

**INVESTIGATION OF CLASSICAL AND NONCLASSICAL
NONLINEARITY IN METALS**

A Dissertation
Presented to
The Academic Faculty

by

Katherine Marie Scott Levy

In Partial Fulfillment
of the Requirements for the Degree
Doctor of Philosophy in the
GW Woodruff School of Mechanical Engineering

Georgia Institute of Technology
December 2019

COPYRIGHT © 2019 BY KATHERINE LEVY

**INVESTIGATION OF CLASSICAL AND NONCLASSICAL
NONLINEARITY IN METALS**

Approved by:

Dr. Laurence Jacobs, Advisor
School of Mechanical & Civil Engineering
Georgia Institute of Technology

Dr. Carly Donahue
Geophysics Group
Los Alamos National Lab

Dr. Jin-Yeon Kim
School of Civil Engineering
Georgia Institute of Technology

Dr. Karim Sabra
School of Mechanical Engineering
Georgia Institute of Technology

Dr. Kenneth Cunefare
School of Mechanical Engineering
Georgia Institute of Technology

Date Approved: November 04, 2019

To my husband

ACKNOWLEDGEMENTS

I would like to start by thanking my advisor Dr. Larry Jacobs. I would like to thank him for providing me with this wonderful opportunity. Without his help and support, this would not have been possible. I would like to thank him for not only providing valuable knowledge with any research question that I had but also advising me on how to successfully obtain a fellowship. I would also like to thank Dr. Jin-Yeon Kim. He has acted as a second advisor to me, and his expertise and help on this research project has been invaluable.

I would next like to thank my committee members, Dr. Cunefare, Dr. Donahue, and Dr. Sabra. I would like to thank you for all of your valuable suggestions and feedback. I would also like to thank Dr. Donahue for providing me with the opportunity to come out to Los Alamos National Lab. I was able to meet and work with some of the best in the field, and the experience was crucial in the completion of my dissertation.

Next, I would like to thank my sources of funding. I would like to thank the NEUP for the IUP fellowship which was my source of funding for the majority of my time here at Georgia Tech. I would like to thank the ASNT for the graduate fellowship which has helped supplement my remaining time here.

Next, I would like to thank Dr. Singh who has been very generous to allow our lab to use his ovens for the heat treatment of our specimens

I would like to thank all of my wonderful lab mates. Their support has been a source of inspiration and a second reason for coming into the lab everyday. I would like

to thank Gun Kim for all of his help and support. When I first started graduate school, he took me under his wing and helped guide me through the experience. He helped build my base of knowledge on NLU and provided a fun and friendly work environment. I would like to thank David Torello for all of his help and support and teaching me how to make all of the nonlinear measurements. He was not only one of my best friends but also my role model. I would like to thank my current lab mates Brian Fuchs and Aurelio Bellotti. They have both provided so much support for helping me finish my PhD. I would like to thank them for providing valuable insight and discussion into my research topic and providing a fun and supportive work environment. Finally, I would like to thank all of the exchange students from Germany and everyone who has spent a short time in our lab. Their richness of culture has brought an unforgettable experience to graduate school. I would like to give a special thanks to Steffen and Niklas for their help on the NRUS measurements.

I would like to thank all of my friends, Megan, Ethan, Reba, Dennis, Devin, Trav, Marnie, and everyone who I have probably forgotten, whose love and support has helped me through this experience. I would like to give a special thanks to Katie Cook. While we have not lived in the same state since I started graduate school, her love and support has kept me going and inspired me to be the best that I can be.

Next, I would like to thank my family. I would like to thank my mom and dad for teaching me how to strive to be the best and teaching me to keep going even when life is hard. I would like to thank them for providing me with the opportunity to get my undergraduate degree at Georgia Tech which has been the building blocks for my

graduate education. I would also like to thank my sister, Kristy. Her love and support has been the fuel for my PhD.

Last but definitely not least, I would like to thank my husband, Bryan. Without his love and support, this degree would not have been possible. He has been there for me through all of it and has provided thoughtful conversations on my research. I am so grateful for him for staying here in Atlanta for me and allowing me to finish this wonderful opportunity (because who are we kidding, I would have followed him to the moon and back).

TABLE OF CONTENTS

ACKNOWLEDGEMENTS	iv
LIST OF TABLES	x
LIST OF FIGURES	xi
LIST OF SYMBOLS AND ABBREVIATIONS	xiv
SUMMARY	xviii
CHAPTER 1. Introduction	1
1.1 Motivation and Background	1
1.1.1 Previous Research on NLU	2
1.1.1.1 Second Harmonic Generation (SHG)	2
1.1.1.2 Nonlinear Resonant Ultrasound Spectroscopy (NRUS)	3
1.2 Objectives	3
1.3 Structure of Thesis	5
CHAPTER 2. Theory	6
2.1 Nonlinear Elasticity	6
2.2 Nonlinear Wave Equation	8
2.2.1 Propagating waves	9
2.2.1.1 Classical quadratic nonlinearity	11
2.2.1.1.1 Longitudinal waves	12
2.2.1.1.2 Rayleigh waves	13
2.2.1.2 Hysteretic nonlinearity	14
2.2.2 Forced Wave Resonance	16
2.2.2.1 Linear Solution	20
2.2.2.2 Quadratic Nonlinearity	22
2.2.2.3 Cubic nonlinearity	23
2.2.2.4 Hysteresis nonlinearity	26
2.2.2.5 Resonance frequency response for forced vibration	29
2.3 Theoretical derivations of contributions to nonlinearity	31
2.3.1 Classical quadratic nonlinearity	31
2.3.1.1 Dislocation pinning	31
2.3.1.2 Precipitate pinned dislocations	34
2.3.2 Nonclassical hysteresis nonlinearity	37
2.4 Nonlinear Ultrasound Resonant Spectroscopy	42
2.4.1 Vibration of 1D Bar	43
2.4.1.1 Longitudinal Strain	44
2.4.1.2 Natural Frequencies of a Free-Free Bar	45
2.4.2 Resonant Ultrasound Spectroscopy (RUS)	46
2.5 Quality Factor	47
2.6 Analysis of variance (ANOVA)	49

CHAPTER 3. Material Description	52
3.1 Overview	52
3.2 304 stainless steel	52
3.2.1 Intergranular stress corrosion cracking	53
3.2.1.1 Sensitization	54
3.2.1.2 Stresses	56
3.2.1.3 Environmental	57
3.2.2 Electrochemical Reactivation (EPR)	57
3.2.3 Microscopy	60
3.3 316L stainless steel	61
3.4 Fe-1.0%Cu Surrogate Specimens	62
3.4.1 Radiation Embrittlement Background	63
3.4.2 Manufacturing and Preparation of Surrogate Specimens	64
3.4.3 Interaction between Cu-precipitate and matrix	64
3.4.3.1 Loss of coherency	66
3.4.4 Precipitate Radii of Fe-1.0% Cu Specimens	67
CHAPTER 4. Experimental Procedure	70
4.1 Overview	70
4.2 SHG	70
4.2.1 Rayleigh Wave Measurements	71
4.2.2 Longitudinal Wave Measurements	75
4.3 NRUS Measurements	78
4.3.1 Determination of resonance frequency	79
4.3.1.1 Experimental determination of resonance frequency	79
4.3.2 Post-processing for NRUS	80
CHAPTER 5. Signal processing for thin specimens	83
5.1 Overview	83
5.2 Method Background	85
5.2.1 Discrete Fourier Transform	85
5.2.2 Prony Method	85
5.2.2.1 Least Squares Prony Method	87
5.2.2.2 Known Poles Prony Method	87
5.2.3 Least Squares Method	87
5.3 Numerical Simulation and Experimental Procedure	89
5.3.1 Numerical Simulation	89
5.3.2 Experimental Procedure	90
5.3.3 Post-Processing	90
5.4 Results and Discussion	90
5.4.1 Effect of SNR on the Synthetic Signals	91
5.4.2 Comparison of Five Candidate Signal Processing Methods	94
5.5 Application for Fe-1.0% Cu specimens	98
CHAPTER 6. NLU Results and Discussion	101
6.1 Overview	101
6.2 304 Stainless Steel	101

6.2.1	Specimen preparation	101
6.2.2	NRUS Results	102
6.2.3	SHG Results	103
6.2.4	ANOVA Results	104
6.3	316L Stainless Steel	105
6.3.1	Specimen preparation	105
6.3.2	NRUS Results	106
6.3.3	SHG Results	107
6.3.4	ANOVA Results	108
6.4	Fe-1.0% Cu	109
6.4.1	Specimen preparation	109
6.4.2	NRUS Results	110
6.4.3	SHG Results	111
6.4.4	SHG model for Fe-Cu alloy and discussion	113
6.4.5	ANOVA results	115
CHAPTER 7. Discussions		117
7.1	Overview	117
7.2	Results from previous studies for comparison	117
7.2.1	17-4PH Stainless Steel	117
7.2.2	Cr9Mo1	119
7.3	Mechanism Discussion	121
7.3.1	304 – sensitization	122
7.3.2	316L – annealed	124
7.3.3	Fe-1.0% Cu	125
7.3.3.1	Comparison of experimental β to models	130
7.3.4	17-4PH	131
7.3.5	Cr9Mo1	133
7.3.6	Summary	134
CHAPTER 8. Conclusions and Future Work		136
8.1	Summary of Results	136
8.2	Recommendations for future work	138
8.3	Significance and Impact	139
APPENDIX A. Theory for Signal Processing Methods		141
A.1	Discrete Fourier Transform	141
A.2	Prony Method	141
A.2.1	Least Squares Prony Method	145
A.2.2	Known Poles Prony Method	147
REFERENCES		151

LIST OF TABLES

Table 1	Cu-precipitate radius of Fe-1.0% Cu specimens	68
Table 2	Minimum SNR of A_2 to accurately determine β within $\pm 5\%$ for original/ LS Prony methods for varying number of effective cycles	94
Table 3	ANOVA results for α for 304 stainless steel	105
Table 4	ANOVA results for α for 316L stainless steel	109
Table 5	ANOVA results for β for 316L stainless steel	109
Table 6	Constants for theoretical model	114
Table 7	ANOVA results for α for Fe-1.0% Cu	116
Table 8	ANOVA result for β for Fe-1.0% Cu	116
Table 9	Summary of materials, mechanisms, and β/α response	122

LIST OF FIGURES

Figure 1	Stress-strain curves showing linear and nonlinear material relationships, from Maier [27] which was adopted from [28]	7
Figure 2	Resonance frequency response from change in strain for each linear and nonlinear portion	30
Figure 3	Precipitate pinned dislocation segment	35
Figure 4	Dislocation pinning model showing increasing stress on the dislocation segment, also showing the stress-dislocation strain relationship– from Granato and Lücke [43]	38
Figure 5	Sample NRUS resonance curves	43
Figure 6	1D Free-Free bar	44
Figure 7	Combination of conditions which lead to IGSCC [46]	54
Figure 8	Microscopy showing a) non-sensitized sample and b) sensitized sample [29]	55
Figure 9	Time-temperature-sensitization curves for different amounts of carbon content [47]	56
Figure 10	Sample reactivation curves from the ASMT standard showing the differences in sensitized and annealed samples [53]	58
Figure 11	Reactivation curve for non-sensitized sample [54]	59
Figure 12	Reactivation curve for sensitized sample [54]	59
Figure 13	EPR results for 304 stainless steel [54]	60
Figure 14	Microscopy for 304 stainless steel: a) 0 minutes, b) 150 minutes, c) 180 minutes, d) 240 minutes, e) 360 minutes [29,54]	61
Figure 15	Dislocation density map of geometrically necessary dislocations showing decreasing dislocation density between the as-forged specimen and the heat treated specimens [55]	62
Figure 16	2D depiction of a) BCC Cu-precipitates, b)9R Cu-precipitates [71]	66
Figure 17	Interface between two crystals, a) coherent interface, b) semi-coherent interface [72]	67

Figure 18	Cu-precipitate radius for Fe-1.0% Cu specimens	68
Figure 19	Rayleigh wave experimental setup	72
Figure 20	Sample time domain plot with figurative Hanning window for Rayleigh wave measurements	73
Figure 21	Sample frequency domain plot for Rayleigh wave measurements	74
Figure 22	Rayleigh wave, A_1 and A_2 as a function of propagation distance	74
Figure 23	Rayleigh wave determination of β	75
Figure 24	Longitudinal Experimental Schematic	76
Figure 25	Raw signal with windowing points	77
Figure 26	A_2 versus A_1^2 where the slope is β	78
Figure 27	NRUS experimental setup	79
Figure 28	Experimental longitudinal vibration modes	80
Figure 29	Time domain signal example for NRUS measurement	81
Figure 30	Resonance frequency spectrum curves example (same as Figure 5)	81
Figure 31	Relative frequency shift as a function of strain amplitude to determine α_f	82
Figure 32	Effect of SNR of A_2 on calculation of relative β for a) three effective cycles b) one effective cycle c) five effective cycles [86]	92
Figure 33	Comparison of signal processing methods for varying number of cycles, a) experimental, b) numerical simulation (synthetic signals) [Note: For less than eight generated cycles, DFT values are so poor that they are off the scale.] [86]	95
Figure 34	Normalized relative β for Fe-1.0% Cu specimens using least squares method, KP Prony method, and original Prony method [6,86]	99
Figure 35	Measurements of α for 304 stainless steel comparing annealed and sensitized specimens	103
Figure 36	Measurements for β for 304 stainless steel comparing results of sensitization [29]	104

Figure 37	Measurements for α for 316L specimens comparing an as-received and heat treated specimen	107
Figure 38	Measurements for β for 316L specimens comparing an as-received and heat treated specimens	108
Figure 39	Measurements for α for Fe-Cu specimens comparing effect of heat treatment time	111
Figure 40	Measurements for β for Fe-Cu specimens comparing effect of heat treatment time [86]	112
Figure 41	Comparison between experimental and theoretical model for β for Fe-1% Cu [6]	115
Figure 42	Results for 17-4PH stainless steel specimens [2,18]	119
Figure 43	Results for Cr9Mo1 specimens [1,102]	120
Figure 44	Overlay showing changes in dislocation density, precipitate radius, and β as a function of heat treatment time [1]	121
Figure 45	Comparison of α , β [29], and E for annealed and sensitized 304	124
Figure 46	Comparison of α , β , and E for as received and heat treated 316L	125
Figure 47	Comparison of classical nonlinearity from Cu atoms and Cu precipitates with increasing point-defect-equivalent concentration [109]	
Figure 48	Comparison of α , β , and E results for Fe-1% Cu specimens (β from [86])	130
Figure 49	Analytical model by Li et al for Fe-Cu alloy [7]	131

LIST OF SYMBOLS AND ABBREVIATIONS

NDE	nondestructive evaluation
SHG	second harmonic generation
NRUS	nonlinear resonant ultrasound spectroscopy
RUS	resonant ultrasound spectroscopy
NLU	nonlinear ultrasound
RPV	reactor pressure vessel
ANOVA	analysis of variance
IGSCC	intergranular stress corrosion cracking
BWR	boiling water reactor
HAZ	heat affected zone
DOS	degree of sensitization
EPR	electrochemical reactivation
DBTT	ductile to brittle transition temperature
CRP	Cu rich precipitate
BCC	body-centered cubic
FCC	face-centered-cubic
SANS	small-angle neutron scattering
FFT	fast Fourier transform
SNR	signal to noise ratio
DFT	discrete Fourier transform
TEP	thermo-electric power
TEM	transmission electron microscopy

APT 3D atom probe tomography
 β classical nonlinearity parameter
 α nonclassical nonlinearity parameter
 σ stress
 K_0 linear elastic modulus
 δ cubic classical nonlinearity parameter
 $\Delta\varepsilon$ local strain amplitude
 $\dot{\varepsilon}$ strain rate
 ν Poisson's ratio
 ω angular frequency
 u particle displacement
 u_1 displacement fundamental wave
 u_2 displacement nonlinear portion
 v velocity
 c_l longitudinal wave speed
 A_1 amplitude of fundamental wave
 A_2 amplitude of second harmonic wave
 ω, f frequency
 k wavenumber
 k_R wavenumber of Rayleigh wave
 k_P wavenumber of longitudinal wave
 k_S wavenumber of shear wave
 F amplitude of sinusoidal force
 Ω circular frequency of resonant driving force

Ω_{res}	resonant frequency
Q	quality factor
ψ	spatial function
z	temporal function
L	length of the NRUS sample
r	radius
τ	shear stress
R	Schmid factor
G	shear modulus
b	Burgers' vector
γ	shear strain
λ	dislocation density
S	area swept dislocation segment
ε_l	lattice strain
$\Delta\sigma$	small oscillatory stress
r_{crit}	critical radius
f_n	volume fraction of critical radii
f_g	volume fraction of growing radii
B	bulk modulus of precipitate
γ_{el}	elastic strain
γ_{dis}	dislocation strain
l	dislocation segment length
ξ	displacement of dislocation
A	effective mass per unit length
B	damping force per unit length

- C force from bowed dislocation
- Δ decrement
- ΔW energy lost per cycle
- W total vibration energy
- H_0 null hypothesis
- H_1 alternative hypothesis

SUMMARY

Nonlinear ultrasound (NLU) techniques such as second harmonic generation (SHG) and nonlinear resonant ultrasound spectroscopy (NRUS) have shown promise in detecting microstructural damage in materials before macroscopic failure can occur. However, before these methods can be implemented in the field, a better understanding of the relationship between the microstructural mechanisms and the parameters that are measured by these nonlinear techniques needs to be established. This is done in this research by isolating multiple mechanisms and studying their relationship to the nonlinearity parameters β and α . These are the two parameters that are measured using SHG and NRUS, respectively. These parameters can then be related back to material properties through the nonlinear elastic stress-strain relationship. This research focuses on three microstructural mechanisms: precipitate growth in and along the grain boundaries, dislocations, and precipitate pinned dislocations. These mechanisms are studied through the sensitization of 304 stainless steel, the annealing of 316L stainless steel, and the heat treatment of Fe-Cu, respectively. Additionally, the results from two previous studies are considered to get a deeper overall understanding of the mechanisms and their relationship to NLU. Through the experimental measurements and analysis, the response of β and α to each microstructural mechanism is determined. It is found that both techniques are highly sensitive to changes in the microstructure but do not always have the same response to each mechanism. It was found that α is sensitive to nonlinear energy dissipation mechanisms and β is sensitive to interactions between mechanisms.

CHAPTER 1. INTRODUCTION

1.1 Motivation and Background

With the aging of infrastructure, there is an increased need to determine the remaining life of these structures. While remaining life can sometimes be determined using destructive tests, this is not always a viable option. Additionally, it can be very difficult to model the exact wear that has occurred in a structure. Therefore, it is important to develop nondestructive evaluation (NDE) techniques that can be used to predict the remaining life of these structures. It is also important to detect the initial onset of microstructural damage of structures before macro-cracking occurs. Such detection of the amount of microstructural damage can help provide quantitative inputs for algorithms capable of predicting the remaining life of a structure before catastrophic failure occurs.

One example of these aging structures is the reactor pressure vessel (RPV) in light water nuclear power reactors. With the current fleet of nuclear reactors in the United States entering the first period of license renewal (operation to 60 years) and planning has begun for a second renewal (operation to 80 years), RPV steel will see more neutron exposure and duty cycles than was originally anticipated. Therefore, it is very important to be able to inspect the condition of these RPVs. If microstructural damage is not caught before macro-cracking occurs, the results could be catastrophic. This early detection of microstructural damage would allow for the nuclear reactors to be in service past their predicted lifespan. This example demonstrates just one of the plethora of situations where the detection of precursors to macroscopic damage will be useful.

Currently, the NDE methods capable of detecting initial microstructural damage in these structures are very limited and have not proven easy to perform field tests. The prominent NDE method of using linear ultrasound has shown excellent results in many applications and is capable of detecting cracks or other features on the same order of magnitude as the wavelength of the ultrasonic wave. In conjunction, the current research on linear ultrasound has shown that it is unable to detect this onset of microstructural damage at very small length scales. However, there have been numerous accounts of promising results with nonlinear ultrasound techniques such as second harmonic generation (SHG) [1–16] and nonlinear resonant ultrasound spectroscopy (NRUS) for this application [17–26].

1.1.1 Previous Research on NLU

1.1.1.1 Second Harmonic Generation (SHG)

Many research studies have shown the potential of SHG to detect microstructural damage in a variety of conditions, and SHG has been shown as a promising technique for metals as well as cement-based materials. These studies have shown the ability of SHG to detect “material damage” such as dislocations [9–11], dislocation dipoles [12,13], precipitates [6,7], and precipitate pinned dislocations [10,14–16] which are all known precursors to macroscopic cracking and damage. Research has shown that the sensitivity of SHG to this microstructural damage is useful in a variety of applications. In one study, SHG gave promising results in the detection of radiation damage in RPV steels [3,4]. Another study shows how SHG can be used to determine damage in thermally treated

materials [5]. Additionally, a study looked at cement-based materials and determined the sensitivity of SHG to microcracks and other microstructural changes [8].

1.1.1.2 Nonlinear Resonant Ultrasound Spectroscopy (NRUS)

Like SHG, NRUS has proven to be useful in many damage situations. So far, the majority of the research has focused on highly hysteretic, nonmetallic materials such as rock [20,21], concrete [22,23], and bone [24]. Research on these materials has shown that the source of hysteretic nonlinearity is from “soft” inclusions found in a “hard” matrix [26]. One study has demonstrated the sensitivity of NRUS theoretically and experimentally to damaged and undamaged concrete bars [22]. Another study looked at the feasibility of NRUS to predict microcracking in bones and saw significant changes in the hysteretic nonlinearity parameter, α , with increased damage while wave velocity saw minimal change [24].

While there has been minimal research and understanding on the mechanisms behind the hysteretic response of metals, there have been a couple of studies that have demonstrated very promising results[18,25]. One study looked at how dislocation densities in Al and Cu contribute to the nonlinearity [25]. A different study demonstrated the sensitivity of NRUS to precipitate growth [18].

1.2 Objectives

While SHG and NRUS have shown promise in detecting changes in the microstructure for a wide range of materials, the issue remains that these techniques are sensitive to multiple microstructural mechanisms which can lead to complications when

studying materials with complicated microstructures. Therefore, it is important to understand the sensitivity and relationship of the NLU parameters, β and α (SHG and NRUS, respectively) to individual mechanisms before more complicated situations can be studied as a whole. This knowledge will then allow these parameters to be used in the future as inputs into quantitative algorithms which would be invaluable for *in-situ* measurements. Therefore, this research aims to expand the understanding and versatility of these NLU techniques and aims to build another portion of the bridge between the laboratory measurements and *in-situ* measurements. This will be done through the series of objectives described below.

Objective 1. *Investigate the sensitivity of NRUS to microstructural damages in metals.*

This portion of the research will investigate different types of microstructural damage that may occur in metals such as precipitate formation and dislocations. While there have been many studies on NRUS that have looked at geomaterials, little is known about the relationship between NRUS and metals.

Objective 2. *Investigate the sensitivity of SHG to microstructural damages in metals and consider the application to thin specimens.* In order to allow a comparison between the NLU methods, the sensitivity of SHG to the same microstructural damages explored using NRUS is considered. While a great deal is known about the links between SHG and the mechanisms, the study of specific conditions will allow for a better comparison of the methods.

Objective 2b. *Consider a geometrical implication on SHG by examining thin specimens.* In many applications, only thin specimens are available to study the material.

However, because of the need to avoid interference between the incident and reflected waves, many researchers steer clear of thin specimens. This research will look at how SHG can still be used to look at these materials.

Objective 3. Compare SHG and NRUS and draw a link between their sensitivities and mechanisms. By making SHG and NRUS on samples with the same damage, a study will be done to compare each of these NLU techniques. A model of this kind will allow for a better understanding of the techniques individually as well as allow future comparisons between the measurement methods.

1.3 Structure of Thesis

This dissertation will be presented through the following sections. Chapter 2 will present the theory for these nonlinear ultrasound techniques as well as demonstrate that in perturbation situations these parameters can be considered completely separate. Chapter 3 will present an overview of the material that was studied in this research as well as provide an understanding of the “ground truth” of these specimens. Chapter 4 will present the experimental procedure for these nonlinear ultrasound techniques. Chapter 5 will present the results for the thin specimens geometric study for SHG. Chapter 6 will present the experimental results for the NRUS and SHG measurements Chapter 7 provides a discussion on the microstructural mechanisms and their relationship to α and β . Finally, chapter 8 summarizes the conclusions, provides some insights into future work, and describes the significant impact.

CHAPTER 2. THEORY

2.1 Nonlinear Elasticity

Nonlinear elastic behavior is observed in materials when the linear stress-strain relationships no longer hold. Considering a 1-D case, the nonlinear stress-strain relationship can be defined as

$$\sigma = K_0 \varepsilon (1 + \beta \varepsilon + \delta \varepsilon^2 + \dots) + K_0 \frac{\alpha}{2} [\text{sgn}(\dot{\varepsilon})((\Delta \varepsilon)^2 - \varepsilon^2) - 2(\Delta \varepsilon)\varepsilon] \quad (1)$$

where K_0 is the linear elastic modulus, β is the quadratic classical nonlinearity parameter, δ is the cubic classical nonlinearity parameter, α is the hysteretic nonlinearity parameter, $\Delta \varepsilon$ is the local strain amplitude, and $\dot{\varepsilon}$ is the strain rate. When looking at the equation of state, $K_0 \varepsilon$ refers to the linear elastic behavior, the terms containing β and δ are considered classical nonlinear elastic behavior, and the term containing α is considered nonclassical nonlinear elastic or hysteretic behavior.

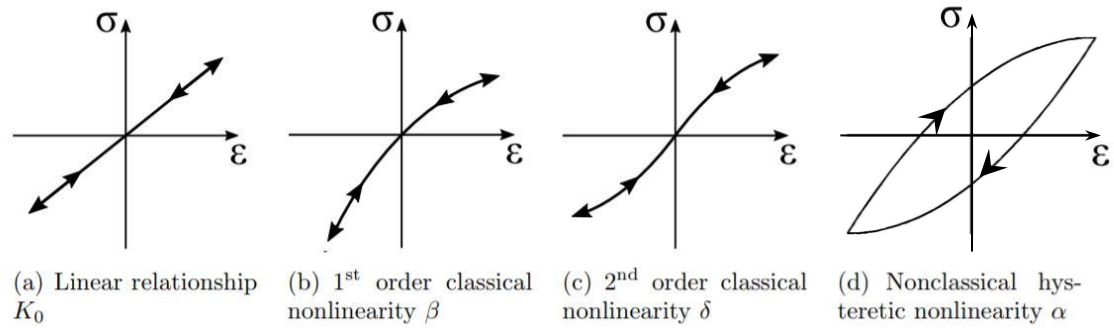


Figure 1. Stress-strain curves showing linear and nonlinear material relationships, from Maier [27] which was adopted from [28]

Figure 1 graphically demonstrates the stress-strain behaviors for the linear regime (a), the classical nonlinear regime (b-c), and the nonclassical nonlinear regime (d). The linear regime demonstrates classical behavior and is representative of Hooke’s law. The classical nonlinear regime consists of both quadratic and cubic nonlinearity.

Current research has shown that classical nonlinearity is dependent on the material crystalline structure and the related local nonlinear (or excessive) strain fields on the atomic scale [9–16,29]. Studies have shown that these local strain fields are caused by “material damage” such as dislocations [9–11], dislocation dipoles [12,13], precipitates [29], and precipitate pinned dislocations [10,14–16]. Section 2.3.1 will go through the theoretical models that have been previously developed to explain the effect each of these “damages” has to the classical nonlinearity.

Nonclassical nonlinearity demonstrates hysteresis and results from nonlinear energy dissipation. The mechanisms behind this energy dissipation are things such as opening/closing of microcracks, friction, sliding of rough contact, etc. Nonclassical nonlinearity focuses on the material at a mesoscopic scale (scale between nanolevel and

macroscopic scale), and was first observed in materials such as sandstone, rock, and concrete which is now known as mesoscopic-elastic materials. These materials demonstrate very high nonlinearity even at very low strain rates. Physically, the hysteresis in these materials may be due to “soft” inclusions found in a “hard” matrix [26]. While a great deal of research has been done on looking at hysteresis in these mesoscopic materials, very little research has been done looking at the mechanisms behind hysteresis in metals. It is hypothesized that the mechanisms in metals will be similar but will focus on dislocations and interaction between precipitates and the grain structure.

2.2 Nonlinear Wave Equation

The general one-dimensional nonlinear wave equation (Eq. 3) can be derived by substituting the nonlinear stress-strain relationship described in Eq. 1 into the one-dimensional equation of motion (Eq. 2) where ρ is the density of the material and u is the displacement.

$$\rho \frac{\partial^2 u}{\partial t^2} = \frac{\partial \sigma}{\partial x} \quad (2)$$

$$\begin{aligned} \rho \frac{\partial^2 u}{\partial t^2} = & K_0 \left[\frac{\partial^2 u}{\partial x^2} + \beta \frac{\partial u}{\partial x} \frac{\partial^2 u}{\partial x^2} + \delta \left(\frac{\partial u}{\partial x} \right)^2 \frac{\partial^2 u}{\partial x^2} + \dots \right] \\ & + K_0 \frac{\alpha}{2} \frac{\partial}{\partial x} \left\{ \text{sgn} \left(\frac{\partial^2 u}{\partial t \partial x} \right) \left[\left(\Delta \frac{\partial u}{\partial x} \right)^2 - \left(\frac{\partial u}{\partial x} \right)^2 \right] - 2 \left(\Delta \frac{\partial u}{\partial x} \right) \frac{\partial u}{\partial x} \right\} \end{aligned} \quad (3)$$

Now that the generic nonlinear wave equation has been established, it is of interest to determine the equation for the displacement, u , for two different forcing conditions. These forcing conditions will be synonymous to conditions seen in experimental SHG and NRUS. The first forcing condition investigated will be a monochromatic propagating wave. The focus for the first forcing condition will be the response from classical nonlinearity where the following sections will derive the classical nonlinearity parameter, β , for both longitudinal and Rayleigh waves. The second forcing condition investigated will be a forced resonance. In this section, the focus will be on the response from hysteresis nonclassical nonlinearity.

Additionally, these sections will show that for the perturbation situation on the order of $O(\epsilon^2)$ β and α can be completely decoupled where hysteretic nonlinearity has no effect of the SHG results, and classical quadratic nonlinearity has no effect on the NRUS results.

2.2.1 *Propagating waves*

The displacement response to a sinusoidal propagating wave will be the first case considered, and this section will follow the derivation proposed by Chen et al. [30]. For this case, it will be assumed that the displacement solution linearly adds the linear (fundamental wave, u_1) and nonlinear displacement portions (second-order solution, u_2): $u = u_1 + u_2$ and that the nonlinear behavior is much smaller than the linear behavior, $|u_2| \ll |u_1|$. Keeping in mind these assumptions, the displacement solution is plugged into the nonlinear wave equation as seen in Eq 4.

$$\begin{aligned}
& \rho \left(\frac{\partial^2 u_1}{\partial t^2} + \frac{\partial^2 u_2}{\partial t^2} \right) \\
&= K_0 \left(\frac{\partial^2 u_1}{\partial t^2} + \frac{\partial^2 u_2}{\partial t^2} \right) + \beta K_0 \left(\frac{\partial u_1}{\partial x} + \frac{\partial u_2}{\partial x} \right) \left(\frac{\partial^2 u_1}{\partial x^2} + \frac{\partial^2 u_2}{\partial x^2} \right) \\
&+ K_0 \frac{\alpha}{2} \frac{\partial}{\partial x} \left\{ \operatorname{sgn} \left(\frac{\partial^2 u_1}{\partial t \partial x} + \frac{\partial^2 u_2}{\partial t \partial x} \right) \left[\left(\Delta \left(\frac{\partial u_1}{\partial x} + \frac{\partial u_2}{\partial x} \right) \right)^2 \right. \right. \\
&\quad \left. \left. - \left(\frac{\partial u_1}{\partial x} + \frac{\partial u_2}{\partial x} \right)^2 \right] - 2 \left(\Delta \left(\frac{\partial u_1}{\partial x} + \frac{\partial u_2}{\partial x} \right) \right) \left(\frac{\partial u_1}{\partial x} + \frac{\partial u_2}{\partial x} \right) \right\} \tag{4}
\end{aligned}$$

In order to simplify the above equation, a couple of simplifications will be taken into consideration. Since $|u_2| \ll |u_1|$, the higher order terms of u_2 (as found in the terms associated with β and α) are considered negligible and are not considered in the final equation. Additionally, it is known that $\rho \frac{\partial^2 u_1}{\partial t^2} = K_0 \frac{\partial^2 u_1}{\partial t^2}$ because u_1 satisfies the linear wave equation, leading to the cancellation of these terms in the final equation. Finally, the sign change from the second order wave is ignored. The simplified version of the nonlinear wave equation can be seen in the following equation:

$$\begin{aligned}
\rho \frac{\partial^2 u_2}{\partial t^2} &= K_0 \frac{\partial^2 u_2}{\partial x^2} + \beta K_0 \frac{\partial u_1}{\partial x} \frac{\partial^2 u_1}{\partial x^2} \\
&+ K_0 \frac{\alpha}{2} \frac{\partial}{\partial x} \left\{ \text{sgn} \left(\frac{\partial^2 u_1}{\partial t \partial x} \right) \left[\left(\Delta \frac{\partial u_1}{\partial x} \right)^2 - \left(\frac{\partial u_1}{\partial x} \right)^2 \right] \right. \\
&\left. - 2 \left(\Delta \frac{\partial u_1}{\partial x} \right) \frac{\partial u_1}{\partial x} \right\}
\end{aligned} \tag{5}$$

2.2.1.1 Classical quadratic nonlinearity

Classical quadratic nonlinearity will be the first case considered, and the well-known solution to the nonlinear wave equation will be investigated [30–32]. When looking at classical nonlinearity, only the corresponding portion of the nonlinear wave equation will be considered as seen in Eq 6 where c_l is the longitudinal wave speed and $c_l^2 = E_0/\rho$.

$$\frac{\partial^2 u_2}{\partial t^2} = c_l^2 \left[1 - \beta \frac{\partial u_1}{\partial x} \right] \frac{\partial^2 u_1}{\partial x^2} \tag{6}$$

SHG is the typical experimental technique associated with classical quadratic nonlinearity. SHG looks at the generation of second harmonic waves in a material due to material nonlinearities. For SHG, a monochromatic wave is introduced into the material through either longitudinal or Rayleigh waves. This wave interacts with nonlinearities found in the material, and higher harmonic waves are generated. While the generation of higher harmonics is possible, the focus of SHG is relating the amplitude of the second

harmonic wave to the amplitude of the fundamental frequency. This can be done through the classical nonlinearity parameter, β , which will be derived later in this section.

2.2.1.1.1 Longitudinal waves

Consider a sinusoidal longitudinal wave, with an angular frequency of ω , which propagates in the x-direction through a quadratic nonlinear, isotropic, elastic material, and the equation for this fundamental wave can be written as the following where A_1 is the wave amplitude and k is the wave number.

$$u_1 = A_1 \sin(kx - \omega t) \quad (7)$$

By plugging the equation for the fundamental wave (Eq 7) into the nonlinear wave equation (Eq. 6), one can solve for the equation of the second harmonic wave which can be seen in Eq. 8.

$$u_2 = -\frac{\beta k^2 x A_1^2}{8} \cos 2(kx - \omega t) = A_2 \cos 2(kx - \omega t) \quad (8)$$

With the amplitude of the second harmonic wave denoted as A_2 , the classical nonlinearity parameter, β , can be solved for as seen in the following equation.

$$\beta = \frac{8|A_2|}{k^2 x A_1^2} \propto \frac{A_2}{A_1^2} \quad (9)$$

Eq. 9 shows that the nonlinearity parameter, β is a direct function of the amplitudes of the fundamental and second harmonic waves, which makes the accurate extraction of each of these amplitudes from a measured tone-burst signal critical for successful SHG measurements.

2.2.1.1.2 Rayleigh waves

The derivation for Rayleigh waves is more in depth than the longitudinal waves because a Rayleigh wave contains both longitudinal and shear wave components. Let's consider the propagation of a Rayleigh wave in the positive x -direction in an isotropic infinite half-space where the z -direction is pointing into the half-space. Assuming plane wave propagation and a stress-free surface, the x and z particle displacements can be decomposed as the following

$$u_x = A_1 \left(e^{-pz} - \frac{2ps}{k_R^2 + s^2} e^{-sz} \right) e^{i(k_R x - \omega t)} \quad (10)$$

$$u_z = iA_1 \frac{p}{k_R} \left(e^{-pz} - \frac{2k_R^2}{k_R^2 + s^2} e^{-sz} \right) e^{i(k_R x - \omega t)} \quad (11)$$

where $p^2 = k_R^2 - k_P^2$, $s^2 = k_R^2 - k_S^2$, k_R is the wavenumber of the Rayleigh wave, k_P is the wavenumber of the longitudinal wave, and k_S is the wavenumber of the shear wave. For the second harmonic Rayleigh wave, the displacement components can be approximated as following at a sufficiently large distance [33,34]

$$u_x = A_2 \left(e^{-2pz} - \frac{2ps}{k_R^2 + s^2} e^{-2sz} \right) e^{i2(k_R x - \omega t)} \quad (12)$$

$$u_z = iA_2 \frac{p}{k_R} \left(e^{-2pz} - \frac{2k_R^2}{k_R^2 + s^2} e^{-2sz} \right) e^{i2(k_R x - \omega t)} \quad (13)$$

It is known for isotropic materials that the acoustic nonlinearity due to shear waves disappears due to symmetry conditions making the longitudinal wave the only component

responsible for the acoustic nonlinearity. The acoustic nonlinearity parameter, β , in terms of out-of-plane components can then be derived as [33] where \bar{u}_z is the displacement evaluated at $z=0$

$$\beta = \frac{\bar{u}_z(2\omega)}{\bar{u}_z^2(\omega)x} \frac{i8p}{k_P^2 k_R} \left(1 - \frac{2k_R^2}{k_R^2 + s^2} \right) \propto \frac{A_2}{A_1^2 x} \quad (14)$$

2.2.1.2 Hysteretic nonlinearity

This section will focus on the hysteretic nonlinearity portion of the nonlinear wave equation (Eq 15). Eq 15 can be seen below. In order to simplify Eq 15, a new variable, $X = x - ct$, will be introduced allowing the consolidation of the number of dependent variables. Using the chain rule, the equation can be simplified by plugging in $\partial/\partial x = \partial/\partial X$ and $\partial/\partial t = -c \partial/\partial X$, and the simplified equation can be seen in Eq. 16.

$$K_0 \frac{\alpha}{2} \frac{\partial}{\partial x} \left\{ \text{sgn} \left(\frac{\partial^2 u_1}{\partial t \partial x} \right) \left[\left(\Delta \frac{\partial u_1}{\partial x} \right)^2 - \left(\frac{\partial u_1}{\partial x} \right)^2 \right] - 2 \left(\Delta \frac{\partial u_1}{\partial x} \right) \frac{\partial u_1}{\partial x} \right\} \quad (15)$$

$$K_0 \frac{\alpha}{2} \left\{ - \frac{\partial}{\partial x} \left[\text{sgn} \left(\frac{\partial^2 u_1}{\partial X^2} \right) \right] \left[\left(\Delta \frac{\partial u_1}{\partial X} \right)^2 - \left(\frac{\partial u_1}{\partial X} \right)^2 \right] - 2 \text{sgn} \left(\frac{\partial^2 u_1}{\partial X^2} \right) \frac{\partial u_1}{\partial X} \frac{\partial^2 u_1}{\partial X^2} \right. \\ \left. - 2 \left(\Delta \frac{\partial u_1}{\partial X} \right) \frac{\partial^2 u_1}{\partial X^2} \right\} \quad (16)$$

Using the same equation for the fundamental longitudinal wave as was used in the SHG section as well as the following reductions seen in Eq. 17, one can reduce the hysteretic portion of the wave equation even further as seen in Eq. 18.

$$u_1 = A_1 \sin(kX)$$

$$\text{sgn}\left(\frac{\partial^2 u_1}{\partial X^2}\right) = -\text{sgn}(\sin(kX)) \quad (17)$$

$$\Delta \frac{\partial u_1}{\partial X} = A_1 k$$

$$\begin{aligned} K_0 \frac{\alpha}{2} \left\{ \left[\frac{\partial}{\partial X} \text{sgn}(\sin(kX)) \right] (A_1 k)^2 \cos(kX)^2 \right. \\ \left. - 2 \text{sgn}(\sin(kX)) A_1 k^3 \cos(kX) \sin(kX) + 2 A_1 k^3 \sin(kX) \right\} \quad (18) \end{aligned}$$

Next, the Fourier series expansion (Eq. 19) for $\text{sgn}(\sin(kX))$ is substituted into the hysteretic excitation term, and the expanded term can be seen in Eq. 20.

$$\text{sgn}(\sin(kX)) = \sum_{n=1,3,5,\dots}^{\infty} \left(\frac{4}{n\pi} \right) \sin(nkX) \quad (19)$$

$$\begin{aligned} K_0 \frac{\alpha}{\pi} A_1^2 k^3 \left\{ \sum_{n=1,3,5,\dots}^{\infty} \left[\cos(nkX) + \left(\frac{1}{n} - \frac{1}{2} \right) \cos((n-2)kX) \right. \right. \\ \left. \left. + \left(\frac{1}{n} + \frac{1}{2} \right) \cos((n+2)kX) \right] + \pi \sin(kX) \right\} \quad (20) \end{aligned}$$

The above equation for the hysteretic excitation term shows that all the frequencies will be odd multiples of the fundamental frequency leading to the conclusion that hysteretic nonlinearity generates only odd harmonics.

This leads to the conclusion that any second harmonic component in propagating longitudinal waves will be due to classical nonlinearity. This means that any changes in β will be solely due to classical quadratic nonlinearity. Note that this is only the case for the perturbation solution (strain levels are much lower than 1 on the order of $O(u_2/u_1)^2$). If the strain levels are larger, then this argument will not hold.

2.2.2 Forced Wave Resonance

This section focuses on the forced wave resonance in a 1D bar with length L and will follow the analytical solution proposed by Van Den Abeele [35]. In this instance, the nonlinear wave equation has additional terms which account for both the external sinusoidal excitation and the attenuation. The excitation considered is a sinusoidal force with an amplitude of \tilde{F} and a circular frequency of Ω applied at one end of the bar. The response is measured at the opposite end of the bar. Eq. 21 shows this nonlinear wave equation where Q is the frequency independent quality factor and $\delta_{x,0}$ is the Kronecker symbol which designates that the force is applied at the location $x = 0$.

$$\begin{aligned} \rho \frac{\partial^2 u}{\partial t^2} = \frac{\partial}{\partial x} & \left\{ K_0 \frac{\partial u}{\partial x} \left(1 + \beta \frac{\partial u}{\partial x} + \delta \left(\frac{\partial u}{\partial x} \right)^2 + \dots \right) \right. \\ & \left. + K_0 \frac{\alpha}{2} \left\{ \text{sgn} \left(\frac{\partial^2 u}{\partial t \partial x} \right) \left[\left(\Delta \frac{\partial u}{\partial x} \right)^2 - \left(\frac{\partial u}{\partial x} \right)^2 \right] - 2 \left(\Delta \frac{\partial u}{\partial x} \right) \frac{\partial u}{\partial x} \right\} \right. \\ & \left. - \rho \frac{\Omega}{Q} \frac{\partial u}{\partial t} + \tilde{F} \cos(\Omega t) \delta_{x,0} \right\} \quad (21) \end{aligned}$$

It is assumed that the displacement field can be written as the summation of products between the spatial, $\psi_i(x)$, and temporal functions, $z_i(t)$. This summation is seen in Eq. 22.

$$u(x, t) = \sum_i \psi_i(x) z_i(t) \text{ for } i = 0, 1, 2, \dots, +\infty \quad (22)$$

The spatial functions, $\psi_i(x)$, are chosen such that they satisfy the boundary conditions: free boundaries, $\psi_n(x) = \cos(n\pi x/L)$. Additionally, the spatial functions represent the normal modes and are chosen such that the shape functions for both the displacement and strain are mutually orthogonal as depicted in Eq. 23

$$\int_0^L \psi_i(x) \psi_j(x) dx = 0 \text{ for } i \neq j$$

$$\int_0^L \frac{\partial \psi_i}{\partial x}(x) \frac{\partial \psi_j}{\partial x}(x) dx = 0 \text{ for } i \neq j$$
(23)

This expression for the displacement is plugged into Eq. 21:

$$\begin{aligned}
& \rho \frac{\partial^2}{\partial t^2} \left(\sum_i \psi_i(x) z_i(t) \right) \\
&= \frac{\partial}{\partial x} \left\{ K_0 \frac{\partial}{\partial x} \left(\sum_i \psi_i(x) z_i(t) \right) \left(1 + \beta \frac{\partial}{\partial x} \left(\sum_i \psi_i(x) z_i(t) \right) \right. \right. \\
&\quad \left. \left. + \delta \left(\frac{\partial}{\partial x} \left(\sum_i \psi_i(x) z_i(t) \right) \right)^2 + \dots \right) \right. \\
&\quad \left. + K_0 \frac{\alpha}{2} \left\{ \text{sgn} \left(\frac{\partial^2}{\partial t \partial x} \left(\sum_i \psi_i(x) z_i(t) \right) \right) \left[\left(\Delta \frac{\partial}{\partial x} \left(\sum_i \psi_i(x) z_i(t) \right) \right)^2 \right. \right. \right. \\
&\quad \left. \left. \left. - \left(\frac{\partial}{\partial x} \left(\sum_i \psi_i(x) z_i(t) \right) \right)^2 \right] \right. \right. \\
&\quad \left. \left. - 2 \left(\Delta \frac{\partial}{\partial x} \left(\sum_i \psi_i(x) z_i(t) \right) \right) \frac{\partial}{\partial x} \left(\sum_i \psi_i(x) z_i(t) \right) \right\} \right. \\
&\quad \left. - \rho \frac{\Omega}{Q} \frac{\partial}{\partial t} \left(\sum_i \psi_i(x) z_i(t) \right) + \tilde{F} \cos(\Omega t) \delta_{x,0} \right.
\end{aligned} \tag{24}$$

The next step for finding the general solution to this problem is multiplying both sides of Eq. 24 by $\psi_i(x)$ and integrating over x from 0 to L (the entire length of the bar). Using the mutually orthogonal relationship and some tedious math, the simplification of

all but the hysteretic term is fairly straight forward and can be seen in Eq. 25. However, the hysteretic term is fairly complicated so a couple of assumptions are made to simplify the equation. First, it is assumed that the dominant contribution in the strain field amplitude is the linear strain solution so the approximation $\Delta \frac{\partial u}{\partial x} \approx m \frac{\pi}{L} A_m$ is used. Second, it is assumed that the excitation frequency is close to one of the resonance frequencies (m th mode). These assumptions can then be used to simplify the hysteretic term which is also seen in Eq. 25. ω_n is defined as the linear (low amplitude) resonance frequencies where $\omega_n = n(\pi c/L)$ and c is the linear bar velocity.

$$\begin{aligned}
& \frac{\partial^2 z_n}{\partial t^2} + \frac{\Omega}{Q} \frac{\partial z_n}{\partial t} + \omega_n^2 z_n \\
&= \frac{2\tilde{F}}{\rho L} \cos(\Omega t) - \sum_{n,i,j} B_{ijk} z_j z_k - \sum_{n,i,j,l} D_{nijkl} z_j z_k z_l \\
& \quad - \sum_{n,m} H_{nm} \left[\text{sgn} \left(\frac{\partial z_m}{\partial t} \right) (A_m^2 - z_m^2) - 2A_m z_m \right]
\end{aligned} \tag{25}$$

$$B_{ijk} = \frac{2K}{\rho L} \int_0^L \beta(x) \frac{\partial \psi_n}{\partial x} \frac{\partial \psi_j}{\partial x} \frac{\partial \psi_k}{\partial x} dx \tag{26}$$

$$D_{ijkl} = \frac{2K}{\rho L} \int_0^L \delta(x) \frac{\partial \psi_n}{\partial x} \frac{\partial \psi_j}{\partial x} \frac{\partial \psi_k}{\partial x} \frac{\partial \psi_l}{\partial x} dx \tag{27}$$

$$H_{nm} = \frac{K}{\rho L} \int_0^L \alpha(x) \frac{\partial \psi_n}{\partial x} \left| \frac{\partial \psi_m}{\partial x} \right| \frac{\partial \psi_m}{\partial x} dx \tag{28}$$

2.2.2.1 Linear Solution

In this section, the linear response of the bar for this forced resonance system is considered. It is assumed that the source frequency Ω is close to ω_m , and this is the only mode activated because the driving frequency is too far away to activate any other modes. For this solution, the material is considered completely linear with the absence of all nonlinearity ($\beta \equiv 0, \delta \equiv 0$, and $\alpha \equiv 0$). With this knowledge and assumptions, the resultant wave equation can be written as the following

$$\frac{\partial^2 z_m}{\partial t^2} + \frac{\Omega}{Q} \frac{\partial z_m}{\partial t} + \omega_m^2 z_m = F \cos(\Omega t) \quad (29)$$

where $F = \frac{2\tilde{F}}{\rho L}$ is the forcing amplitude. Using differential equations, the particular solution to the wave equation can be written in the following form.

$$z_p = A \cos(\Omega t) + B \sin(\Omega t) \quad (30)$$

Plugging the particular solution back into the wave equation (Eq. 31) and equating corresponding terms (Eq. 32 and Eq. 33), one can solve for the constants A and B seen in Eq. 34. The particular solution for the temporal function can then be related to the amplitude of the displacement as seen in Eq. 35. The amplitude of the displacement can be solved for using A and B as seen in Eq. 36. The tangent of the phase can be solved for using A and B as seen in Eq. 37. The final form of the displacement can then be seen in Eq. 38.

$$\left(A\omega_m^2 - \Omega^2 A + \frac{\Omega^2}{Q} B\right) \cos(\Omega t) + \left(B\omega_m^2 - \Omega^2 B - \frac{\Omega^2}{Q} A\right) \sin(\Omega t) = F \cos(\Omega t) \quad (31)$$

$$\left(A\omega_m^2 - \Omega^2 A + \frac{\Omega^2}{Q} B\right) = F \quad (32)$$

$$\left(B\omega_m^2 - \Omega^2 B - \frac{\Omega^2}{Q} A\right) = 0 \quad (33)$$

$$z_p = \frac{\omega_m^2 - \Omega^2}{\left((\omega_m^2 - \Omega^2)^2 + \left(\frac{\Omega^2}{Q}\right)^2\right)} F \cos(\Omega t) + \frac{\frac{\Omega^2}{Q}}{\left((\omega_m^2 - \Omega^2)^2 + \left(\frac{\Omega^2}{Q}\right)^2\right)} F \sin(\Omega t) \quad (34)$$

$$z_p = A \cos(\Omega t) + B \sin(\Omega t) = A_m \cos(\Omega t + \phi_m) \quad (35)$$

$$A_m = \sqrt{A^2 + B^2} = \frac{F}{\sqrt{(\Omega^2 - \omega_m^2)^2 + \left(\frac{\Omega^2}{Q}\right)^2}} \quad (36)$$

$$\tan(\phi_m) = \frac{B}{A} = -\frac{\Omega^2}{Q(\Omega^2 - \omega_m^2)} \quad (37)$$

$$z_m = \frac{F}{\sqrt{(\Omega^2 - \omega_m^2)^2 + \left(\frac{\Omega^2}{Q}\right)^2}} \cos\left(\Omega t + \tan^{-1}\left(-\frac{\Omega^2}{Q(\Omega^2 - \omega_m^2)}\right)\right) \quad (38)$$

The maximum amplitude response ($dA/d\Omega = 0$) can then be used to determine the true resonance frequency of a linear damped oscillator which can be seen in Eq. 39. This equation shows that the true resonance frequency for a linear response is independent of the excitation amplitude.

$$\Omega_{res} = \frac{\omega_m}{\sqrt{1 + 1/Q^2}} \quad (39)$$

2.2.2.2 Quadratic Nonlinearity

This section will focus on the solution to the quadratic (classical) nonlinearity portion ($\alpha \equiv 0$ and $\delta \equiv 0$) of the wave equation under forced resonance. This section will focus on the integral of the spatial portion of the displacement seen in Eq. 26 because it will be shown that this integral will go to zero under the assumptions made for this problem. For a thin bar (1D case) under longitudinal vibration, the spatial portion of the displacement can be written as the following because of the free-free boundary conditions.

$$\psi_j = \cos\left(\frac{n\pi x}{L}\right) \quad (40)$$

Since the excitation frequency is chosen to be close to one of the resonance modes (m), it can be assumed that this will be the only mode of excitation, and the integral in the quadratic nonlinearity term can be written as the following equation. Note that it is also assumed that β is not a function of x because of the isotropy of the material ($\beta(x) \equiv \beta$).

$$\int_0^L \left(\frac{\partial \psi_j}{\partial x} \right)^3 dx = \int_0^L \left(\sin \left(\frac{n\pi x}{L} \right) \right)^3 dx \quad (41)$$

To solve this integral, trigonometric identities and a function substitution are used to obtain the following solution:

$$\int_0^L \left(\sin \left(\frac{n\pi x}{L} \right) \right)^3 dx = \left. \frac{\left(\cos \left(\frac{n\pi x}{L} \right) \right)^3}{3 \left(\frac{n\pi}{L} \right)} - \frac{\cos \left(\frac{n\pi x}{L} \right)}{\left(\frac{n\pi}{L} \right)} \right|_0^L \quad (42)$$

Plugging in the bounds to this solution, one can get the following equation.

$$\frac{\left(\cos(n\pi) \right)^3}{3 \left(\frac{n\pi}{L} \right)} - \frac{\cos(n\pi)}{\left(\frac{n\pi}{L} \right)} - \frac{1}{3 \left(\frac{n\pi}{L} \right)} + \frac{1}{\left(\frac{n\pi}{L} \right)} \quad (43)$$

For even resonance modes, the above equation will be equal to zero. Since quadratic nonlinearity is only nonminimal for even harmonics, this assumption can be made. With the above integral equaling zero, the entire quadratic nonlinearity term goes to zero. This is a crucial finding. It demonstrates that for a forced resonance system (same circumstances seen for the NRUS measurements) under these conditions and assumptions the quadratic nonlinearity will have no influence on the response of the material.

2.2.2.3 Cubic nonlinearity

This section will focus on the solution to the nonlinear wave equation where only the effects of cubic nonlinearity ($\beta \equiv 0$ and $\alpha \equiv 0$) are considered. The excitation

frequency is chosen to be close to one of the modes of resonance (m), and it will be assumed that this will be the only mode that will be excited. Therefore, the nonlinear wave equation can be written in the following form where Eq. 44 is the wave equation and Eq. 45 is the definition for D . Assuming that the spatial portion of the displacement can be written the same as Eq. 40, the definition for D can be expanded as the second portion of Eq. 45.

$$\frac{\partial^2 z_m}{\partial t^2} + \frac{\Omega}{Q} \frac{\partial z_m}{\partial t} + \omega_m^2 z_m = F \cos(\Omega t) - D_{mmmm} z_m^3 \quad (44)$$

$$D_{mmmm} = \frac{2K}{\rho L} \int_0^L \delta(x) \left(\frac{\partial \psi_m}{\partial x} \right)^4 dx = \frac{2K}{\rho L} \left(\frac{m\pi}{L} \right)^4 \int_0^L \delta(x) \left(\sin \left(\frac{m\pi x}{L} \right) \right)^4 dx \quad (45)$$

In order to solve for the temporal portion of the displacement, the particular solution to the differential equation can be chosen as

$$z_m = A_m \cos(\Omega t + \phi_m) \quad (46)$$

This solution for z_m can then be plugged back into the wave equation. Next, by equating like coefficients in the wave equation, the following two equations can be determined where the only two unknowns are the amplitude, A_m , and phase, ϕ_m , of the displacement.

$$F = A_m \left[- \left(\Omega^2 - \omega_m^2 - \frac{3}{4} D_{mmmm} A_m^2 \right) \cos(\phi_m) - \left(\frac{\Omega^2}{Q} \right) \sin(\phi_m) \right] \quad (47)$$

$$0 = A_m \left[\left(\Omega^2 - \omega_m^2 - \frac{3}{4} D_{mmmm} A_m^2 \right) \sin(\phi_m) - \left(\frac{\Omega^2}{Q} \right) \cos(\phi_m) \right] \quad (48)$$

Simultaneously solving these two equations yields the following equation for the response amplitude.

$$A_m = \frac{F}{\sqrt{\left(\Omega^2 - \omega_m^2 - \frac{3}{4} D_{mmmm} A_m^2 \right)^2 + \left(\frac{\Omega^2}{Q} \right)^2}} \quad (49)$$

The resonance frequency for the peak resonance amplitude response can then be approximated as

$$\Omega_{res} \approx \frac{\omega_m \sqrt{1 + \frac{3}{4\omega_n^2} D_{mmmm} A_m^2}}{\sqrt{1 + \left(\frac{1}{Q} \right)^2}} \approx \Omega_{res}(0) \left(1 + \frac{3}{8\omega_n^2} D_{mmmm} A_m^2 \right) \quad (50)$$

Using the definition for the maximal strain amplitude of $\varepsilon_m = \frac{m\pi}{l} A_{m,max}$, the resonance frequency can be written as a function of the strain. Eq. 51 demonstrates that the resonance frequency due to cubic nonlinearity is a function of the square of the strain.

$$\Omega_{res} \approx \Omega_{res}(0) \left(1 + \frac{3}{4L} \varepsilon_m^2 \int_0^L \delta(x) \left(\sin \left(\frac{m\pi x}{L} \right) \right)^4 dx \right) \quad (51)$$

2.2.2.4 Hysteresis nonlinearity

In this section, only the effects of hysteresis are considered, and the classical nonlinearity components are set to zero ($\beta \equiv 0$ and $\delta \equiv 0$). With this consideration, the nonlinear wave equation is simplified to the following.

$$\begin{aligned} \frac{\partial^2 z_n}{\partial t^2} + \frac{\Omega}{Q} \frac{\partial z_n}{\partial t} + \omega_n^2 z_n \\ = F \cos(\Omega t) - \sum_{n,m} H_{nm} \left[\operatorname{sgn} \left(\frac{\partial z_m}{\partial t} \right) (A_m^2 - z_m^2) - 2A_m z_m \right] \end{aligned} \quad (52)$$

The first step is to find all of the oscillating terms on the right-hand side of Eq. 52 with circular frequencies that are approximately equal to $n/m \Omega \approx \omega_h$ because these are the only terms that contribute to the amplitude of $z_n(t)$. This is done by expressing the sign function as a Fourier series as seen in Eq. 53. The sine function in the Fourier series shows that only odd harmonics will be generated. Additionally, no other oscillating terms on the right-hand side of Eq. 52 contain even multiples of Ω meaning that hysteresis will only result in odd harmonics.

$$\begin{aligned} \operatorname{sgn} \left(\frac{\partial z_m}{\partial t} \right) &= \operatorname{sgn}(-\Omega A_m \sin(\Omega t + \phi_m)) \\ &= - \sum_{k=0}^{\infty} \frac{4}{(2k+1)\pi} \sin((2k+1)(\Omega t + \phi_m)) \end{aligned} \quad (53)$$

Using this definition for the sign function and choosing a sinusoidal excitation frequency close to mode m ($n=m$), the nonlinear wave equation can be written as seen in Eq. 54 where the three dots represent terms associated with higher order oscillation frequencies.

$$\begin{aligned} \frac{\partial^2 z_m}{\partial t^2} + \frac{\Omega}{Q} \frac{\partial z_m}{\partial t} + \omega_m^2 z_m & \\ &= F \cos(\Omega t) \\ &- H_{mm} \left[\frac{-8}{3\pi} A_m^2 \sin(\Omega t + \phi_m) - 2A_m^2 \cos(\Omega t + \phi_m) + \dots \right] \end{aligned} \quad (54)$$

It is assumed that the displacement term z_m will be of the same form seen in the linear solution: $z_m = A_m \cos(\Omega t + \phi_m)$ where the amplitude and phase are unknown and will be solved for by plugging z_m into Eq. 54. After plugging in z_m , the coefficients between corresponding terms (for both $\cos(\Omega t)$ and $\sin(\Omega t)$) can be equated as seen in Eq. 55 and Eq. 56.

$$F = A_m \left[-(\Omega^2 - \omega_m^2 + 2H_{mm}A_m) \cos(\phi_m) - \left(\frac{\Omega^2}{Q} + \frac{8}{3\pi} H_{mm}A_m \right) \sin(\phi_m) \right] \quad (55)$$

$$0 = A_m \left[(\Omega^2 - \omega_m^2 + 2H_{mm}A_m) \sin(\phi_m) - \left(\frac{\Omega^2}{Q} + \frac{8}{3\pi} H_{mm}A_m \right) \cos(\phi_m) \right] \quad (56)$$

These two equations can be solved simultaneously to obtain the displacement amplitude, A_m which can be seen in Eq. 57.

$$A_m = \frac{F}{\sqrt{(\Omega^2 - \omega_m^2 + 2H_{mm}A_m)^2 + \left(\frac{\Omega^2}{Q} + \frac{8}{3\pi}H_{mm}A_m\right)^2}} \quad (57)$$

This solution provides a relationship between the response amplitude and the drive frequency for a fixed excitation amplitude. Similar to the linear situation, the resonance frequency is the frequency at which the response amplitude is maximum. If it is assumed that there are only small nonlinear contributions, the resonance frequency can be written as the following where it can be approximated as a function of the resonance frequency at a minimal excitation amplitude.

$$\begin{aligned} \Omega_{res}(A_m) &= \frac{\omega_m \sqrt{(1 - 2/\omega_m^2)(1 + 4/3\pi Q)H_{mm}A_m}}{\sqrt{1 + 1/Q^2}} \\ &\approx \Omega_{res}(0) \left(1 - \frac{1}{\omega_m^2} \left(1 + \frac{4}{3\pi Q}\right) H_{mm}A_m\right) \end{aligned} \quad (58)$$

It is of interest to relate the resonance frequency to the maximal strain amplitude. The maximal strain amplitude is dependent on the excitation mode and is a function of the maximum response amplitude and can be written as Eq. 59.

$$\varepsilon_m = \frac{m\pi}{L} A_{m,max} \quad (59)$$

This equation is then substituted into the resonance frequency equation for the response amplitude, and the equation for the resonance frequency as a function of the strain can be written as the following.

$$\begin{aligned}\Omega_{res}(\varepsilon_m) &\approx \Omega_{res}(0) \left(1 - \left(1 + \frac{4}{3\pi Q} \right) \frac{cH_{mm}\varepsilon_m}{\omega_m^3} \right) \\ &= \Omega_{res}(0) \left(1 - \left(1 + \frac{4}{3\pi Q} \right) \frac{\varepsilon_m}{L} \int_0^L dx \alpha(x) \left| \sin^3 \left(m \frac{\pi}{L} x \right) \right| \right)\end{aligned}\quad (60)$$

Eq 60 shows that for hysteretic nonlinearity the relative frequency shift is a linear function of the strain which is the same result that has been seen across the literature [28,36–42]

2.2.2.5 Resonance frequency response for forced vibration

Now that each portion (linear and nonlinear) of the nonlinear wave equation for forced vibration has been considered on its own, let's combine all the contributions to determine the response of the material. Through the derivations, it was seen that the linearity portion, cubic nonlinearity portion, and hysteretic nonlinearity portion will all contribute to the resonance response of the material while the quadratic nonlinearity portion vanishes. The contributions to the resonance frequency from the cubic nonlinearity and hysteretic nonlinearity can be seen again in Eqs. 61 and 62, respectively. These equations show very clearly that the resonance frequency due to cubic nonlinearity has a quadratic relationship with the strain while the resonance frequency due to hysteretic nonlinearity has a linear relationship with the strain. Both resonance

frequencies are functions of the resonance frequency at minimal amplitude ($\Omega_{res}(0)$, linear). The response of the resonance frequency can be seen qualitatively in Figure 2.

$$\Omega_{res} = \Omega_{res}(0) \left(1 + \frac{3}{4L} \varepsilon_m^2 \int_0^L \delta(x) \left(\sin \left(\frac{m\pi x}{L} \right) \right)^4 dx \right) \quad (61)$$

$$\Omega_{res} = \Omega_{res}(0) \left(1 - \left(1 + \frac{4}{3\pi Q} \right) \frac{\varepsilon_m}{L} \int_0^L dx \alpha(x) \left| \sin^3 \left(m \frac{\pi}{L} x \right) \right| \right) \quad (62)$$

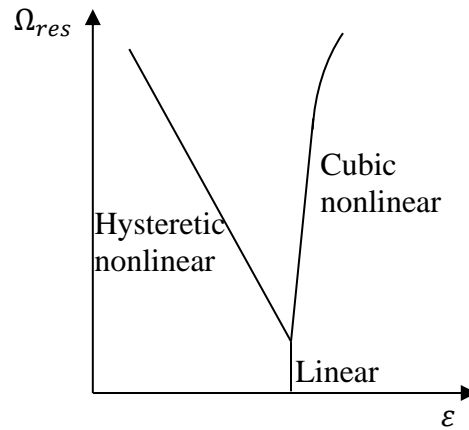


Figure 2. Resonance frequency response from change in strain for each linear and nonlinear portion

The contributions from each portion can be combined to determine the overall response of the material as seen below. This research will only be dealing with situations in the perturbation regime where the strain levels are very small ($\varepsilon_m \ll 1$). With strain levels so small, the higher order term goes to zero. Consequently, it can be assumed that the response of the resonance frequency is solely due to the hysteretic nonlinearity for this forced resonance case. The NRUS measurements conducted in this research follow

the conditions and assumptions listed in this section. This leads to the conclusion that the changes in α seen in this research are due only to hysteretic nonlinearity.

$$\begin{aligned} \Omega_{res} = \Omega_{res}(0) & \left(1 + \frac{3}{4L} \varepsilon_m^2 \int_0^L \delta(x) \left(\sin\left(\frac{m\pi x}{L}\right) \right)^4 dx \right. \\ & \left. - \left(1 + \frac{4}{3\pi Q} \right) \frac{\varepsilon_m}{L} \int_0^L dx \alpha(x) \left| \sin^3\left(m \frac{\pi}{L} x\right) \right| \right) \varepsilon_m \gg \varepsilon_m^2 \end{aligned} \quad (63)$$

$$\Omega_{res} \cong \Omega_{res}(0)[1 - \varepsilon A] \quad (64)$$

2.3 Theoretical derivations of contributions to nonlinearity

2.3.1 Classical quadratic nonlinearity

This section will explore the theoretical derivations for β from dislocation pinning and precipitate pinned dislocations.

2.3.1.1 Dislocation pinning

The theoretical model for the effect of dislocation pinning on the acoustic nonlinearity parameter was originally proposed by Hikata et al [31]. In this model, a dislocation line segment that has been pinned at two points a distance of $2L$ apart is considered. This pinning may be due to grain boundaries, other dislocations, or point defects in the material. When a small longitudinal stress, σ , is applied to this dislocation segment, it will bow between the two pinning points forming a circular arc with a radius of r . This stress is small enough that the dislocation does not break away from the

pinning points. The shear stress component can be related to the longitudinal stress through the Schmid factor: $\tau = R\sigma$.

If the dislocation density is small enough, the bowing of the dislocation segment will have no effect on the surrounding dislocations, and the line tension can be written as $T = Gb^2/2$ where G is the shear modulus and b is the Burgers' vector and the shear stress can be written as the following equation.

$$\tau = \frac{T}{rb} = \frac{Gb}{2r} \quad (65)$$

The corresponding shear strain, γ_d , from the dislocation can then be resolved as a function of the dislocation density, Λ , and the area swept by the dislocation segment, $S = r^2 \left(\theta - \frac{1}{2} \sin(2\theta) \right)$.

$$\gamma_d = \frac{\Lambda b}{2L} S \quad (66)$$

The angle θ can be approximated as $\theta = \sin^{-1}(L/r)$ and then expanded as a power series up the fifth power. Using this expansion along with Eq. 65, the shear strain can be expanded as the following equation.

$$\gamma_d = \frac{2}{3} \left(\frac{\Lambda L^2}{G} \right) \tau + \frac{4}{5} \left(\frac{\Lambda L^4}{G^3 b^2} \right) \tau^3 \quad (67)$$

This shear strain from dislocations can then be combined with the lattice strain, ε_l , to get the total strain, ε , in the material where Ω is the conversion factor from shear to longitudinal strain.

$$\varepsilon = \varepsilon_l + \Omega\gamma_d \quad (68)$$

Using the expression for the classical quadratic nonlinear stress-strain relationship to determine the lattice strain, the equation for the total strain can be expanded to the following equation.

$$\varepsilon = \left(\frac{1}{E_1} + \frac{2\Omega\Lambda L^2 R}{3G} \right) \sigma + \frac{E_2}{E_1^3} \sigma^2 + \left(\frac{4\Omega\Lambda L^4 R^3}{G^3 b^2} \right) \sigma^3 \quad (69)$$

Now consider the case where a small oscillatory stress, $\Delta\sigma$ is applied to the dislocation segment in addition to the internal stress, σ , where the oscillatory stress can be written as the following equation and is a function of the additional strain of $\Delta\varepsilon$.

$$\Delta\sigma = \left(\frac{1}{E_1} + \frac{2\Omega\Lambda L^2 R}{3G} \right)^{-1} \Delta\varepsilon - \left(\frac{E_2}{E_1^3} + \frac{12\Omega\Lambda L^4 R^3}{5G^3 b^2} \sigma \right) \left(\frac{1}{E_1} + \frac{2\Omega\Lambda L^2 R}{3G} \right)^{-3} \Delta\varepsilon^2 \quad (70)$$

The classical nonlinearity parameter can be found by comparing the form of Eq. 70 to the classical nonlinear stress-strain relationship where β is the negative ratio of the coefficients of the first two terms. From this, the total nonlinearity parameter can be defined as the following equation.

$$\beta_{tot} = \left(-\frac{E_2}{E_1^3} + \frac{24\Omega\Lambda L^4 R^3}{5G^3 b^2} \sigma \right) \left(\frac{1}{E_1} + \frac{2\Omega\Lambda L^2 R}{3G} \right)^{-2} \quad (71)$$

For most materials, the ratio $\frac{2\Omega\Lambda L^2 R}{3G}$ can be assumed to be much smaller than $\frac{1}{E_1}$, and β_{tot} can be simplified to the following equation.

$$\beta_{tot} = \left(-\frac{E_2}{E_1} + \frac{24\Omega\Lambda L^4 R^3 E_1^2}{5G^3 b^2} \sigma \right) \quad (72)$$

The ratio of Young's modulus $\frac{E_2}{E_1}$ is known as the lattice nonlinearity so the change in the classical nonlinearity parameter can be written as the following equation.

$$\Delta\beta = \frac{24\Omega\Lambda L^4 R^3 E_1^2}{5G^3 b^2} \sigma \quad (73)$$

2.3.1.2 Precipitate pinned dislocations

This section will consider the contribution of precipitate pinned dislocations to β . The theoretical model for precipitate pinned dislocations was developed by Cantrell and Yost [15]. In their model, they start with the derivation for a pinned dislocation segment (Eq. 73) and define an expression for the radial stress caused by the precipitate. Figure 3 gives a schematic of a precipitate pinned dislocation where the two pinning precipitates and one bending precipitate can be seen.

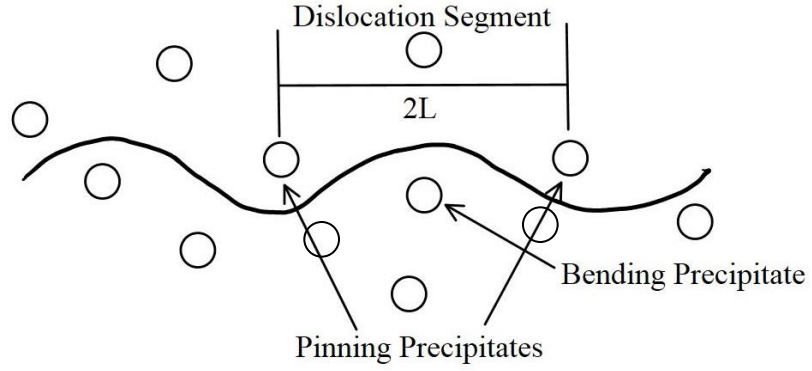


Figure 3. Precipitate pinned dislocation segment

In this model, Cantrell and Yost consider precipitates that are spherical, elastically isotropic, and randomly distributed throughout the material. The radial stress in the material stems from the mismatch between the lattice structures of the precipitate and the matrix. Cantrell and Yost define this radial stress seen in Eq. 74 as a function of the radius of the spherical precipitate, r_1 , where δ is the misfit parameter between the precipitate and the matrix.

$$\sigma = -\frac{4G\delta r_1^3}{(L/2)^3} \quad (74)$$

This equation for the radial stress can be plugged into Eq. 73 to get the following equation for the change in classical nonlinearity due to precipitate pinned dislocations.

$$\Delta\beta = 154 \frac{\Omega\Lambda LR^3 C_{11}^2 |\delta| r_1^3}{G^2 b^2} \quad (75)$$

In this equation, all of the variables are material constants except for L and r_1 . The radius of the precipitate can be defined as a function of the critical radius, r_{crit} , the volume fraction of critical radii, f_n , and the volume fraction of growing radii, f_g , seen in the equation below.

$$r_1 = r_{crit} \left(1 + \frac{f_g}{f_n} \right)^{1/3} \quad (76)$$

Since it is assumed that the precipitates are randomly distributed throughout the matrix, L can be defined as a function of the critical precipitate radius and the volume fraction of critical radii.

$$L = \left(\frac{4\pi}{3} \right)^{1/3} \frac{r_{crit}}{f_n^{1/3}} \quad (77)$$

These definitions for the precipitate radius and the loop length can be plugged back into Eq. 75 to get the following equation.

$$\Delta\beta = 248 \frac{\Omega\Lambda R^3 C_{11}^2 |\delta| r_{crit}^4}{G^2 b^2} (f_n^{-1/3} + f_n^{-4/3} f_g) \quad (78)$$

In order to account for differences between the elastic properties of the precipitate and the matrix, Hurley et al. modified the above model by developing a new expression for the radial stress around the precipitate [16]. In their model, the radial stress (Eq. 79) is

a function of the bulk modulus of the precipitate, B , and the shear modulus of the matrix, G .

$$|\sigma| = 2|\sigma_{rr}| = \frac{64Gr_1^3\delta}{(L)^3} \left[\frac{3B}{3B + 4G} \right] \quad (79)$$

The expression for the radial stress can be plugged into the model from Cantrell and Yost. Assuming that the average precipitate radius is the critical radius and that all of the growing precipitates are at the critical size, the following expression can be written for $\Delta\beta$.

$$\Delta\beta = 495 \frac{\Omega\Lambda R^3 C_{11}^2 |\delta| r_{avg}^4}{G^2 b^2 f_n^{1/3}} \left[\frac{3B}{3B + 4G} \right] \quad (80)$$

2.3.2 *Nonclassical hysteresis nonlinearity*

While there have been several models proposed for classical quadratic nonlinearity, there are still few models for nonclassical hysteresis nonlinearity because not much is known about the physics of the hysteresis mechanisms. Right now, a model developed by Granato and Lücke which investigates the effect of dislocations on hysteresis is one of the few models available for explaining hysteresis nonlinearity [43]. In this model, they consider a dislocation line that has been pinned in multiple locations as seen in Figure 4. This dislocation line is then subjected to an external stress which will cause an elastic strain as well as a dislocation strain from the dislocations in the material. Figure 4 shows the dislocation segment as the stress increases on the material. (A) shows the dislocation

segment pinned down with no external stress. When the external stress is very small, the individual loops will begin to bow. As the amount of stress is increased, the loops will bow even further until the breakaway stress is reached (C to D). As breakaway from the pinning points occurs, the strain level will continue to increase while the stress level remains the same. As the stress level increases even further, this new longer dislocation segment will continue to bow as seen in D to E. In this model, it will be assumed that the network pins (the pins at the ends of the dislocation segment) are so strong that there will be no break away from these pins. If the stress is increased even further, then new closed dislocation loops will form and the damage will be irreversible (plastic strain, F to G).

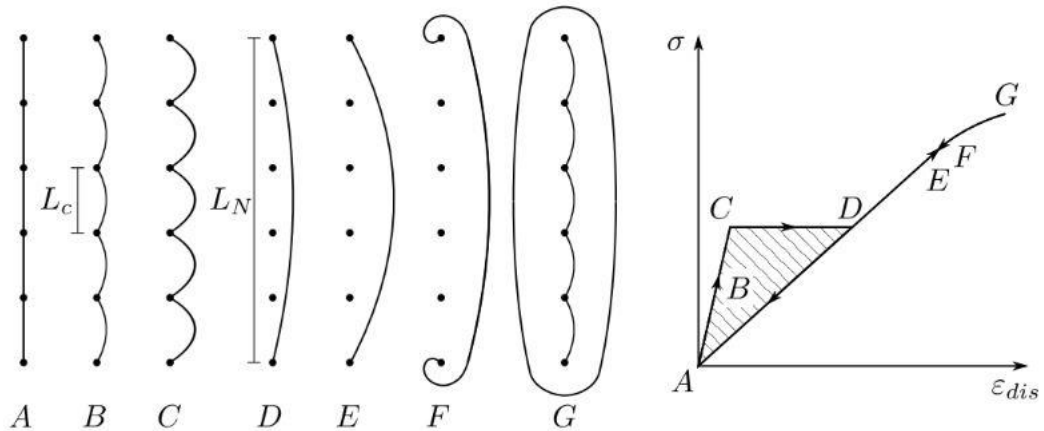


Figure 4. Dislocation pinning model showing increasing stress on the dislocation segment, also showing the stress-dislocation strain relationship– from Granato and Lüke [43]

This model looks at the loss due to damping mechanisms. The Granato and Lüke model considered in this research will be the frequency dependent model because of its resonance nature and the applied stresses are still relatively small. The equation of motion for this model can be seen in the equation below where the strain is the sum of the elastic strain and the dislocation strain: $\gamma = \gamma_{el} + \gamma_{dis}$.

$$\frac{\partial^2 \tau}{\partial x^2} - \rho \frac{\partial^2 \gamma}{\partial t^2} = 0 \quad (81)$$

The elastic strain can be determined through elasticity theory: $\gamma_{el} = \tau/G$, and the dislocation strain can be calculated from the displacement of the dislocation. The average displacement of the dislocation segment with length l can be written as the following where y is along the dislocation line:

$$\bar{\xi} = \frac{1}{l} \int_0^l \xi(y) dy \quad (82)$$

The strain from the dislocations can then be written as the following equation where Λ is the total amount of moveable dislocation length and a is the Burger's vector.

$$\gamma_{dis} = \frac{\Lambda a}{l} \int_0^l \xi(y) dy \quad (83)$$

The dislocation displacement can then be related to the applied shear stress through the following equation where A is the effective mass per unit length, B is the damping force per unit length, and C is the force from the tension of bowed dislocation per unit length. The boundary conditions are the displacement is zero at the ends of the dislocation segment.

$$A \frac{\partial^2 \xi}{\partial t^2} + B \frac{\partial \xi}{\partial t} - C \frac{\partial^2 \xi}{\partial y^2} = a\tau \quad (84)$$

$$A = \pi\rho a^2$$

$$C = \frac{2Ga^2}{\pi(1-\nu)}$$

The equation of motion, average displacement, dislocation strain, and displacement-stress relationship can be combined to get the following system of equations.

$$\frac{\partial^2 \tau}{\partial x^2} - \frac{\rho}{G} \frac{\partial^2 \tau}{\partial t^2} = \frac{\Lambda \rho a}{l} \frac{\partial^2}{\partial t^2} \int_0^l \xi(y) dy \quad (85)$$

$$A \frac{\partial^2 \xi}{\partial t^2} + B \frac{\partial \xi}{\partial t} - C \frac{\partial^2 \xi}{\partial y^2} = a\tau$$

It is of interest to consider a shear stress that is periodic in time and independent of y as written below, and the dislocation lines are normal to the wave propagation direction.

$$\tau = \tau_0 e^{-ax} e^{i\omega(t-x/v)} \quad (86)$$

Knowing the shear stress in the material, the displacement can be solved for as the following equation where $d = B/A$, $\omega_n = (2n + 1)\pi/l\sqrt{C/A}$, and $\delta_n = \tan^{-1}(\omega d/(\omega_n^2 - \omega^2))$. If the damping is not small, the higher order terms of this series are negligible so the first term of the series will be the only one considered.

$$\xi = 4a\tau \sum_{n=0}^{\infty} \frac{1}{2n+1} \sin\left(\frac{(2n+1)\pi y}{l}\right) \frac{e^{i(\omega t - \delta_n)}}{[(\omega_n^2 - \omega^2) + (\omega d)^2]^{1/2}} \quad (87)$$

Using these equations for the shear stress and displacement, the attenuation and velocity of the stress wave can be defined as the following equations where $v_0 = \sqrt{G/\rho}$, $\Delta_0 = 8G a^2/\pi^3 C$, and $\eta^2 = \pi^2 C/A$.

$$\alpha = \frac{\omega}{2v} \frac{\Lambda \Delta_0 \eta^2}{\pi} \frac{\omega d}{(\omega_0^2 - \omega^2) + (\omega d)^2} \quad (88)$$

$$v = v_0 \left[1 - \frac{\Lambda \Delta_0 \eta^2}{2\pi} \frac{\omega_0^2 - \omega^2}{(\omega_0^2 - \omega^2) + (\omega d)^2} \right] \quad (89)$$

The decrement, Δ , can be defined as the energy lost per cycle, ΔW over the total vibrational energy of the specimen, W and can also be related to the attenuation, velocity, and frequency.

$$\Delta = \frac{\Delta W}{2W} = \frac{\alpha 2\pi v}{\omega} \quad (90)$$

Knowing the terms for the attenuation and velocity, the decrement can be solved for in the following equation.

$$\Delta = \frac{\Lambda \Delta_0 L^2 d}{\omega_0} \left[\frac{\omega/\omega_0}{(1 - (\omega/\omega_0)^2)^2 + (\omega/\omega_0)^2/(\omega_0/d)^2} \right] \quad (91)$$

This derivation shows that for very small damping the decrement response is linear for frequencies up to the resonance frequency and then decreases and for large damping the is linear up to a point before the resonance frequency and then decreases through the

resonance frequency. Additionally, for small damping, the maximum loss occurs at the resonance frequency, and for large damping the maximum loss occurs at ω_0^2/d .

The loss is seen to be a function of the number of dislocations as well as the dislocation loop length. As the number of dislocations or loop length increases, the loss will increase. Since it cannot be assumed that all dislocations will have the same loop length in a material, an effective loop length must be determined. This derivation can be seen in full in Granato and Lücker's paper [43], but qualitatively, the loss will have the same response.

2.4 Nonlinear Ultrasound Resonant Spectroscopy

Nonlinear ultrasound resonant spectroscopy (NRUS) is a nonlinear ultrasound technique which looks at the shift in resonance frequency curves as a function of increasing excitation amplitude (in turn increasing strain) and is used to determine the nonlinearity parameter α associated with the nonclassical nonlinearity mentioned earlier. NRUS is an expansion of the linear resonance ultrasound spectroscopy (RUS) technique. RUS measures the equilibrium resonance frequency of a material and then uses the equilibrium resonance frequency to determine the stiffness parameters.

Figure 5 takes a look at a set of sample resonance curves that may be obtained using NRUS. A negative shift in the resonance frequency can be seen with increasing excitation amplitude indicating a softening of the material. From these resonance curves, one can determine the shift in the resonance frequency, Δf . The relationship between the shift in resonance frequency, the strain amplitude, $\Delta \epsilon$, and the hysteretic nonlinearity parameter, α , can be seen in Equation 92 where f is the resonance frequency of the current

excitation level and f_0 is the equilibrium frequency (resonance frequency at the lowest exciting level)

$$\frac{\Delta f}{f_0} = \frac{f - f_0}{f_0} = \alpha \Delta \varepsilon \quad (92)$$

The following section will explore how to determine the strain amplitude.

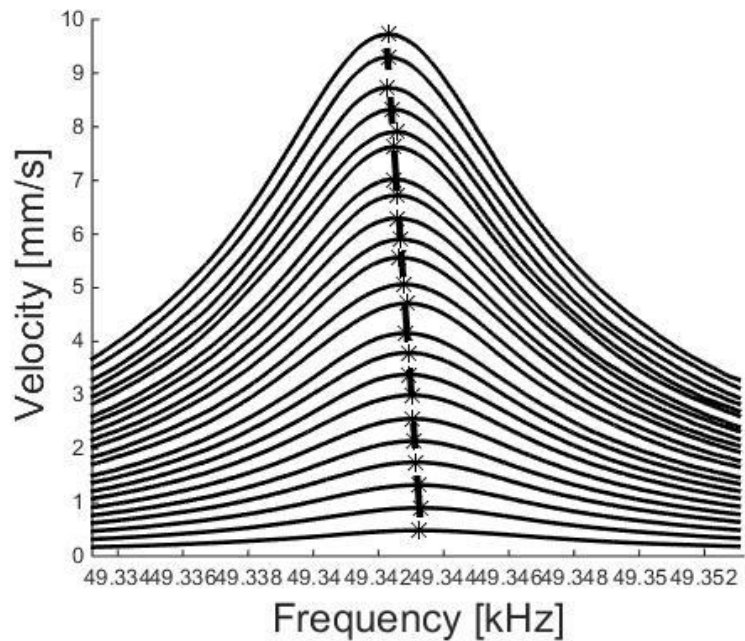


Figure 5. Sample NRUS resonance curves

2.4.1 *Vibration of 1D Bar*

While the resonance frequency and equilibrium resonance frequencies can be determined directly from the resonance curves, the determination of the strain amplitude is a little more complicated. To be consistent with the experimental setup used in this research, the vibration of a 1D thin bar with free-free boundary conditions will be

considered [44]. Additionally, the derivation of the natural frequencies of the bar will be considered.

2.4.1.1 Longitudinal Strain

Consider the bar shown in Figure 6 with a length of L and a constant cross-sectional area of A and two points marked on the bar at locations x and $x+dx$. Now by applying a force to the left end of the bar, both points will move a distance in the x -direction of u and $u+du$, respectively.

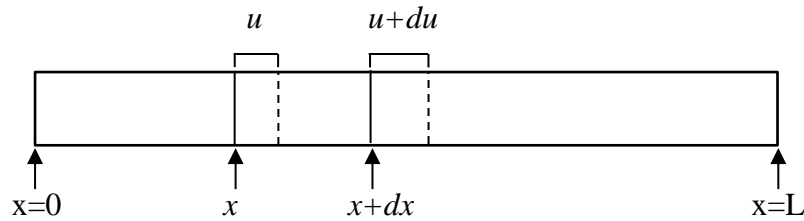


Figure 6. 1D Free-Free bar

In small strain situations, the displacement in the beam can be written as the following Taylor series with respect to x

$$u + du = u + \left(\frac{\partial u}{\partial x}\right) dx \quad (93)$$

Eq. 93 can be rearranged so that we get the change in displacement (increase in length) as follows

$$(u + du) - u = \left(\frac{\partial u}{\partial x}\right) dx \quad (94)$$

Eq. 94 can then be divided by x to get an equation for the strain

$$\varepsilon = \frac{\left(\frac{\partial u}{\partial x}\right) dx}{x} = \frac{v}{c} \quad (95)$$

where v is the velocity at the end of the bar and c is the wave velocity.

2.4.1.2 Natural Frequencies of a Free-Free Bar

Consider the 1D longitudinal wave equation seen below

$$\frac{1}{c^2} \frac{\partial^2 u}{\partial t^2} = \frac{\partial^2 u}{\partial x^2} \quad (96)$$

where

$$\mathbf{u} = \mathbf{A}e^{i(\omega t - kx)} + \mathbf{B}e^{i(\omega t + kx)} \text{ where } k = \frac{\omega}{c} \quad (97)$$

is the complex harmonic solution to this wave equation. Since we are considering the case where the boundary conditions are free-free, the strain amplitude $\left(\frac{\partial u}{\partial x}\right)$ at the ends of the bar ($x=0$ and $x=L$) will be equal to 0 leading to the following relationship between the amplitude coefficients

$$-A + B = 0 \rightarrow A = B \quad (98)$$

Using this relationship, Eq. 97 can be simplified to

$$\mathbf{u} = A e^{i\omega t} (e^{-ikx} + e^{ikx}) = 2A e^{i\omega t} \cos(kx) \quad (99)$$

By plugging in that the strain is equal to 0 at $x=L$, one gets $\sin(kL) = 0$ which leads to the conclusion of the natural frequencies where n is the mode number:

$$f_n = \frac{nc}{2L} \quad n = 1, 2, 3, \dots \quad (100)$$

The strain amplitude for the n -th mode can then be related to the natural frequency by relating Eqs. 95 and 100

$$\varepsilon_n = \frac{nv_n}{2Lf_n} \quad (101)$$

2.4.2 Resonant Ultrasound Spectroscopy (RUS)

The linear version of NRUS, RUS, can be used to determine Young's modulus, E , of the material. RUS measures the linear resonance frequency, f_0 , of the material by exciting the material at a sufficiently low strain amplitude. The linear frequency can then be related to Young's modulus using Eq 100 and the relationship $c = \sqrt{E/\rho}$.

$$E = \rho \left(\frac{2Lf_n}{n} \right)^2 \quad (102)$$

The experimental setup for the RUS measurements is the same as the setup used for the NRUS measurements seen in section 4.3.

2.5 Quality Factor

For an idealized system when vibration is initiated, wave motion will continue to increase indefinitely however this is in stark contrast to “real life” behavior. In “real life” materials, the amplitude of the wave motion will attenuate as the wave propagates. This attenuation can be due to a multitude of constraints, but they can be grouped into the category of internal friction. Quantitatively, this internal friction can be defined by a term known as the quality factor, Q . The quality factor is a method to quantify the amount of damping in the material. If the quality factor is large, then the system is said to have a small amount of damping, and similarly, if the quality factor is small, the system is said to have a large amount of damping.

Both linear and nonlinear quality factors can be defined. The linear quality factor is dependent on the resonance frequency but is independent of drive amplitude meaning that the resonance curves retain the same shape with increasing drive amplitude. The linear quality factor can be defined in multiple different ways but two manners are explored here: Q relating the energy in the system to the energy loss in the system and Q relating the resonance frequency to the half power frequencies. First, Q relating the energy in the

system to the energy loss in the system is defined. Eq. 103 defines the quality factor as the ratio of the peak energy stored in the system, E , and the energy lost each cycle, $-\Delta E$.

$$\frac{1}{Q(\omega)} = -\frac{\Delta E}{2\pi E} \quad (103)$$

If it can be assumed that the attenuation is linear (wave may be broken into Fourier components) and the medium has a linear stress-strain relationship, then the wave amplitude is proportional to the square root of the energy ($E^{1/2}$). If it is also assumed that $Q \gg 1$, then the quality factor can be written as a function of the amplitude as seen in Eq. 104.

$$\frac{1}{Q(\omega)} = -\frac{\Delta A}{\pi A} \quad (104)$$

Next, Q relating the resonance frequency to the half power frequencies is defined as seen in Eq. 105. f_0 is the resonance frequency of the system and f_u and f_l are the frequencies at the half power above and below resonance frequency.

$$Q = \frac{f_0}{(f_u - f_l)} \quad (105)$$

While a significant amount is known about linear hysteresis and the linear quality factor and this knowledge is important in the field of vibrations, it is important to note that this is not the same as the hysteresis nonlinearity being studied in this research. For materials with hysteresis nonlinearity, research has shown that the quality factor is a

function of the linear quality factor but is no longer linear. Van Den Abeele derived the quality factor for hysteretic nonlinearity in his modeling paper for NRUS [35] where this quality factor can be seen in Eq. 106 where H_{mm} is defined in Eq. 28, and other papers have shown similar results [36,38]. This Q factor accounts for the nonlinear damping.

$$\frac{1}{Q_N} = \frac{1}{Q_L} + \frac{8}{3\pi\omega_m^2} H_{mm} A_m = \frac{1}{Q_L} + \frac{8cH_{mm}\varepsilon_m}{3\pi\omega_m^3} \quad (106)$$

The equation for the nonlinear Q factor demonstrates that the loss factor is amplitude dependent meaning the Q factor will change depending on the excitation amplitude. This can be seen experimentally in the broadening of the resonance curves to the left with increasing input strain. It is important to note that this amplitude dependence of the Q factor is only seen in systems with hysteretic nonlinearity [35].

2.6 Analysis of variance (ANOVA)

The analysis of variance (ANOVA) test will be the statistical method used in this research to determine the statistical significance of the experimental results. Please note that this section is meant to give the reader a brief understanding of ANOVA and how to understand the results. For more detailed information on the mathematics, the reader is referred to the following textbook [45].

ANOVA is a statistical method used to test whether two or more means are significantly different. This is done by testing the null hypothesis and determining whether to reject it or accept the alternative hypothesis. The null hypothesis for an

ANOVA can be defined as no significant difference between groups and can be written as follows

$$H_0: \mu_1 = \mu_2 = \dots = \mu_L \quad (107)$$

For this research, the null hypothesis is written as: material change (such as growth in precipitate radius) has no effect on the values of either α or β (ie. even with a material change the mean value for both α and β will remain the same). The alternative hypothesis for an ANOVA can be defined as the averages for each of the groups are significantly different and can be written as the following

$$H_1: \textit{at least one of the means is different} \quad (108)$$

For this research, the alternative hypothesis is written as: material change will cause a change in the value of both α and β . If the null hypothesis is rejected and alternative hypothesis accepted, then the groups or in this instance mean values are said to be significantly different.

There are two main types of ANOVA tests: one-way and two-way where the difference is the number of independent variables. For a one-way ANOVA, there is one independent variable whereas for a two-way ANOVA, there are two independent variables. For this research, the one-way ANOVA will be used because there is only one material change per experimental group.

The data analysis toolbox in Excel is used to perform the ANOVA for the experimental results. This toolbox calculates the F-value, p-value, and F-critical for the data set. First, the F-value is compared to the F-critical, and if it is found to be larger, then it is said that there is a statistically significant finding. Next, the p-value is considered. The p-value says the percent chance that the finding is due to random error alone. The p-value is compared to the significance level, alpha, (which will be written out so that it is not confused with the hysteresis nonlinearity parameter). The significance level is the probability of falsely rejecting the null hypothesis and is typically chosen to be 0.05. If the p-value is found to be less than or equal to alpha, then the null hypothesis is rejected, and the mean values are said to be significantly different.

CHAPTER 3. MATERIAL DESCRIPTION

3.1 Overview

This chapter describes the materials and microstructural mechanisms studied in this research. Since this research investigates the effects of different microstructural mechanisms on the classical and nonclassical nonlinearity parameters, β and α , it is important to choose mechanisms that are known to be precursors to macroscale damage. A better understanding of these mechanisms allows for easier detection in the future. The mechanisms chosen for study in this research are: growth of precipitates in and along grain boundaries, dislocation removal, and precipitate growth in the grain structure (precipitate pinned dislocations). These mechanisms were primarily chosen for their ease of isolation allowing the ability to study a single mechanism at a time. This chapter will provide details for each of the materials studied and their relationship to a particular microstructural mechanism. It will also provide insight into the “ground truth” of the materials studied.

3.2 304 stainless steel

One of the material mechanisms studied in this research is the growth of precipitates along grain boundaries. This mechanism is investigated by looking at 304 stainless steel because of its susceptibility to sensitization and in turn intergranular stress corrosion cracking (IGSCC). As will be described in more detail below, sensitization is a known precursor to IGSCC making the detection of sensitization desirable. The research on this material extends a previous study where the researchers examined the sensitivity

of SHG to sensitization [29]. This research examines an annealed and a sensitized 304 sample. One sample was annealed at 1080°C for 30 min removing any cold working effects in the form of excessive dislocations and residual stresses. The second sample was annealed and subsequently heat treated at 675°C for 4 hr resulting in full sensitization. The following sections will provide an overview of IGSCC and sensitization to give the reader a better understanding of the material.

3.2.1 Intergranular stress corrosion cracking

IGSCC is a well-known and studied failure mechanism that occurs in a variety of materials. One situation that may see IGSCC is the austenitic stainless steels found in recirculating boiling water reactors (BWR). IGSCC has been known to be a problem in BWRs for over 40 years with incidents being documented since the 1960s [46]. While this is only one example, it will give the reader a better understanding of IGSCC and pave the way to why the detection of sensitization in 304 stainless steel is being studied.

Many instances of IGSCC in BWRs have been found in the weld heat affected zone (HAZ). This is due to the “ideal” conditions in the HAZ which leads to IGSCC. It is known that three conjoining factors (environment, stress, and susceptibility) must occur for IGSCC to occur as outlined in Figure 7 from [46]. The figure shows that before IGSCC occurs the three conditions of material susceptibility, stress, and environment all have to be met.

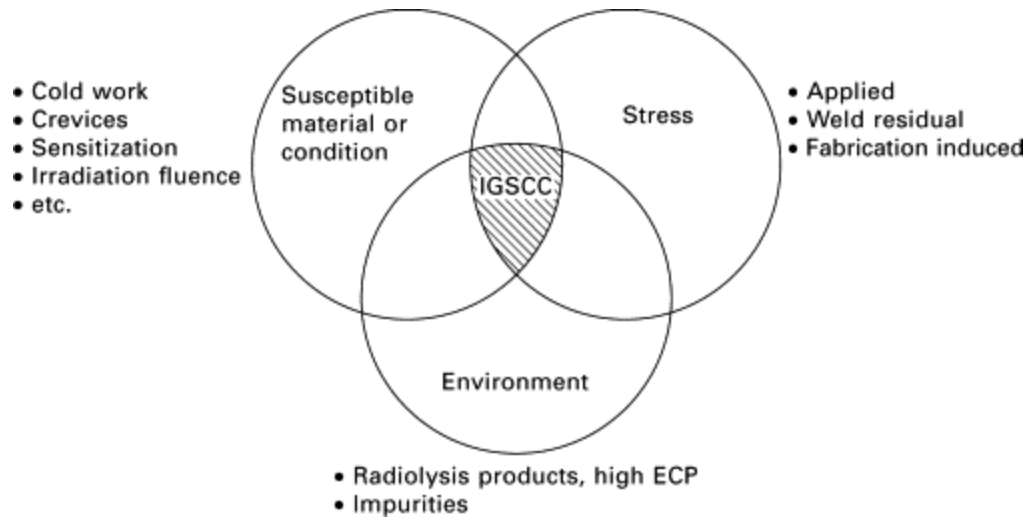


Figure 7. Combination of conditions which lead to IGSCC [46]

3.2.1.1 Sensitization

The material susceptibility focused on here will be sensitization. Austenitic stainless steels such as 304 and 316 are known to have corrosion resistance because of the chromium in the alloys. However, when these metals are either furnace heat treated or welded in the temperature range of ~550 to 850°C for a sufficient period of time, there will be a formation of chromium carbide precipitates at the grain boundaries. The formation of these carbides results in chromium depletion zones. These chromium depleted zones leave the material susceptible to aqueous corrosion.

Figure 8 shows the difference in the microscopy between a non-sensitized and fully sensitized sample [29]. In the image for the sensitized sample, one can see the formation of the chromium carbides at the grain boundaries.

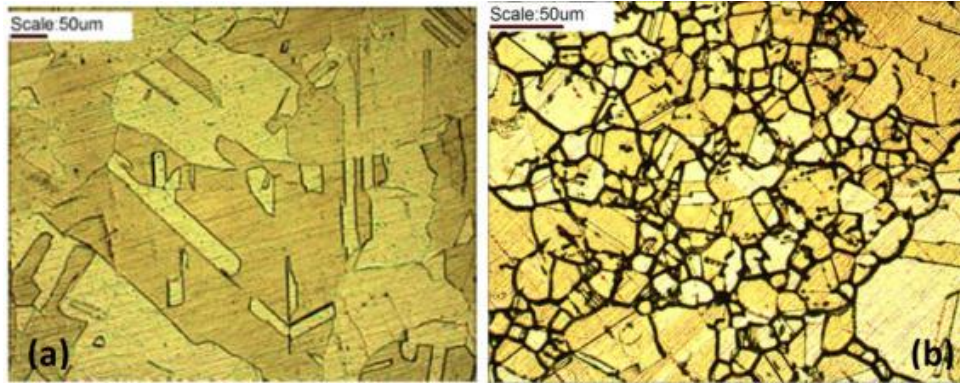


Figure 8. Microscopy showing a) non-sensitized sample and b) sensitized sample [29]

The effects of many factors on sensitization has been studied by researchers. One of the factors affecting sensitization is the carbon content in the material as well as exposure temperature and time. Figure 9 demonstrates the time-temperature-sensitization curves for increasing carbon contents [47]. The figure depicts that increased aging times are needed for a decrease in carbon content before sensitization occurs. It also has been seen that the degree of sensitization (DOS) is dependent on both the heat treatment temperature and time [48]. Additionally, it has also been seen that grain size [47,49], grain orientation/boundary conditions [50,51], and cold working [46,47,52] have an effect on sensitization.

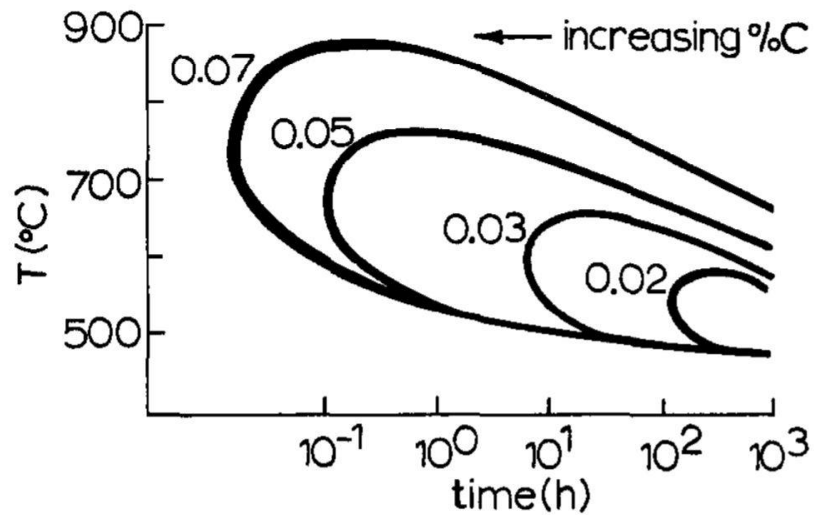


Figure 9. Time-temperature-sensitization curves for different amounts of carbon content [47]

3.2.1.2 Stresses

For the initiation of IGSCC, there must be tensile stresses in the material. Researchers have found three main sources of stress that may occur in BWRs [46] which will be referred to as fabrication stresses, primary stresses, and secondary stresses. Fabrication stresses result from any fabrication process such as machining, surface grinding, cold rolling, and welding. The stresses that occur from welding are of particular interest because there are many instances where the residual stress from the weld has led to IGSCC without any external stresses. Primary stresses are any stresses that occur from operational forces such as pressure load stress. Finally, secondary stresses include any other stresses such as thermal stress.

3.2.1.3 Environmental

The final category that influences the occurrence of IGSCC is environmental conditions. The corrosion potential of the environment is the tendency of the material to undergo corrosion in a particular environment. The higher the corrosion potential the more likely the material will experience corrosion.

3.2.2 *Electrochemical Reactivation (EPR)*

It is important to understand and estimate the degree of sensitization (DOS) as this research compares an annealed to a sensitized state. The DOS provides a measure of “ground truth” because it quantifies the chromium depletion along the grain boundaries due to the nucleation of chromium carbides and is a test completely independent of the nonlinear ultrasound measurements. The DOS was measured using the ASTM G108 test method for electrochemical reactivation (EPR) [53]. The EPR test consists of a process called reactivation where a potentiodynamic sweep is done from the passive to active regions of the electrochemical potentials and measures the charge generated by corrosion that occurs in the chromium depleted regions around chromium carbide precipitates. Please note that while the majority of the chromium carbides will be in the grain boundaries a few may be located in the grains and will still contribute to the total charge. As the electrochemical potential changes from passive to active, the chromium depleted regions react with the oxidizing acid solution and corrosion occurs. This corrosion results in a rapid increase of the current density. Since the chromium depleted regions of sensitized materials are known to be much more susceptible to corrosion than annealed unsensitized material, the increase in the current density is much higher in the sensitized

material than the annealed material. Please note that the EPR test is highly repeatable [53].

Figure 10 shows a qualitative comparison between sample reactivation curves for an annealed and sensitized sample [53]. The figure shows the much smaller rise in current density for the annealed sample than the sensitized sample.

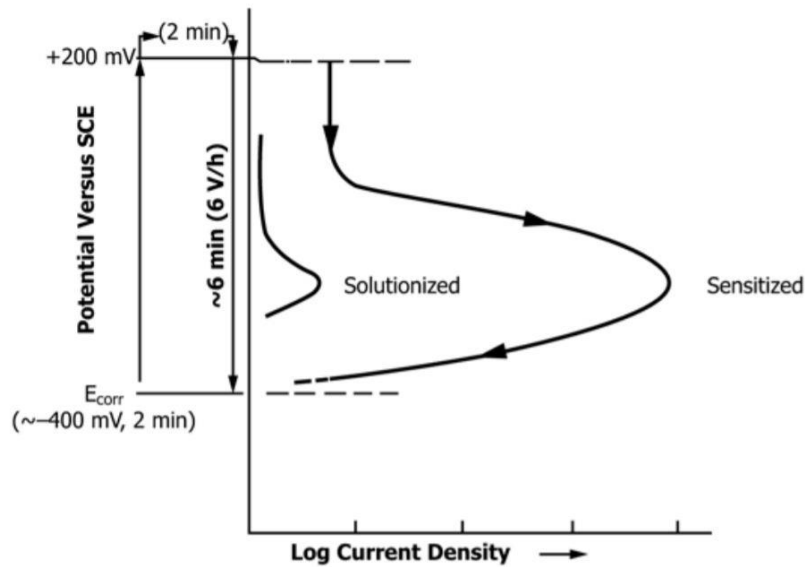


Figure 10. Sample reactivation curves from the ASMT standard showing the differences in sensitized and annealed samples [53]

Similar results were seen in the experimental measurements made by Doerr et al [29,54] where they compare the reactivation curves for annealed and sensitized 304 as seen in Figure 11 and Figure 12. These figures show a much larger increase in current density for the sensitized sample than the non-sensitized sample. Doerr et al performed a DOS test for each of their 304 stainless steel specimens and determined the peak current density for each specimen. They then normalized these peak current densities to the initial state (heat treatment time of 0) and plotted them as a function of the heat treatment

times to demonstrate the change in DOS as a function of heat treatment time as can be seen in Figure 13. This figure shows that the peak current density begins to level off at 240 minutes meaning that for this heat treatment time the sample is sensitized. These results are important because this material and heat treatments can be considered identical to the material studied in this research providing evidence that this research is looking at a non-sensitized and sensitized sample.

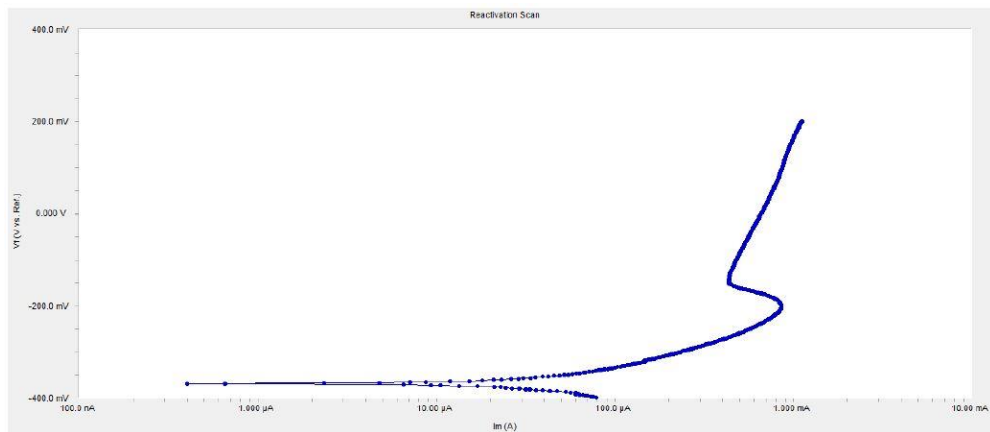


Figure 11. Reactivation curve for non-sensitized sample [54]

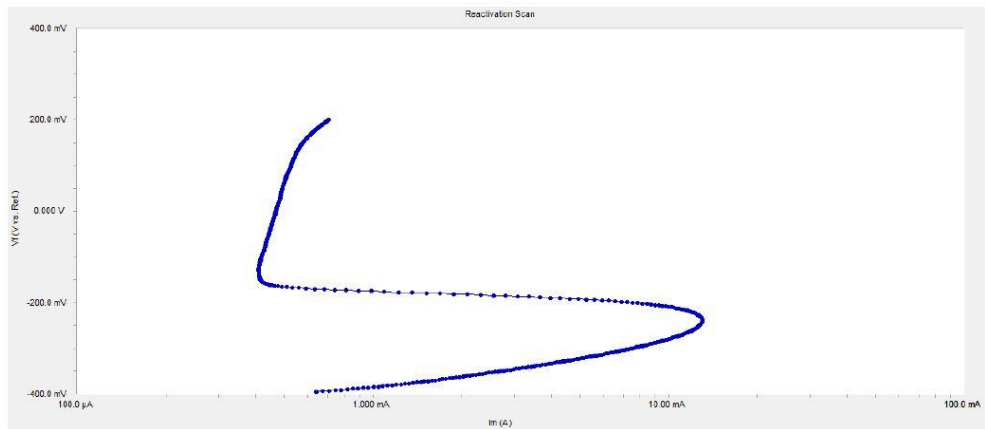


Figure 12. Reactivation curve for sensitized sample [54]

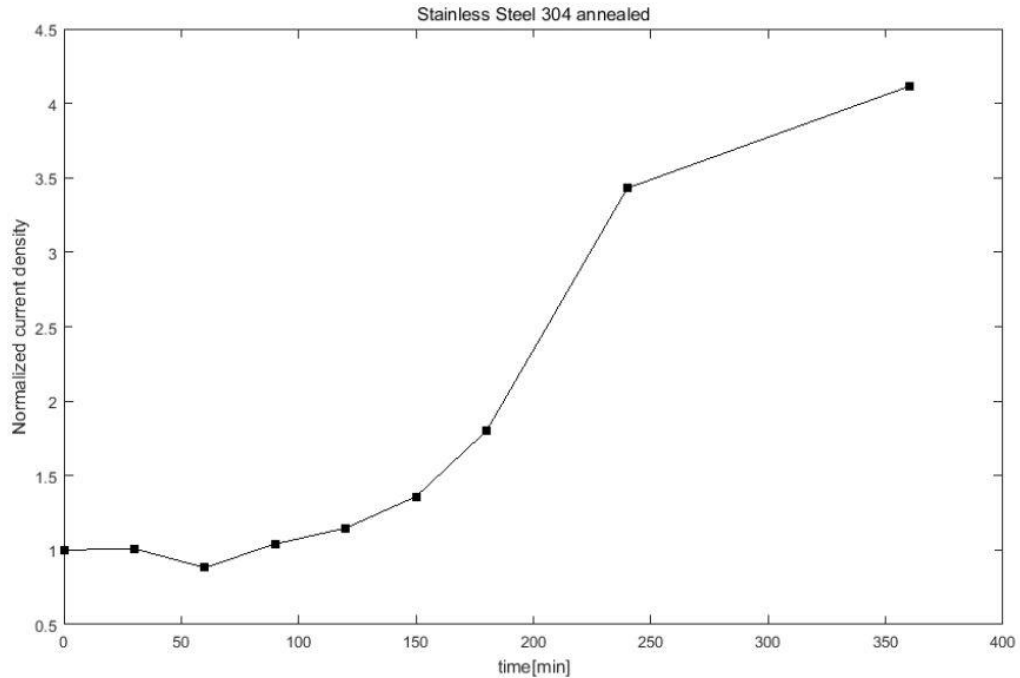


Figure 13. EPR results for 304 stainless steel [54]

3.2.3 Microscopy

Complementary to the EPR test, microscopy can be done to confirm the growth of chromium carbides in the grain boundaries. Doerr et al performed microscopy on all their 304 stainless steel samples which can be seen in Figure 14. This figure shows the growth of the chromium carbides in the grain boundaries in addition to a couple of chromium carbides that are intragranular. These microscopy results confirm the EPR results that the material is sensitized at 240 minutes again showing that the material studied in this research is sensitized.

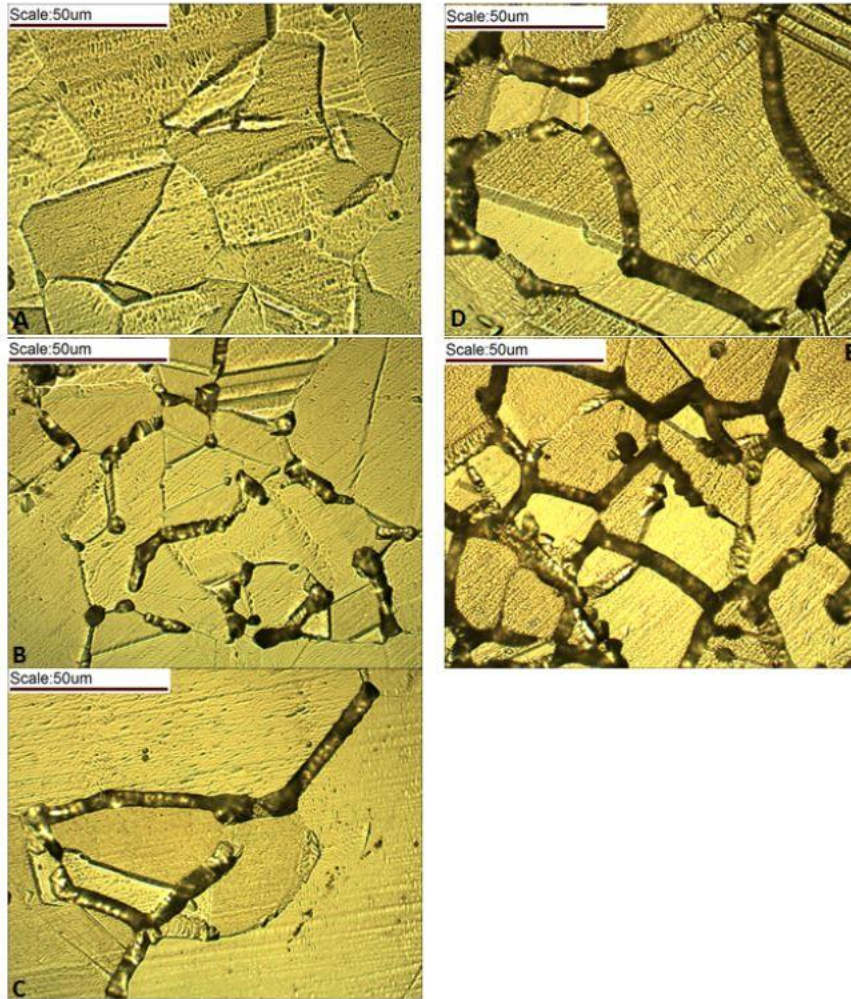


Figure 14. Microscopy for 304 stainless steel: a) 0 minutes, b) 150 minutes, c) 180 minutes, d) 240 minutes, e) 360 minutes [29,54]

3.3 316L stainless steel

Another set of specimens investigated in this research takes a look at the change in dislocation number as well as the relief of stresses when exposed to annealing temperatures. This was done by taking a set of as received 316L stainless steel specimens and heat treating them at 1325 K for 30 minutes. Heat treating stainless steel at this temperature is known to relieve residual stresses and remove dislocations.

Smith et al studied the behavior of forged and additively manufactured 304L austenitic steel to heat treatment at the annealing temperature [55]. Part of their research investigates the dislocation density change of geometrically necessary dislocation (GND) when the material is heat treated. The heat treatment schedule for the forged material is as follows: 973 K for 30 minutes, 1098 K for 30 minutes, and 1223 K for 30 minutes. They found that as the heat treatment temperature increased the density of the GNDs decreased as can be seen in Figure 15 where the maroon color represents lower dislocation density and the yellow color represents higher dislocation density. While the 304L (vs 316L) material is not the exact same material studied in this research, the chemical composition between the materials is very similar so the behaviors during annealing will be comparable. Therefore, it can be assumed that when the 316L is annealed the dislocation density will decrease. While it would be ideal to have the exact dislocation densities for the material studied, the measurements are still pending at Sandia National Lab.

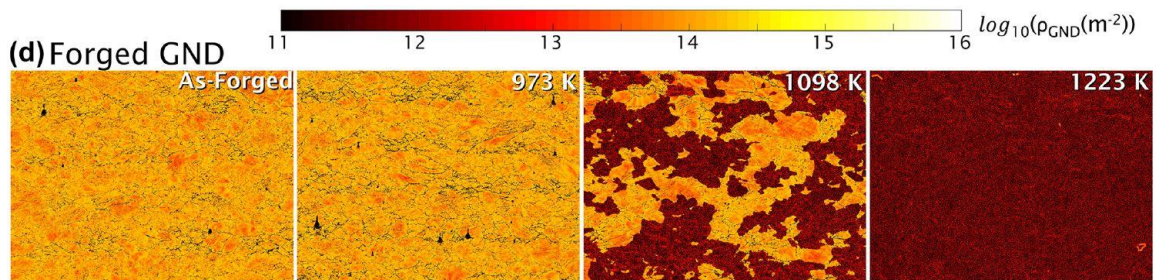


Figure 15. Dislocation density map of geometrically necessary dislocations showing decreasing dislocation density between the as-forged specimen and the heat treated specimens [55]

3.4 Fe-1.0%Cu Surrogate Specimens

The set of Fe-1.0%Cu specimens look at the microstructural mechanism of precipitate growth in the grains and serve as a set of surrogate specimens which simulate

radiation damage in light-water reactor pressure vessel (RPV) steel. Individual specimens were thermally aged at 500°C using the following heat treatment schedule: 5 hours, 15 hours, 30 hours, 100 hours, and 300 hours, respectively. This thermal aging promotes the nucleation and growth of Cu-precipitates and simulates varying amounts of radiation damage.

3.4.1 Radiation Embrittlement Background

Chronic radiation exposure seen by light water power reactors leads to the embrittlement of reactor pressure vessel (RPV) steel [56,57]. While embrittlement in the RPV steels is a very complicated process and depends on many variables such as chemical composition, neutron fluence, neutron flux, irradiation temperature, etc., studies have shown that this embrittlement is caused by a combination of multiple microstructural changes [58]. Examples of these microstructural changes include vacancies, microvoids, dislocation loops, and the formation of precipitates including clusters enriched with Cu, Mn, Ni, and Si, as well as phosphide formations, and carbide formations [56–60]. Despite the complexity of embrittlement, the causes of irradiation embrittlement on a basic level can be broken down into two main material changes, radiation hardening, which will be the focus of this research, and segregation of precipitates along the grain boundaries [61,62].

Radiation embrittlement is typically characterized by an increase of the ductile-to-brittle transition temperature (DBTT). The DBTT indicates the transition temperature between the low toughness brittle fracture region and the high toughness ductile fracture region. In this section, the focus on the mechanism causing this increase in DBTT will be material hardening. As precipitates nucleate and grow in RPV steel, the precipitates provide an obstacle to the motion of dislocations in the material. This hindrance to motion results in a hardening of the material as well as an increase in the yield strength of

the material [57,62–64]. This increase in the yield strength of the material induces an increase in the DBTT.

While there are many precipitates that form in RPV steel as irradiation occurs such as Mn, Ni, and Si, Odette et al have provided considerable evidence the main contribution to this hardening and consequently embrittlement is Cu rich precipitates (CRPs) [63,64]. In many of the RPVs in the United States, there is a significant amount of Cu present in the RPV steel coming from the use of recycled steel [58,62]. With Cu being one of the main variables contributing to radiation embrittlement and significant amounts of Cu can be found in RPV steel, it is desirable to study these Cu-precipitates through the use of surrogate specimens.

3.4.2 Manufacturing and Preparation of Surrogate Specimens

The set of Fe-Cu surrogate specimens were manufactured through the melting of pure Fe and pure Cu at the Korean Atomic Energy Research Institute (KAERI) and contained 1.0% by wt. Cu. Individual specimens were then thermally aged at 500°C using the following heat treatment schedule: 5 hours, 15 hours, 30 hours, 100 hours, and 300 hours, respectively. This thermal aging promotes the nucleation and growth of Cu-precipitates and simulates different amounts of radiation damage.

3.4.3 Interaction between Cu-precipitate and matrix

The Fe-Cu specimens investigated in this research are very similar to Fe-Cu material that has been studied extensively in the past. Many experimental measurements, as well as computer simulations, have been performed in order to better understand the

evolution of these Cu-precipitates and their interaction with the α -iron matrix as heat treatment time increases. In particular, the coherency of the Cu-precipitates and the α -iron matrix as precipitate radius grows is of interest

It is well known that as the Fe-Cu material is heat treated the structure of the Cu-precipitates transforms from the coherent BCC (body-centered cubic) structure to semi-coherent 9R structure to incoherent FCC (face-centered cubic) structure [65–70]. Even in the absence of an external force, coherent BCC Cu-precipitates cause internal compressive stress in the Fe-matrix due to a lattice mismatch between the Cu and Fe [7,68,71]. As the radii of the Cu-precipitates grow, this lattice mismatch results in larger compressive stresses. When the Cu-precipitates reach a critical radius, the compressive stress promotes the transition from the BCC to 9R structure [68,71].

Many studies have been performed to determine the critical transition radius for each of these structural transitions. Othen et al. showed that this transformation from BCC to 9R occurs when the Cu-particle size is between 4 to 5 nm and the transformation from 9R to FCC occurs when the Cu-particle size is approximately 18 nm [69].

Figure 16 [71] is provided to give the reader a visual understanding of this transformation from the BCC Cu-precipitates to the 9R Cu-precipitates. The 9R structure is much more complex than the BCC structure making it difficult to simply draw as a 2D schematic. However, this 2D depiction provides a basis for understanding the differences between the two structures.

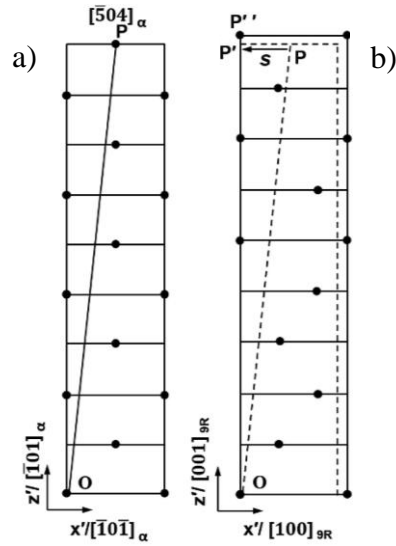


Figure 16. 2D depiction of a) BCC Cu-precipitates, b)9R Cu-precipitates [71]

3.4.3.1 Loss of coherency

As described in the section above, there is a loss of coherency when the Cu-precipitates transform from the BCC structure to the 9R structure (coherent to semi-coherent). Here, coherency is referring to the consistency in the atomic arrangements at the interface between the matrix and the precipitate phase (Fe and Cu). An interface is said to be coherent if the two crystals match perfectly and the lattice is continuous across the interface plane [72]. This occurs when the two crystals are oriented towards each other in the same atomic orientation. Figure 17a visually demonstrates a coherent interface where the continuous connection between the crystals can be seen.

As can be seen in Figure 17a, the “match” between the matrix and precipitate may not be perfect which leads to coherency strains. These strains contribute to the interfacial energy. For the Fe-Cu alloy as the radius of the Cu-precipitate grows, these strains increase which in turn increases the energy [66]. After a certain point, it is energetically

favorable for the interface to transition to a semi-coherent interface (microstructures favor configurations with the lowest energy) which is depicted in Figure 17b [66,72]. This transition to the semi-coherent interface occurs at the same time as the Cu-precipitate transitions from the BCC structure to the 9R structure [66,69].

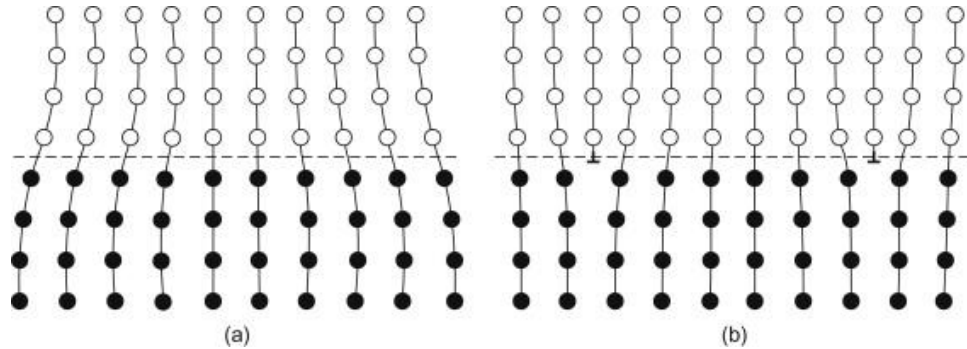


Figure 17. Interface between two crystals, a) coherent interface, b) semi-coherent interface [72]

3.4.4 Precipitate Radii of Fe-1.0% Cu Specimens

Measurement of the Cu-precipitate radii was performed on an identical set of Fe-1.0% Cu specimens at KAERI. These measurements determined the Cu-precipitate radii as a function of heat treatment time through small-angle neutron scattering (SANS) measurements conducted at the HANARO reactor [73]. These SANS measurements were completed using a neutron wavelength of 4.31 Å and a magnetic field of 1.2 tesla. These radii values provide a “ground truth” for nonlinear ultrasound measurements.

Figure 18 displays a graphical representation of the radii measurements and Table 1 displays the actual values of the exact radii measured. As can be seen from the figure, the radii of the Cu-precipitates increased as a function of increasing heat treatment time which was expected. While SANS data was only collected for heat treatment times of 5

hours to 100 hours, it is presumed that the precipitate radii will continue to increase as the heat treatment time is increased to 300 hours.

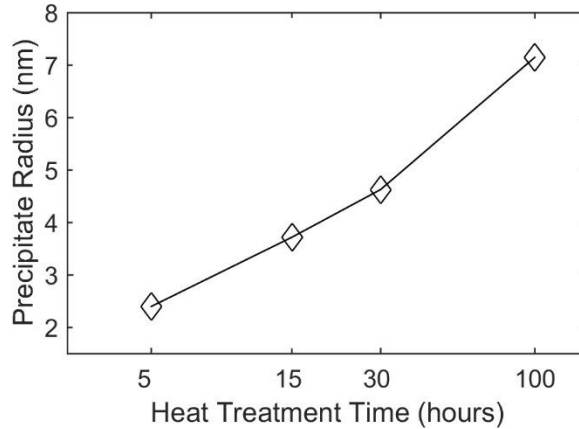


Figure 18. Cu-precipitate radius for Fe-1.0% Cu specimens

Table 1. Cu-precipitate radius of Fe-1.0% Cu specimens

Heat treatment time (hours)	5	15	30	100
Radius (nm)	2.4	3.72	4.63	7.15

As can be seen from Figure 18 and Table 1, at a heat treatment time of 30 hours, the radius of the Cu-precipitates is 4.63 nm. This indicates that a transition of the Cu-precipitates from BCC structure to 9R structure might be occurring after the 30-hour specimen. This conclusion is drawn from the fact that this radius falls in the transition range. This transition from the BCC structure to the 9R structure indicates a loss in coherency after the 30-hour specimen. While the precipitate radius continues to increase as heat treatment time increases, it is presumed that this set of specimens never reaches the transition from the 9R structure to the FCC structure because the largest precipitate

radii observed is 7.15 nm (while there is no data for the 300-hour specimen the precipitate radii is expected to be slightly larger than 7.15 nm) which is significantly below the transition radius of 18 nm.

CHAPTER 4. EXPERIMENTAL PROCEDURE

4.1 Overview

This chapter describes the experimental procedure for both the SHG and NRUS measurements. For the SHG measurements, two techniques are discussed: longitudinal waves and Rayleigh waves. The technique using longitudinal waves propagates a longitudinal wave through the thickness of the material using contact transducers. The technique using Rayleigh waves propagates a Rayleigh wave across the surface of the material, the transmitting transducer is a contact transducer, and the received transducer is air-coupled. For the NRUS measurements, the material is vibrated at a chosen longitudinal resonance mode using a completely noncontact setup.

4.2 SHG

As discussed earlier when looking at the SHG technique, a monochromatic signal with frequency f is introduced into a material where it interacts with microstructural features and generates a second harmonic wave (as well as higher harmonics) with frequency, $2*f$. Two different wave types can be used for SHG, surface propagation of Rayleigh waves or through thickness propagation of longitudinal waves.

This research will look at the use of Rayleigh waves to determine β for the 304 and 316L specimens and the use of longitudinal waves to determine β for the Fe-Cu specimens. Rayleigh wave measurements are the preferred SHG technique because it only requires access to one side of the material and reduces the amount of system nonlinearity. However, for the Fe-Cu specimens, despite numerous attempts, Rayleigh

waves could not be generated on the surface. This will be discussed more in the results section.

4.2.1 Rayleigh Wave Measurements

The Rayleigh wave instrumentation setup used for this thesis is the same as used in previous research [74,75] and can be seen in Figure 19. The experimental procedure for the Rayleigh wave measurements is as follows. A sinusoidal tone burst, frequency of 2.1 MHz and packet length of 20 cycles, was generated by a function generator (Agilent 33250a) and then amplified by a gated-amplifier (RITEC GA-2500A). The longitudinal wave signal was then transmitted from a commercial piezoelectric contact transducer to a Rexolite wedge which was then mounted on the material. The generation wedge was designed such that the wedge angle was equal to the critical angle for generating Rayleigh waves along the surface of the material. The transducer, wedge, and specimen were all coupled using a light layer of oil coupling to ensure better acoustic transmission between the components.

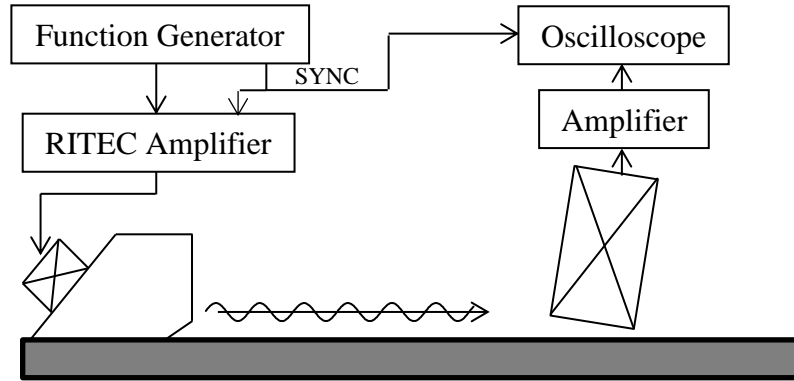


Figure 19. Rayleigh wave experimental setup

As the Rayleigh wave propagates along the length of the specimen, longitudinal waves are leaked off of the surface. These longitudinal waves were received by an air-coupled receiver (Ultran NCT4-D13, center frequency: 4 MHz). The center frequency of the air-coupled transducer was chosen to be twice that of the generating transducer for better detection of the small second harmonic. The use of an air-coupled receiver allows for fine tuning of the receiver location as well as the elimination of contact conditions between the specimen and the receiver. The received signal was then amplified and sent to an oscilloscope where the signal was averaged 512 times to reduce any noise effects. The signal was then saved for post-processing. The air-coupled transducer was then moved along the wave propagation path, and the measurement was repeated. Please see [75] for the information on how to calibrate the wave propagation path.

Once all of the measurement points have been completed, the data is processed to extract the amplitudes of the first and second harmonics, A_1 and A_2 . First, the raw time signal data is windowed using a Hanning window as seen in Figure 20. Extra care was taken to window only the steady state portion of the signal. The fast Fourier transform (FFT) (Figure 21) was then used to extract A_1 and A_2 . Figure 22 shows a sample plot of

A_1 and A_2 as a function of propagation distance. As can be seen in the figure, A_1 decreases as a function of propagation distance because of signal attenuation in the material. It can also be seen that A_2 increases as a function of propagation distance. This is due to compounding the second harmonic as propagation distance increases.

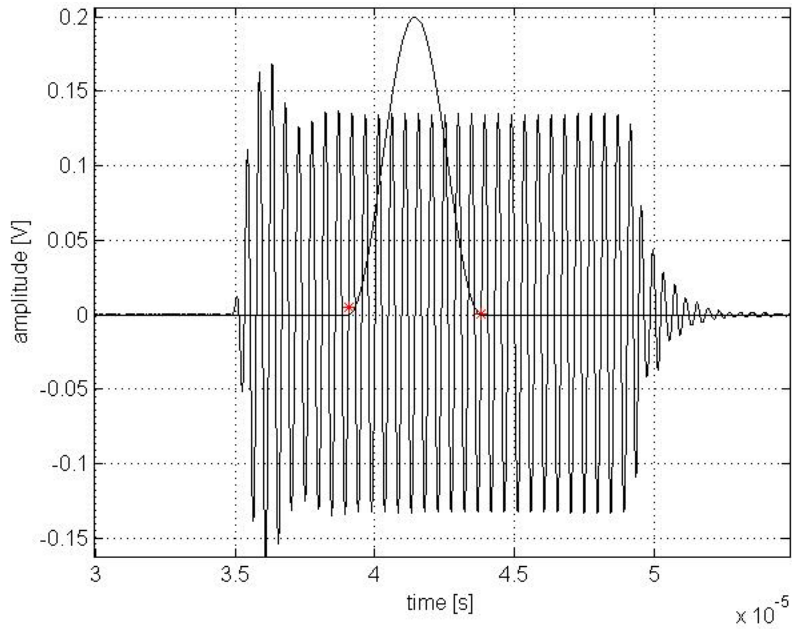


Figure 20. Sample time domain plot with figurative Hanning window for Rayleigh wave measurements

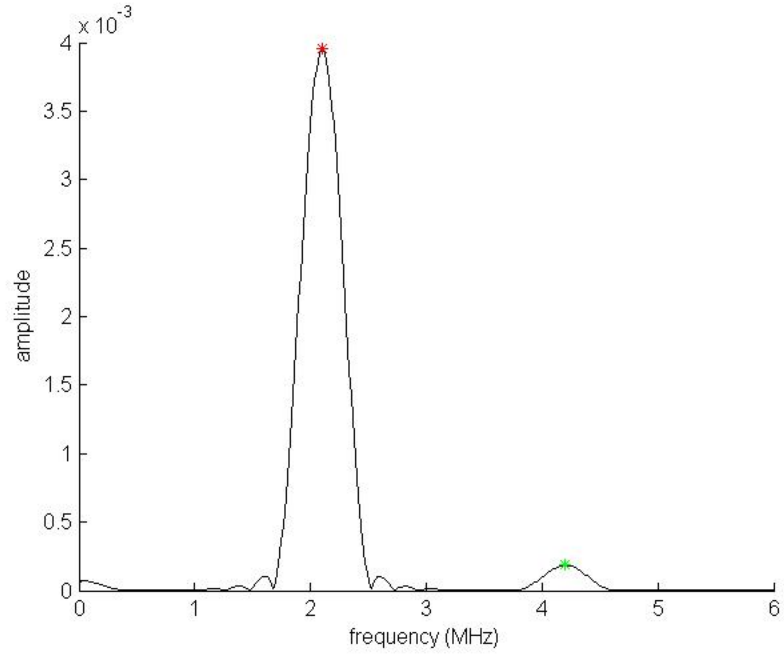


Figure 21. Sample frequency domain plot for Rayleigh wave measurements

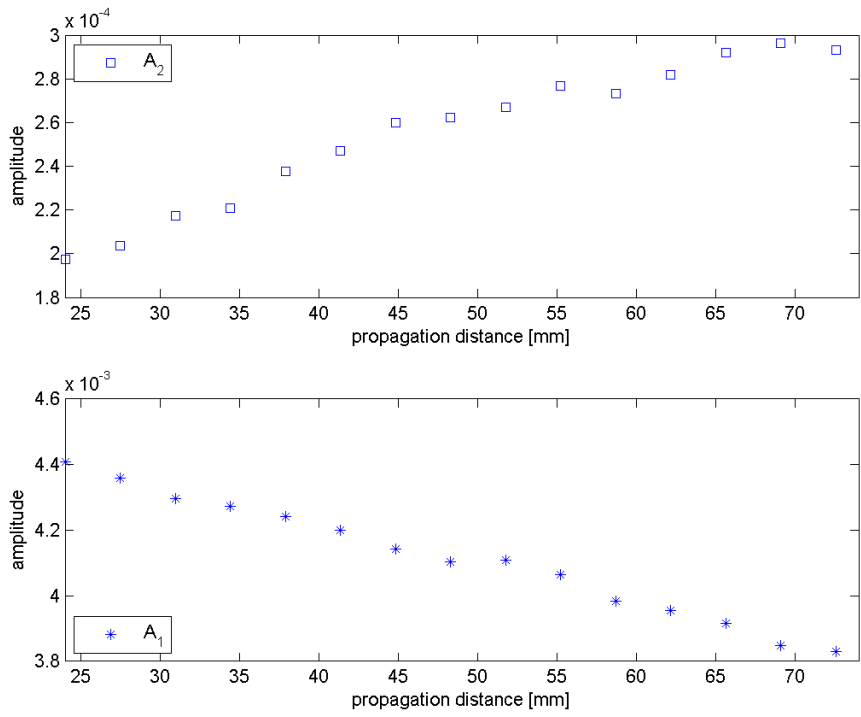


Figure 22. Rayleigh wave, A_1 and A_2 as a function of propagation distance

These extracted values for A_1 and A_2 are then used to calculate A_2/A_1^2 for each propagation point and then plotted as a function of propagation distance. A sample plot can be seen in Figure 23. A linear line is fit to this plot, and the slope of this line is the acoustical nonlinearity parameter β .

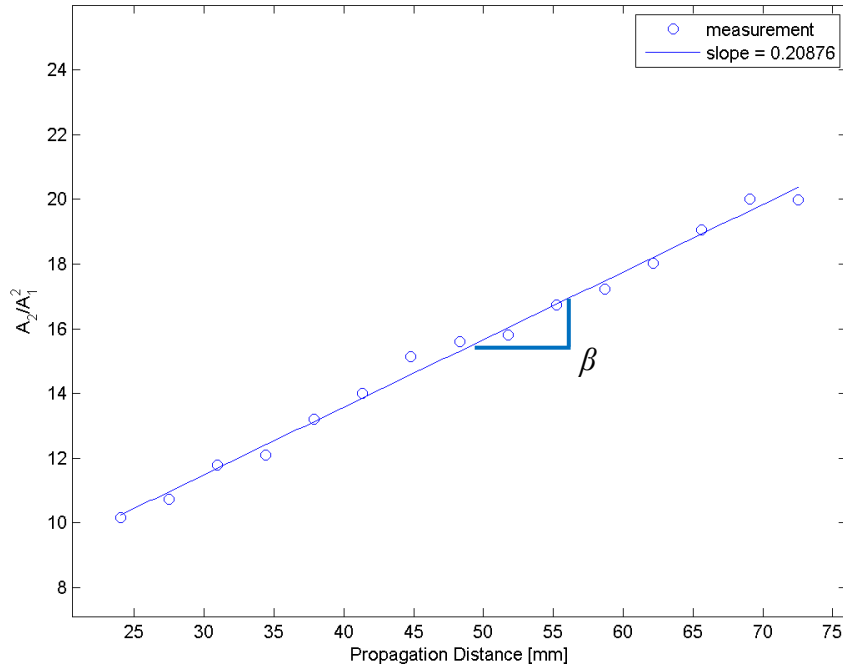


Figure 23. Rayleigh wave determination of β

4.2.2 Longitudinal Wave Measurements

The longitudinal NLU setup used in this research follows the same procedure that has been used in previous research studies [4,6]. Figure 24 shows the instrumentation used in the experimental setup. The experimental procedure consisted of the generation of a sinusoidal tone burst, which was amplified by a gated-amplifier (RITEC GA-2500A) and transmitted using a contact transducer. The signal traveled through the thickness of the specimen, interacted with the material, and then was detected with a second contact

transducer whose center frequency was twice that of transmitting transducer. This difference in center frequency between the transmitting and receiving transducers allows for better detection of the small amplitude second harmonic. The received signal was then saved by an oscilloscope for post-processing. Signal averaging (512 averages) was performed to increase SNR. An example of the received signal with windowing points can be seen in Figure 25. The input amplitude was then increased, and the procedure was repeated until the final input amplitude had been reached.

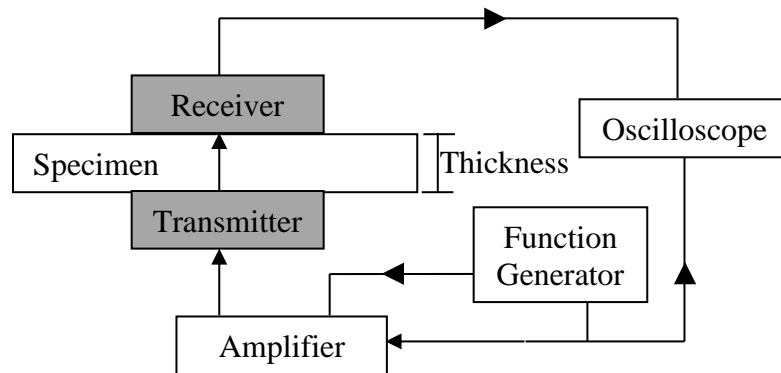


Figure 24. Longitudinal Experimental Schematic

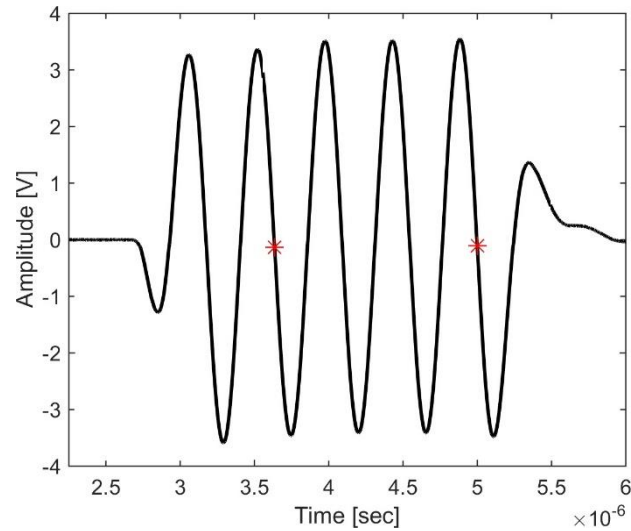


Figure 25. Raw signal with windowing points

A thin layer of oil coupling was spread between the contact transducers and the specimen to allow for better transmission of the acoustic energy between the transducers and the material. Additionally, extra care was taken to ensure that the centerlines of the transmitting and receiving transducers were aligned as well as consistent pressure was applied when affixing the transducers to the material.

The signal was received from the receiving transducer on an oscilloscope and saved for post-processing. After the signal was saved, the input amplitude was increased, and the measurement was performed again. The input amplitude was increased linearly until the final amplitude was reached.

The received signals were then processed extracting the amplitude of the first and second harmonic wave, A_1 and A_2 . Depending on the thickness of the material, the use of the FFT to extract A_1 and A_2 may not be possible as will be discussed in CHAPTER 5. In some cases other signal processing techniques may be used, such as the least squares

method, and will be discussed in full detail in CHAPTER 5. Once A_1 and A_2 have been determined for each of the received signals, A_2 is plotted as a function of A_1^2 as seen in Figure 26 where the slope of the fit line is proportional to the acoustic nonlinearity parameter, β .

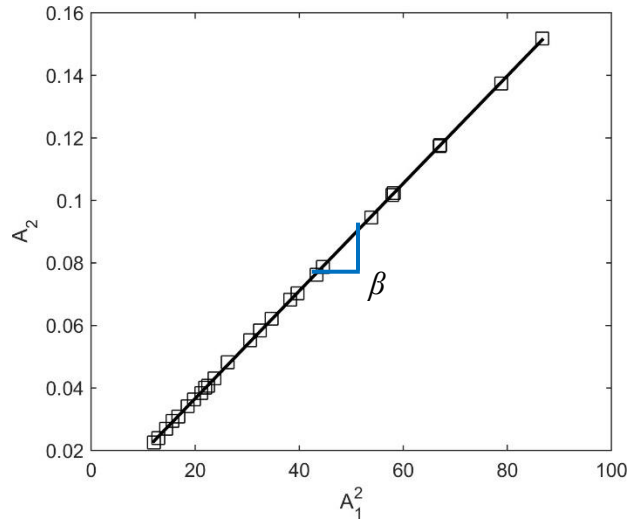


Figure 26. A_2 versus A_1^2 where the slope is β

4.3 NRUS Measurements

For the NRUS measurements, a completely noncontact setup is implemented, and the experimental schematic can be seen in Figure 27. The experimental procedure used for the NRUS measurements follows that established in [18]. In this setup, a function generator, controlled by Labview, generates a frequency sweep at a minimal amplitude which is then amplified by E&I RF power amplifier and transmitted to an air-coupled transducer (center frequency: 50 kHz). The acoustic waves are then focused using an acoustic horn designed by Steffen et al. [18] which follows the acoustic horns from Kim [76] which are based on the Webster horn equation. The focused acoustic waves then vibrate longitudinal waves in a free hanging specimen. The velocity of the opposite end

of the specimen is then measured using a laser vibrometer. The signal from the laser vibrometer is then sent to the computer for post-processing. The input amplitude is then increased, and the measurement is taken again.

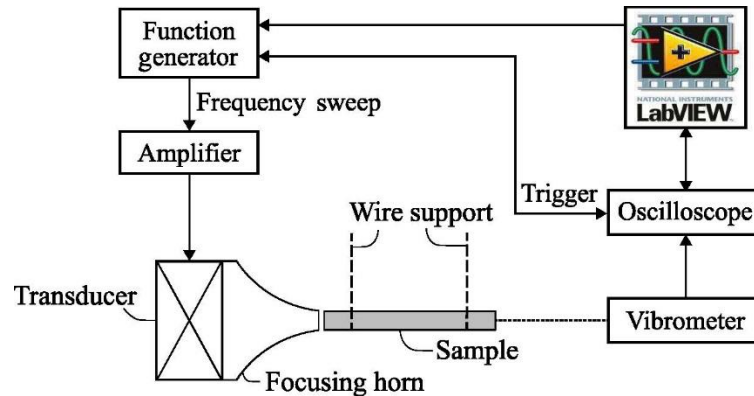


Figure 27. NRUS experimental setup

4.3.1 *Determination of resonance frequency*

The longitudinal modal resonance frequencies of the samples were determined analytically and confirmed experimentally.

4.3.1.1 Experimental determination of resonance frequency

The resonance frequency was determined experimentally through long frequency sweeps using the same setup seen in Figure 27. This setup allows the measurement of the longitudinal vibration modes and corresponding resonance frequencies. By taking the FFT of the time domain signals, one can easily see the eigenmodes as the peaks on the graph as seen in Figure 28.

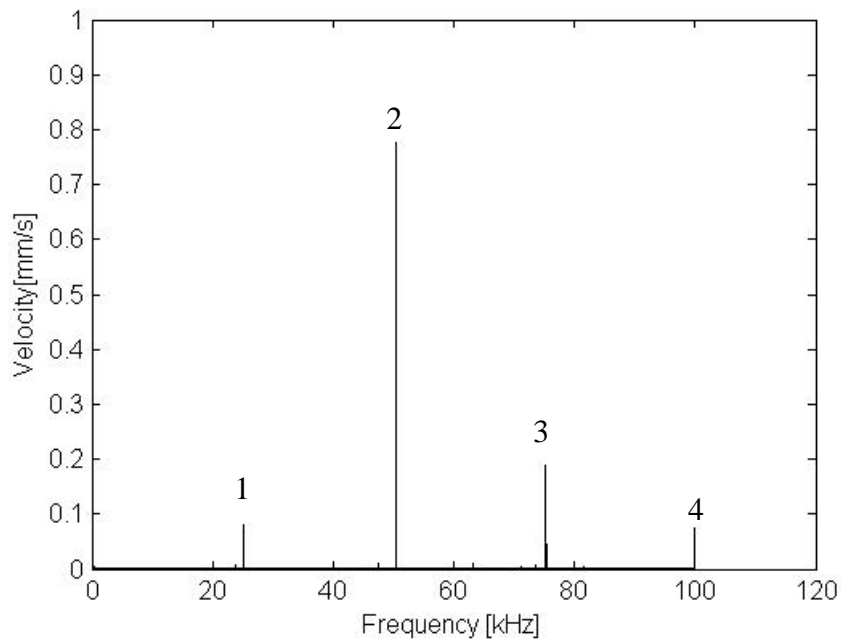


Figure 28. Experimental longitudinal vibration modes

4.3.2 *Post-processing for NRUS*

The resonance frequency at each drive amplitude was determined by applying a tapered cosine window to the time domain signal and then taking the FFT. Each time domain signal contains all of the information for the respective frequency sweep as seen in Figure 29. The frequency curves for each of the drive amplitudes were all plotted on a single plot to observe the frequency shift as seen in Figure 30, and the peak of each frequency curve being the resonance frequency for the respective drive amplitude.

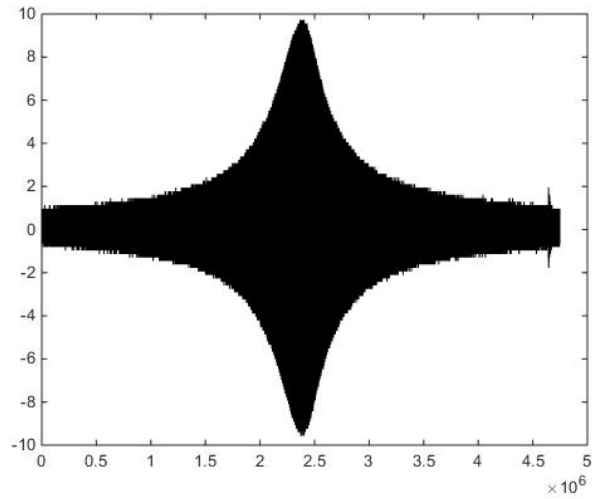


Figure 29. Time domain signal example for NRUS measurement

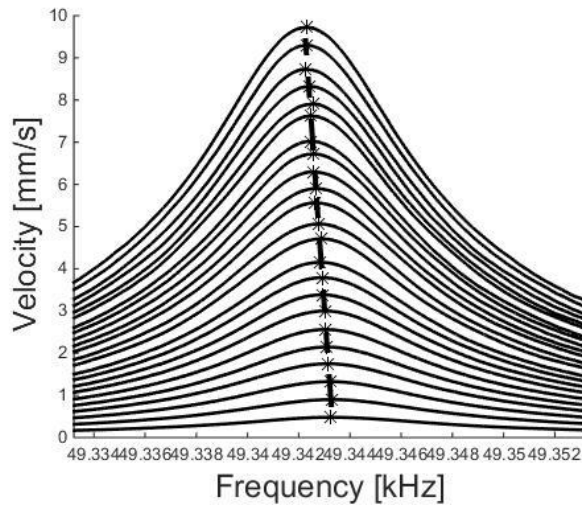


Figure 30. Resonance frequency spectrum curves example (same as Figure 5)

The equilibrium resonance frequency (linear resonance frequency), f_0 , was determined by fitting a line to the resonance curves, Figure 30, and finding the intersection of the linear fit with the x-axis. The strain amplitude for each drive amplitude can then be calculated using Eq. 101 from Section 2.4.1.2. The inputs to the equation are

determined as follows: v_n is the velocity amplitude measured using the laser vibrometer (measured voltage is multiplied by LDV sensitivity), L is the length of the specimen, and f_n is the resonance frequency determined from the resonance frequency curves. The relative frequency shift, $\Delta f/f_0$ ($\Delta f = f - f_0$), is then plotted as a function of the strain amplitude for each drive amplitude as seen in Figure 31 and fit with a linear fit. The hysteretic nonlinearity parameter, α_f , is then determined to be the slope of this fit line as seen in the figure.

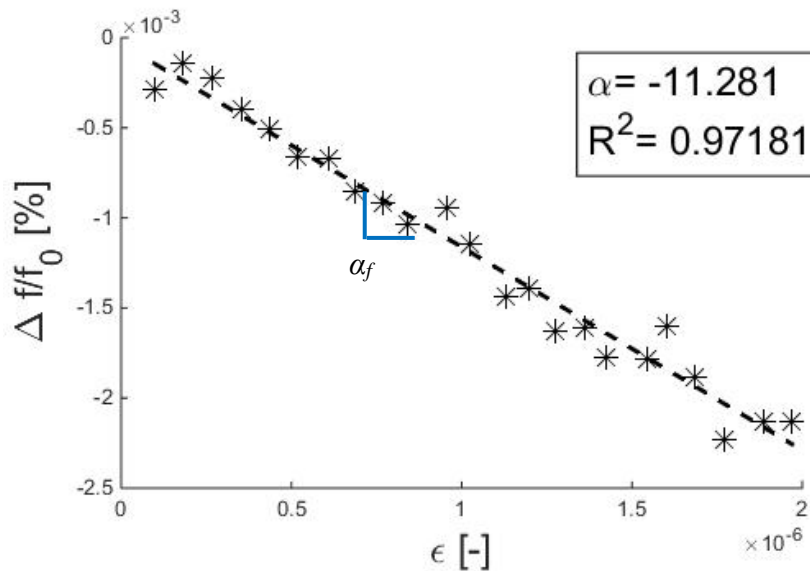


Figure 31. Relative frequency shift as a function of strain amplitude to determine α_f

CHAPTER 5. SIGNAL PROCESSING FOR THIN SPECIMENS

5.1 Overview

In some applications, it is desirable or even necessary to investigate specimens that are considered “thin”. For example, it may be of interest to study a specimen that has the same “thin” characteristic that is seen *in-situ*. However, because of finite thickness, the number of cycles in the propagating wave is limited and has been a hindrance to thin specimen measurement in the past.

In finite thickness specimens, it is critical to avoid the interference between the forward propagating and boundary-reflected tone-burst signals. The reason for this is that “extraneous” higher harmonic waves are produced in the reflection mode at a stress-free boundary [77]. Thus the maximum number of cycles is limited for the tone-burst wave packet to “fit” within twice the thickness of the specimen. The maximum number of cycles, n , is:

$$n = \frac{2h}{\lambda} \quad (109)$$

where h is the specimen thickness, and λ is the wavelength of the fundamental wave.

The conventional and most preferred signal processing method used to extract the amplitudes of the fundamental and second harmonic waves from the tone-burst signal is the Fourier analysis using a discrete Fourier transform (DFT) [78]. However, this method fails for tone-burst signals with a low number of cycles; in this case, the main lobe (for

the fundamental) is wide and its side-lobes interfere with the intrinsically small second harmonic component, ultimately leading to the calculation of an incorrect nonlinearity parameter, β . This section is motivated by this shortcoming of the DFT, with the objective of determining alternative signal processing methods, which perform better in thin specimens. This section examines five available signal processing methods: DFT; original Prony method; least squares (LS) Prony method; known poles (KP) Prony method; and a direct fitting least squares method. With such a wide range of signal processing methods available, it is unrealistic to consider all of these candidate methods in a single study. Therefore, these five methods were chosen because of their similarity to the DFT, their ease of understanding and implementation by the reader, and their use in other ultrasonic research [79–83]. Additionally, the Prony methods are relatively easy to implement compared to other available methods and have the capability to fit not only damped signals but also undamped signals. In the latter case, the damping parameter is set to be a near zero value by the algorithm. The Prony method and its variations have been used in a variety of previous acoustic and ultrasonic research for both transient and short steady state signals [79–83].

Through both numerically generated synthetic signals and experimental measurements, this research investigates the accuracy and feasibility of the five candidate signal processing methods to accurately calculate the amplitude of the fundamental and second harmonic waves, and then subsequently β . The numerical simulations provide the ability to control attributes of the tone-burst signal and determine the effectiveness of each of the five methods, while the experimental measurements provide additional insight

into each method and feasibility for the implementation. A description of the numerical simulation and experimental procedure can be found later on in this section.

5.2 Method Background

The following section will give a description and derivation of the five available signal processing methods investigated in this section.

5.2.1 Discrete Fourier Transform

This research implements the fast Fourier transform (FFT) which is an efficient way to calculate the DFT and makes use of Matlab's *fft* command. More information on the DFT can be seen in Appendix A.

5.2.2 Prony Method

A full derivation of Prony's method can be found in Appendix A including information for the least squares and known poles modifications. Prony's method is a signal modeling method where a linear combination of exponentials is fit to a set of data points [84]. For the NLU measurements described in this paper, the linear combination of exponentials represents the summation of sinusoidal signals (fundamental and higher harmonic frequencies) which make up the received signal. Fitting this linear combination to the received data allows for the computation of frequencies that make up the signal along with their corresponding amplitude, phase angle, and damping factor. This section gives a brief description of the steps found in Prony's method. Future sections will provide the solution for either the original Prony method or one of the modifications (least squares or known poles) and the full derivation can be seen in Appendix A.

In general, Prony's method can be thought of comprising three steps. The first step consists of developing a model that fits p exponentials to the data (finite sample with N discrete data points) and determining the corresponding parameters. These parameters can then be used to develop a polynomial in the second step, and the roots of this polynomial are determined. These roots can then be used to determine the frequencies of the signal and the corresponding damping factors. The corresponding amplitudes and phase angles can then be determined in the third step from these values.

The Prony prediction model for the SHG measurements can be seen in Eq. 110 where A_k is the amplitude, α_k is the damping, f_k is the frequency, θ_k is the phase angle, and T is the sampling interval in seconds (1/sampling frequency):

$$\hat{x}[n] = \sum_{k=1}^p A_k e^{(\alpha_k + j2\pi f_k)(n-1)T + j\theta_k} = \sum_{k=1}^p h_k z_k^{n-1} \quad 1 \leq n \leq p \quad (110)$$

Note that Eq. 110 is simplified by the substitution of h_k in for $A_k e^{j\theta_k}$ and z_k in for $e^{(\alpha_k + j2\pi f_k)T}$. By following the in-depth derivation seen in Appendix A, the values for the frequency, the damping, the amplitude, and the phase angle can be calculated using the following equations.

$$f_k = \frac{\tan^{-1}\left(\frac{\text{Im}\{z_k\}}{\text{Re}\{z_k\}}\right)}{2\pi T} \quad [\text{Hertz}] \quad (111)$$

$$\alpha_k = \frac{\ln|z_k|}{T} \quad [\text{seconds}^{-1}] \quad (112)$$

$$A_k = |h_k| \quad (113)$$

$$\theta_k = \tan^{-1} \left(\frac{\text{Im}\{h_k\}}{\text{Re}\{h_k\}} \right) \quad [\text{radians}] \quad (114)$$

5.2.2.1 Least Squares Prony Method

Modifications have since been made to the original Prony method to adapt to varying conditions. The LS Prony method was developed to be used when the number of data points exceeds the number of data points needed to fit the model to the data (overdetermined) [84]. This method is not an exact fit to the data as was used in the original Prony method. Instead, it minimizes the squared error through the determination of the parameters z_k and h_k . An in-depth discussion for the math behind the LS Prony method can be seen in Appendix A.

5.2.2.2 Known Poles Prony Method

Often times some of the frequencies are known a priori, but their amplitudes may be unknown [79] as is the case for SHG. The known poles (KP) Prony method can be used in this instance. An in-depth discussion on the math behind the KP Prony method can be seen in Appendix A.

5.2.3 *Least Squares Method*

This method makes a least squares fit between the measured data points and a proposed model. In SHG, it is known that the measured signal is composed of two sinusoidal waves: the fundamental wave whose frequency is the same as the input

frequency, f_1 , and the second harmonic wave whose frequency is twice that of the fundamental wave, $f_2=2*f_1$. The model for the signal adds both wave components together:

$$s = b_1 \cos(2\pi f_1 t) + b_2 \sin(2\pi f_1 t) + b_3 \cos(2\pi f_2 t) + b_4 \sin(2\pi f_2 t) + b_5 \quad (115)$$

The model adds a cosine component and a sine component for each frequency to account for any phase differences as well as a constant, b_5 , to account for any vertical shift in the signal.

Eq. 115 is rewritten in the following matrix form where the elements of the s -vector are the measured data points:

$$\begin{bmatrix} s[1] \\ s[2] \\ \vdots \\ s[N] \end{bmatrix} = \begin{bmatrix} b_1 \\ b_2 \\ b_3 \\ b_4 \\ b_5 \end{bmatrix} [\cos(2\pi f_1 t) \quad \sin(2\pi f_1 t) \quad \cos(2\pi f_2 t) \quad \sin(2\pi f_2 t) \quad 1] \quad (116)$$

Least squares is then used to calculate the b -coefficients. This can be done in Matlab using the *mldivide* command. The amplitudes of the fundamental and second harmonic waves are calculated using these b -coefficients as follows:

$$A_1 = \sqrt{b_1^2 + b_2^2} \quad (117)$$

$$A_2 = \sqrt{b_3^2 + b_4^2} \quad (118)$$

5.3 Numerical Simulation and Experimental Procedure

5.3.1 Numerical Simulation

A synthetic sinusoidal signal with two frequency components, fundamental frequency f_1 and second harmonic frequency f_2 , with added noise was created using MATLAB as:

$$sig = A_1 \sin(2\pi f_1 t) + A_2 \sin(2\pi f_2 t) + noise \quad (119)$$

where A_1 is the amplitude of the fundamental frequency component, and A_2 the amplitude of the second harmonic component. The amplitudes of the fundamental and second harmonic frequencies were selected as values close to typical experimental values, and the noise was generated using the *randn* command in MATLAB. Individual tone-burst signals were produced with cycle lengths varying from four to twelve cycles. The sampling frequency was set to 250 MSamples/sec to match that in the experiment. The individual tone-burst signals were averaged 512 times, mimicking the signal averaging used in the experiments.

To determine the effect of noise on the candidate signal processing methods, varying levels of noise were added to each of the numerically generated synthetic signals to obtain specific signal to noise ratio (SNR) values. The same range of noise was added to each of the individual tone-burst signals with varying lengths (four to twelve cycles). Each of the synthetic signals was then processed using the five signal processing methods to determine the amplitudes of the fundamental (A_1) and second harmonic (A_2) waves. The nonlinearity parameter, β was then calculated for each of the signals.

5.3.2 *Experimental Procedure*

The experimental measurements used the same longitudinal NLU setup described in Section 4.2.2. The generation frequency used in this experiment was 2.25 MHz. To enable a direct comparison of the five different signal processing methods, a relatively thick (~12.5 mm) 304L stainless steel specimen was used which allowed a maximum of 9 cycles to be generated in its thickness. The number of cycles in the tone-burst signal generated could then be reduced, simulating the wave packets needed in thinner specimens, thus providing the ability to "vary" the specimen thickness without changing any other conditions, like contact conditions between the specimen and transducers. The input amplitude was set for each measurement, and the number of cycles was increased in increments of one, from four to nine cycles.

5.3.3 *Post-Processing*

The numerically generated synthetic and experimental signals were each processed using the five candidate signal processing methods to extract the amplitudes of the fundamental, A_1 , and second harmonic waves, A_2 , at each input amplitude for each of the number of cycles. For the numerically generated synthetic signal, the nonlinearity parameter, β , was calculated directly using Eq. 9 as described in Section 2.2.1.1.

5.4 **Results and Discussion**

The results from the numerical simulation and experiments provide insights into the feasibility and accuracy of each of the candidate signal processing methods. The numerically generated synthetic signals allow control and a priori knowledge of the

specific signal attributes (such as amplitudes), while the experimental signals confirm the applicability to real measurement applications. The input amplitudes for the synthetic signal were chosen to be 6 and 0.06 for the fundamental and second harmonic waves, respectively. These amplitudes were selected to be close to the experimental values. These specific amplitudes resulted in a relative β value of 0.00167.

In the experimental measurements, it is crucial to only process the steady state portion of the tone-burst signal. For the specific generation transducer used in these measurements, the first two cycles and last cycle were determined to be transient, leaving the remaining steady state cycles to be processed; the remaining steady state cycles will be referred to as the effective number of cycles. The steady state cycles were chosen to be the cycles where the peak-to-peak amplitude remained steady as a function of time. Note that a Hann window was used in the DFT processing. To simulate experimental conditions, the numerically generated synthetic signals were generated with a specific number of cycles while only the effective number of cycles (number of cycles generated - 3) were processed.

5.4.1 Effect of SNR on the Synthetic Signals

In different experimental conditions, the noise level in the system can be inherently higher or lower depending, on measurement conditions. For example, if the material has large grain noise, the noise of the system would be higher. Consequently, the first signal attribute investigated in the numerically generated synthetic signals was the effect of noise on each of the five signal processing methods. The noise level in the system was determined by calculating the SNR of the second harmonic amplitude because it is a

naturally smaller amplitude, so it is affected more by noise than the amplitude of the fundamental wave. Results for the effect of SNR are shown in Figure 32. The dashed line in the figure represents the actual relative β value and the solid lines represent $\pm 5\%$ of this value. It is important to note the results from the DFT are so poor in Figure 32(a-b) that the results cannot be seen on the selected axes.

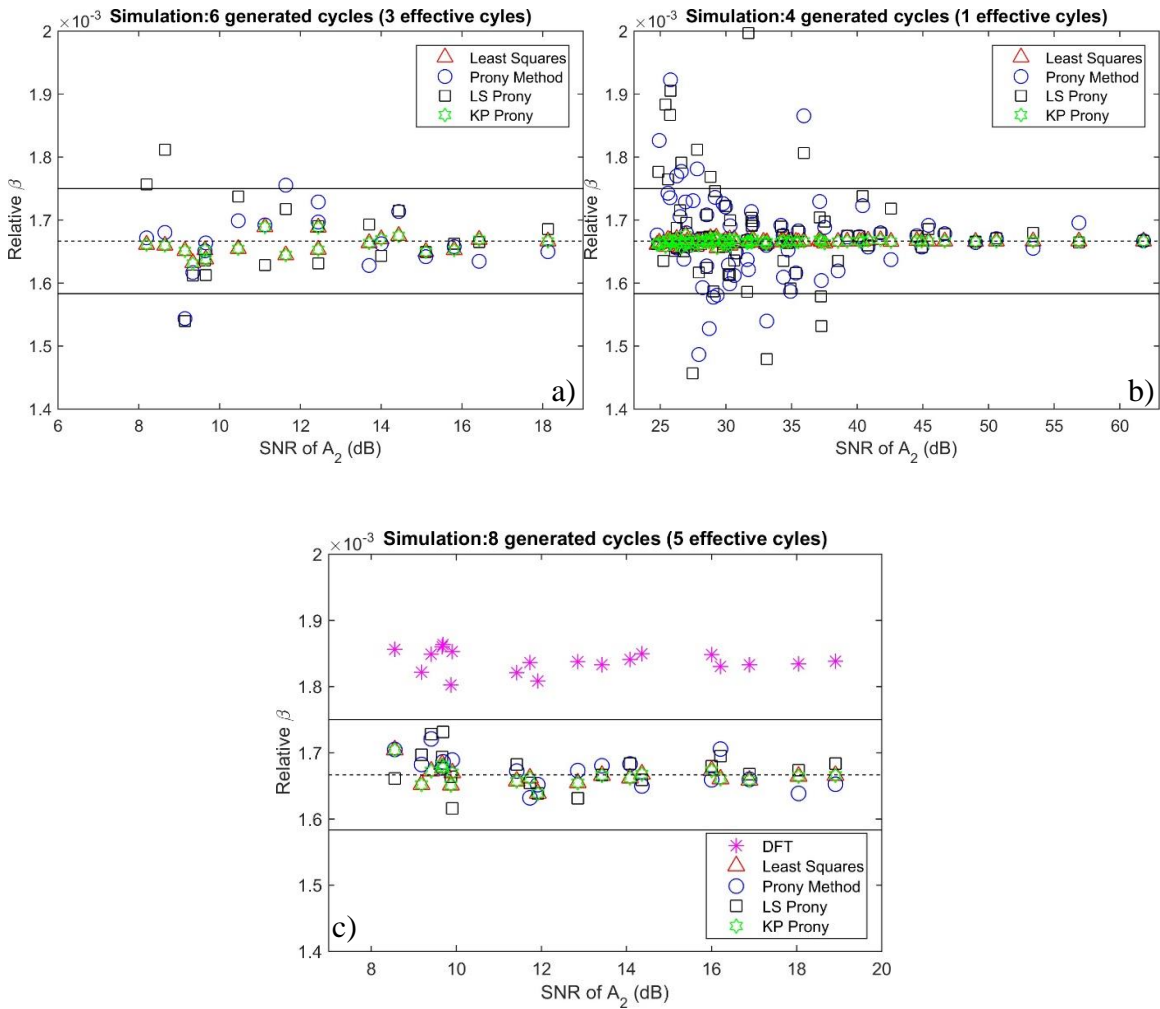


Figure 32. Effect of SNR of A_2 on calculation of relative β for a) three effective cycles b) one effective cycle c) five effective cycles [86]

Figure 32(a) shows the result for three effective cycles. The figure shows that the original Prony method and the LS Prony method are most influenced by the presence of

noise in comparison to the least squares and KP Prony method. Specifically, this figure shows that the original and LS Prony methods accurately calculate relative β within $\pm 5\%$ when the SNR is above 13 dB. Figure 32(b) illustrates how drastically the SNR could affect the accuracy of the original and LS Prony methods. As the SNR increases, the accuracy of both the original and LS Prony methods increases, and the calculated relative β value converges to the known value of 0.00167. Note that the calculated values of β with the DFT do not even fit within the range of Figure 32(a-b). Figure 32(c) shows that while the accuracy of the DFT greatly improves with increasing SNR, the change in SNR has a smaller effect on the accuracy of the DFT in comparison to the other signal processing methods. Most importantly, this figure demonstrates the issues with simply using the DFT for a tone-burst signal with a low number of cycles – the DFT does not even calculate a value of β within 5% of the known value.

Table 2 provides a summary of the minimum SNR of A_2 required to use either the original or LS Prony methods to accurately calculate β within 5% for one to eight effective cycles. These minimum SNR values were determined from plots similar to those seen in Figure 32(a-c) where the results from the original and LS Prony methods approached the actual relative β value, and there was little scatter in the result points. Note that these are an approximation and care should be taken when making measurements where the SNR is close to these values.

Table 2. Minimum SNR of A_2 to accurately determine β within $\pm 5\%$ for original/ LS Prony methods for varying number of effective cycles

Number of Effective Cycles	SNR (dB)
1	40
2	16
3	13
4	11
5	10
6	10
7	10
8	10

5.4.2 Comparison of Five Candidate Signal Processing Methods

Now consider the experimentally measured tone-burst signals, where the SNR of A_2 for this setup was calculated to be approximately 13 dB. For ease of comparison, the SNR of A_2 for the numerically generated synthetic signals was chosen to be a similar value of 13.2 dB which is within 2% of the experimental value. In addition, the range of effective cycles was chosen from one to six, as the maximum number of cycles for this 12.5 mm thick 304L stainless steel specimen is nine per Eq. 109. The results for the experimental measurements and numerical simulation (synthetic signals) are shown in Figure 33(a) and Figure 33(b), respectively.

Note that the difference in the value of β between the experimental measurements (~ 0.00176) and the numerical simulation (0.00167) is a product of the procedure and not the signal processing methods. For the numerically generated synthetic signals, β is calculated directly from the values of A_1 and A_2 , but for the experimental measurements, β is calculated from the measurement of several input voltages resulting in the difference of β between the two. While it is desirable to have similar values of β to help with

analysis, it is not necessary for them to be the exact same value between the experimental measurements and the numerical simulation when comparing the signal processing methods. Instead, it is desirable to have similar SNR of A_2 because of its effect on the signal processing methods.

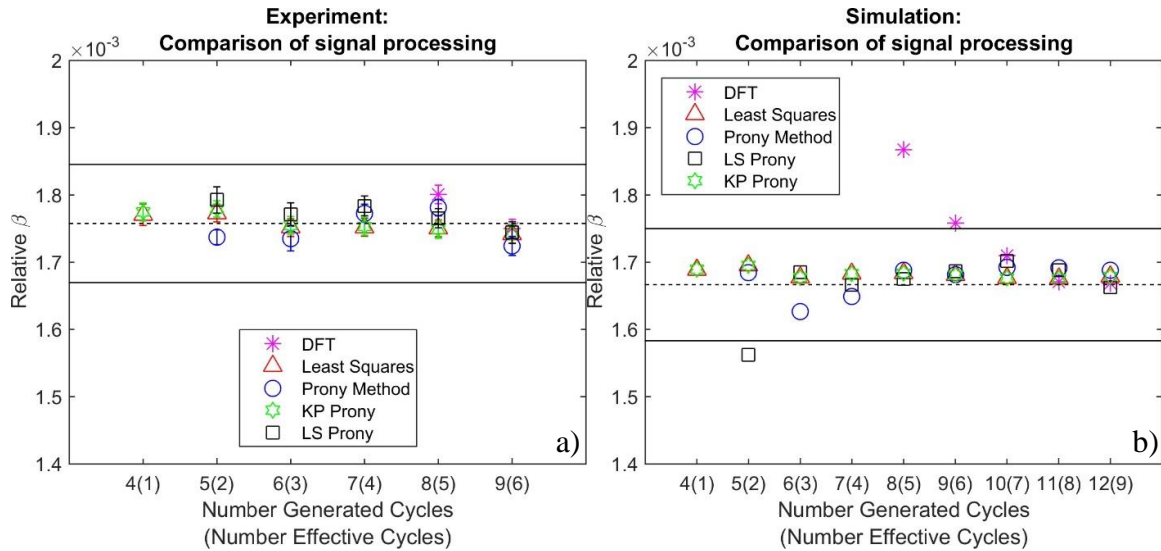


Figure 33. Comparison of signal processing methods for varying number of cycles, a) experimental, b) numerical simulation (synthetic signals) [Note: For less than eight generated cycles, DFT values are so poor that they are off the scale.] [86]

The results presented in Figure 33 demonstrate the limitations of the signal processing techniques as well as provide a basis for selecting the most appropriate signal processing techniques to use when measuring thin specimens with SHG. The next few paragraphs will discuss the results for each of the signal processing techniques at length, and the conclusions on the best methods for thin specimens will be described at the end.

Despite the ease of implementation and low amount of computational power needed for the DFT, the results for both the synthetic and experimental signals demonstrate the shortcomings of the DFT for the low number of cycles possible in thin specimens. These

results demonstrate the well-known fact that as a signal length shortens in the time domain, the spectrum broadens in the frequency domain (the principle of uncertainty). This intrinsic behavior causes the side lobes of the fundamental frequency to interfere with the amplitude of the second harmonic. This interference effect is seen in the results for the low number of effective cycles. While the DFT is effective in measuring the value of A_1 even for a low number of effective cycles, the value of A_2 increases as the number of effective cycles decreases because of the increasing interference from the fundamental frequency. This interference is present until there are at least eight effective cycles, as seen in the numerical simulation results, rendering the DFT ineffective for SHG measurements when the number of effective cycles cannot be increased to at least eight cycles.

In contrast, the original and LS Prony methods provide an accurate method for extracting the values of A_1 and A_2 for a low number of effective cycles as long as the SNR of A_2 is large using the criteria described earlier. Unfortunately, this dependence on the SNR of A_2 is a major drawback of these two methods. As the level of noise increases, the tone-burst signal length (number of effective cycles) must increase to retain the accuracy of both of these methods as seen in Table 2. It is known that the Prony method does not perform well in the presence of noise [84,87–89]. One way to compensate for the noise is to over define the system by increasing the number of unknown parameters [84,90,91]. However, the number of unknown parameters is limited to half the number of data points. To achieve a system where there are enough unknown parameters, the length of the signal (number of effective cycles) must be a minimum length – as the noise level rises, the minimum number of effective cycles also increases. For this reason, the noise

level in this system causes both the original and LS Prony methods to inaccurately determine the values of A_1 and A_2 if there is only one or two effective cycles.

Fortunately, the least squares and the KP Prony methods provide an accurate method for extracting the values of A_1 and A_2 for all signal lengths, and the presence of some noise ($\text{SNR} > 3\text{dB}$) seems to have a minimal effect. The accuracy of these results is expected because these methods take advantage of available information of the frequency contents in the acquired tone- burst signal and apply this directly in the model equations. This requirement of known frequency contents can be a shortcoming of these two methods when there is a slight shift in the true generated frequency due to slight flaws in equipment. However, it is not difficult to determine the fundamental frequency of a tone-burst signal in general. As a result, the least squares and the KP Prony methods are the two best methods for the application of SHG in thin specimens.

The four available signal processing methods have proven to be good alternatives to the DFT when testing thin specimens using SHG (less than 8 effective cycles). The least squares and KP Prony methods outperform the other three candidate methods, regardless of the number of effective cycles when the frequency contents are known a priori. The original and LS Prony methods provide accurate means to calculate β if the SNR of A_2 is sufficiently large. However, all three Prony methods have a greater implementation and computational complexity than the least squares method and the DFT. With these limitations and abilities in mind, it is determined that the best methods for the extraction of A_1 and A_2 when analyzing thin specimens are the least squares and KP Prony methods.

Note that another potential application of these results is cases when the attenuation of a material due to features like large grains can be very large, making it impractical to conduct ultrasonic measurements on a thick specimen or at a high frequency.

5.5 Application for Fe-1.0% Cu specimens

The least squares and the KP Prony methods are now used in an application to analyse experimental data for a set of Fe-1.0% Cu specimens which had been heat treated for varying lengths of time (untreated, 5 h, 15 h, 30 h, 100 h, and 300 h) as described in Section 3.4. These specimens were previously analyzed using the original Prony method, and previous results can be found in [6,92].

Following the procedure in [6,92], both the least squares and KP Prony methods are used to calculate the relative nonlinearity parameter, β , for each of the heat treatment times and normalized using the 5-h specimen. Figure 34 shows the results for normalized relative β using these two signal processing techniques as well as a comparison to the results found in [6,92]. First, the β values obtained from the least squares and KP Prony methods are almost exactly the same for all heat treatment times making it difficult to distinguish between the two results on the figure. These β values show an initial decrease from the untreated to the 5-h specimen possibly due to the initial nucleation of Cu-precipitates, followed by an increase in β from the 5-h specimen to the 30-h specimen due to the growth of the Cu-precipitates. There is a continued increase in β from the 30-h specimen to the 100-h specimen due to either some of the Cu-precipitates remaining coherent with the Fe-matrix or some of the pinned dislocations becoming unpinned

leading to an effectively longer loop length. Finally, β decreases from the 100-h specimen to the 300-h specimen which is attributed to a loss of coherency between the Cu-precipitates and the Fe-matrix. The specifics on these changes in β will be discussed in more detail in the results and discussion sections.

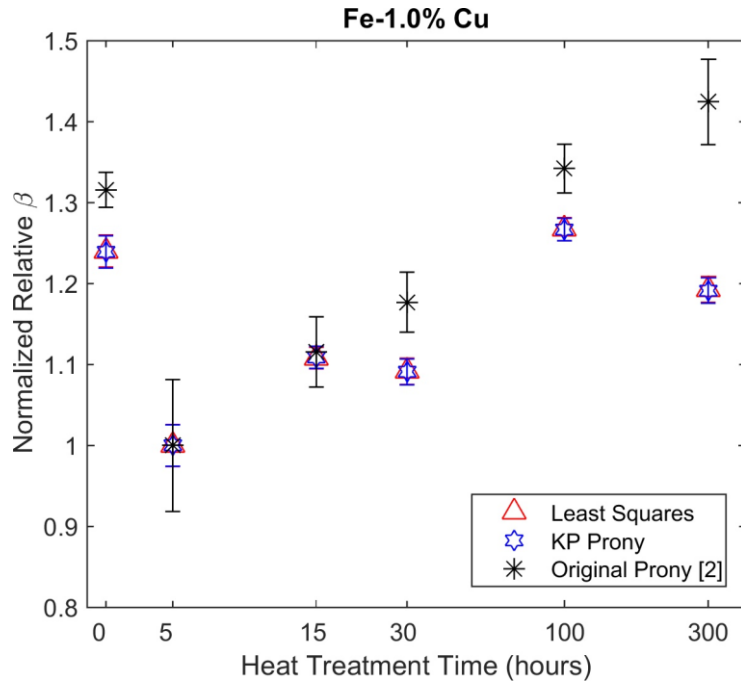


Figure 34. Normalized relative β for Fe-1.0% Cu specimens using least squares method, KP Prony method, and original Prony method [6,86]

These results from the least squares and KP Prony methods are not too far from the results in [6,92] except for the decrease in β from the 100-h to 300-h specimen. The discrepancies between the results can be explained by two reasons. First, the results of the present study demonstrate the large effect noise can have on the original Prony method, even when the SNR seems to be a reasonable value (~ 10 dB for A_2 for the Fe-1.0% Cu specimens). Since the SNR is on the cusp between the original Prony method being a reliable method and not being a reliable method, the results given by the original Prony

method might not be as consistent as originally thought. The second reason is that the results of the current study demonstrate the importance of only analyzing the steady state portion of the signal, which may not be intuitive when looking at an experimentally measured tone-burst signal. [6,92] analyses four cycles of the signal, where one of the cycles is in the transient portion of the signal, while the least square and KP Prony results of Figure 34 only analyze the last 3 cycles in the signal which is in the steady state portion. It is believed that the present trend in β is more representative of the actual changes in the microstructure than the previous one in [6,92], in that the expected decrease after a certain time was not present in [6,92]. The present trend in β was also seen by another research group who modeled the Fe-Cu material [7].

CHAPTER 6. NLU RESULTS AND DISCUSSION

6.1 Overview

This research looks at both the sensitivity of NRUS and SHG to different microstructural mechanisms in metals and compares the NLU methods to a linear method. All of the measurements in this section are normalized to a specified base state so that the relative differences between specimens may be seen. The relative differences also allow for easier comparisons between the measurement types. In this chapter, the results for α , β , and ANOVA are presented for the 304 stainless steel, 316L stainless steel and Fe-1.0% Cu specimens. The error bars seen in each of the figures represent the standard error for experimental repeatability.

6.2 304 Stainless Steel

The first results that will be presented in this section are those from the 304 stainless steel. As presented in the materials section (3.2), an annealed sample (non-sensitized) is compared to a sensitized sample. This allows the comparison between a sample with minimum microstructural damage (annealed) and a sample with chromium carbides that have grown in and along the grain boundaries.

6.2.1 Specimen preparation

For the two nonlinear ultrasound techniques, the specimens had to be prepared at different sizes for each technique. Both sets of samples were cut using wire EDM to minimize the added stresses in the material. For the NRUS specimens, the samples were

cut to 10 mm x 10 mm x 100 mm. This size was chosen to retain consistency with Maier et al [18] who developed the noncontact NRUS technique used in this research. The length of the specimens is much longer than the width/height dimensions to ensure that the problem can be treated as 1D. The ends of the specimens are polished using sandpaper up to 2000 grit to provide a smooth surface as well as provide a reflective surface for the laser to measure. For the SHG measurements, the samples were 152.4 mm× 50.8 mm×12.7 mm. This size was chosen to allow the propagation of a Rayleigh wave across the surface of the material. These specimens were surface ground and polished using a polishing wheel to provide a clean and even surface for measurement.

6.2.2 NRUS Results

The noncontact NRUS measurements were conducted on these two specimens using the procedure outlined in section 4.3. For each specimen, the measurement was conducted 10 times for repeatability and accuracy of the measurement. The results for α for both the annealed and sensitized samples can be seen in Figure 35. The values for α have been normalized by the annealed specimen value. This allows easy comparison to the base state. As can be seen in the figure, there is an increase in α of approximately 43% between the annealed and sensitized samples. Note the strain levels for this set of measurements were on the order of 10^{-6} .

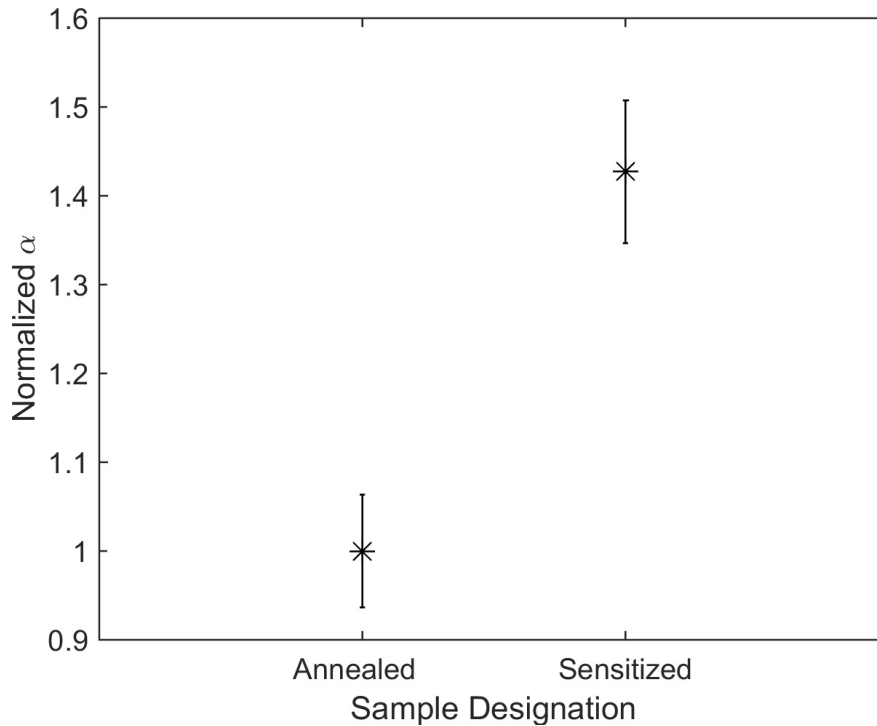


Figure 35. Measurements of α for 304 stainless steel comparing annealed and sensitized specimens where error bars represent the standard error for experimental repeatability

6.2.3 SHG Results

The SHG measurements using Rayleigh waves were made by Doerr et al [29] and can be seen in Figure 36. The results from Doerr et al show several more heat treatment steps than conducted for the NRUS measurements. This was to determine how heat treatment time affected sensitization. After annealing, Doerr et al heat treated the 304 stainless steel for varying lengths of time at 675°C to track the growth of the chromium carbides in the grain boundaries. Doerr et al then made SHG and DOS measurements on each of the specimens. As described in section 3.2.2, the DOS measurements provide a “ground truth” for the specimens. As can be seen in the figure, the DOS is fairly level from heat treatment times of 0 min to 120 min and then begins to increase as the chromium carbides

begin to form in the material and levels off to a second plateau. β follows a similar trend to the DOS where it remains level while the material is non-sensitized and then jumps to a second plateau when the chromium carbides begin to form. The increase in β between the annealed and sensitized samples is 25%.

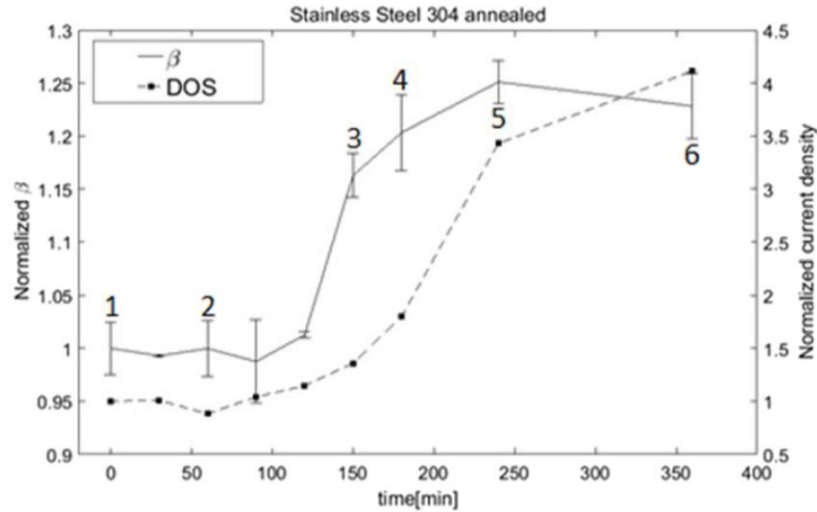


Figure 36. Measurements for β for 304 stainless steel comparing results of sensitization [29]

6.2.4 ANOVA Results

ANOVA was used to determine the statistical significance of the experimental results. Using the procedure setup in section 2.6, the ANOVA results for α can be seen in Table 3. It can be seen that the F-value is much larger than the F-critical value and the P-value is much lower than 0.05. These results show that the null hypothesis is rejected, and the mean values of α are significantly different. This significant difference means that the changes in α are due to changes in the microstructure and not due to random error.

Table 3. ANOVA results for α for 304 stainless steel

<i>Source of Variation</i>	<i>SS</i>	<i>df</i>	<i>MS</i>	<i>F</i>	<i>P-value</i>	<i>F crit</i>
Between Groups	302.22	1	302.22	10.61	0.0044	4.41
Within Groups	512.68	18	28.48			
Total	814.91	19				

6.3 316L Stainless Steel

This section looks at the effect that dislocations and residual stresses have on the nonlinear and linear parameters. This was done by looking at the 316L stainless steel samples. As discussed earlier, an as-received piece of 316L is compared to the heat treated piece of 316L. The as-received piece of 316L is cold-worked with the dislocations being due to this cold-working. This analysis investigates the effect that removing some of these dislocations and residual stresses has on α and β .

6.3.1 Specimen preparation

Similar to the 304 stainless steel specimens, the 316L specimens were cut using wire-EDM to sizes needed for the nonlinear measurements. For the NRUS measurements, the specimens were cut so that the length of the specimen was much longer than the width/height to retain the 1D problem. However due to size restrictions of the piece of 316L provided, these specimens were cut smaller than the 304 specimens, 5 mm x 5 mm x 50 mm. It was found that these specimens provided a better signal and slightly higher strain value so future specimens used for NRUS measurements were cut to this size. Please note that while this size improved the measurements, the improvement was not enough to warrant the recutting of the 304 specimens. These specimens were then

polished on their ends using sandpaper up to 2000 grit. The specimens for the SHG measurements were cut to the size 2 inches by 6 inches. This size allows for the propagation of a Rayleigh wave along the surface of the material. These specimens were then surface ground and sanded to provide a clean and even surface for measurements.

6.3.2 *NRUS Results*

NRUS measurements using the noncontact technique described in section 4.3 were made on the as-received and heat treated specimens. The values for α can be seen in Figure 37 where the error bars represent the standard error of 10 measurements. The values for α are normalized by the as-received α -value allowing a comparison between the base and heat treated state. The figure shows that α decreases from the as-received to the heat treated state by 44%. Note the strain levels for this set of measurements were on the order of 10^{-6} .

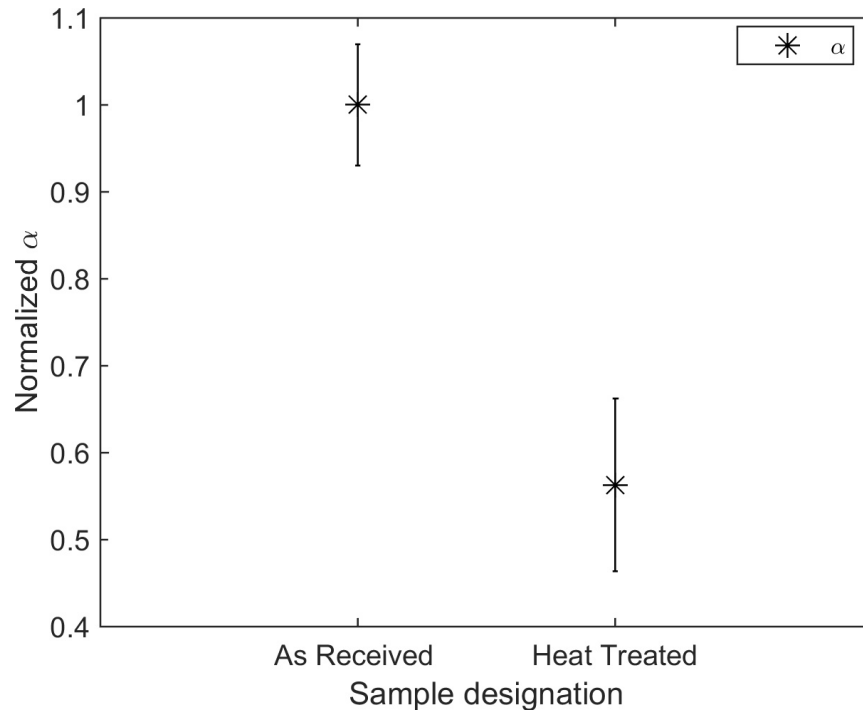


Figure 37. Measurements for α for 316L specimens comparing an as-received and heat treated specimen where error bars represent the standard error for experimental repeatability

6.3.3 SHG Results

The SHG technique used for these samples is Rayleigh waves using the experimental technique described in section 4.2.1. The results for β can be seen in Figure 38 where the error bars show the standard error of 4 measurements. The values for β are normalized by as-received value. The figure shows that β decreases from the as-received specimen to the heat treated specimen by 20%.

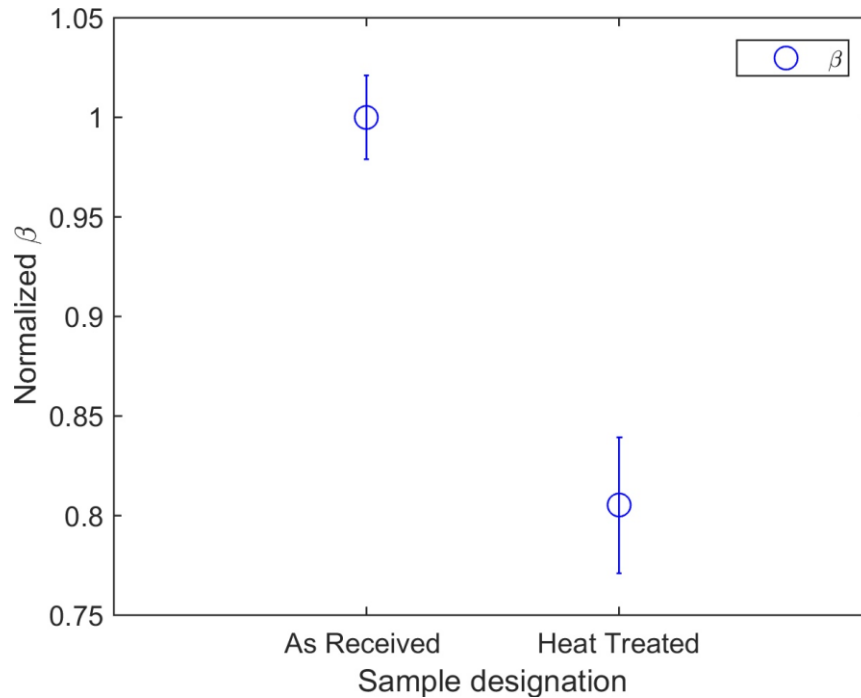


Figure 38. Measurements for β for 316L specimens comparing an as-received and heat treated specimens where error bars represent the standard error for experimental repeatability

6.3.4 ANOVA Results

ANOVA was used to determine the statistical significance of the experimental results. Using the procedure setup in section 2.6, the ANOVA results for α can be seen in Table 4, and the ANOVA results for β can be seen in Table 5. It can be seen that the F-value is much larger than the F-critical value and the P-value is much lower than 0.05. These results show that the null hypothesis is rejected, and the mean values of α and β are significantly different. This significant difference means that the changes in α and β are due to changes in the microstructure and not due to random error.

Table 4. ANOVA results for α for 316L stainless steel

<i>Source of Variation</i>	<i>SS</i>	<i>df</i>	<i>MS</i>	<i>F</i>	<i>P-value</i>	<i>F crit</i>
Between Groups	27.10	1	27.10	23.9	0.00012	4.41
Within Groups	20.41	18	1.13			
Total	47.52	19				

Table 5. ANOVA results for β for 316L stainless steel

<i>Source of Variation</i>	<i>SS</i>	<i>df</i>	<i>MS</i>	<i>F</i>	<i>P-value</i>	<i>F crit</i>
Between Groups	8.97E-06	1	8.97E-06	31.68	0.0013	5.99
Within Groups	1.7E-06	6	2.83E-07			
Total	1.07E-05	7				

6.4 Fe-1.0% Cu

This section looks at the results for the Fe-1.0% Cu specimens. As discussed in section 3.4, the heat treatment of Fe-Cu promotes the nucleation and growth of Cu-precipitates where increasing heat treatment time simulates increasing radiation damage. These Cu-precipitates are known to be the microstructural mechanism of precipitate-pinned dislocations. This section provides measurement results for both α and β as well as introduces a “stick” model for β .

6.4.1 Specimen preparation

Similar to the 304 stainless steel and 316L stainless steel, the Fe-Cu specimens were prepared for the NRUS and SHG measurements. Since these specimens were provided by KAERI, the initial size was limited to 9mm x 32 mm x 150 mm, and this was the size used for the SHG measurements where the only surface treatment was to surface grind and sand the material up to 1500 grit sandpaper. For the NRUS measurements, the

specimens were cut following the size used for the 316L specimens (5 mm x 5 mm x 50 mm) using wire-EDM. The surfaces were then sanded using up 2000 grit sandpaper.

6.4.2 *NRUS Results*

The noncontact NRUS setup was again used to measure α where the results can be seen in Figure 39 and the error bars represent the standard error of 10 measurements. The α values have been normalized by the heat treatment time of 5-hours. This normalization value was chosen because between 0-hours and 5-hours of heat treatment time the Cu-precipitates nucleate. The figure shows that between the untreated specimen and 5-hour heat treatment α decreases. Then between the 5-hour and 300-hour specimens α increases. Note the strain levels for this set of measurements were on the order of 10^{-7} .

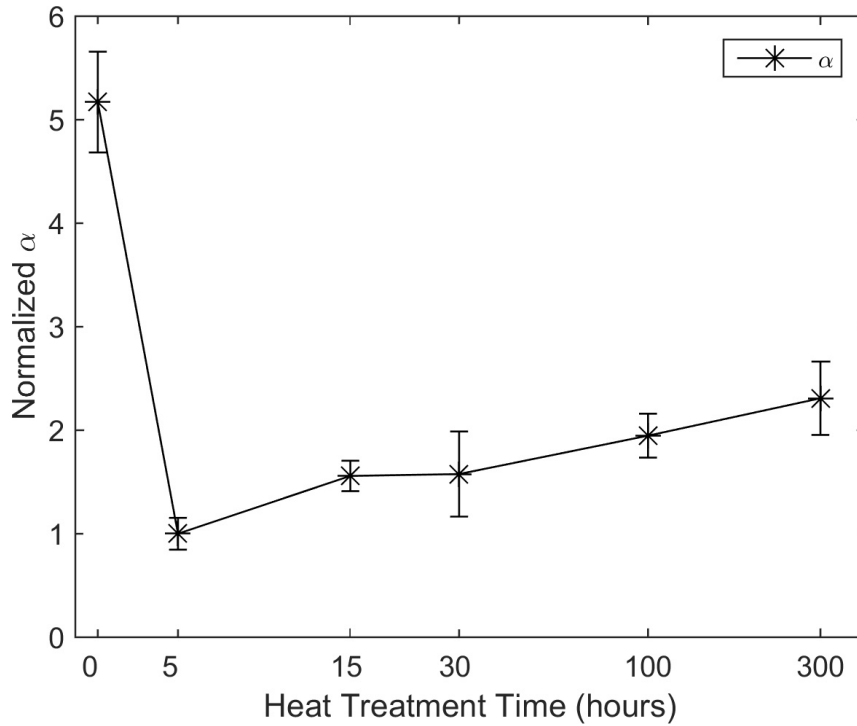


Figure 39. Measurements for α for Fe-Cu specimens comparing effect of heat treatment time where error bars represent the standard error for experimental repeatability

6.4.3 SHG Results

For the SHG measurements, the longitudinal wave technique was used where the experimental procedure can be seen in section 4.2.2. While it is preferable to make Rayleigh wave measurements for SHG, this material was unable to sustain a Rayleigh wave of sufficient amplitude for these measurements. An exhaustive effort was made to try and generate a Rayleigh wave such as creation of new wedges for this material, use of a receiving wedge in place of the air-coupled transducer, as well use of variable angle wedges. It is suspected that attenuation may be a factor with the attenuation of this material being much higher than that of typical stainless steel. However, a concrete

solution cannot be determined without further research which would make an excellent future research topic.

The results for β can be seen in Figure 40 and are the same results shown in the signal processing section 5.5 [86] and shows just the least square results. As can be seen in the figure, β initially decreases from the untreated to 5-hour specimen. β then increases from the 5-hour to 100-hour specimen. β finally decreases from the 100-hour to 300-hour specimen.

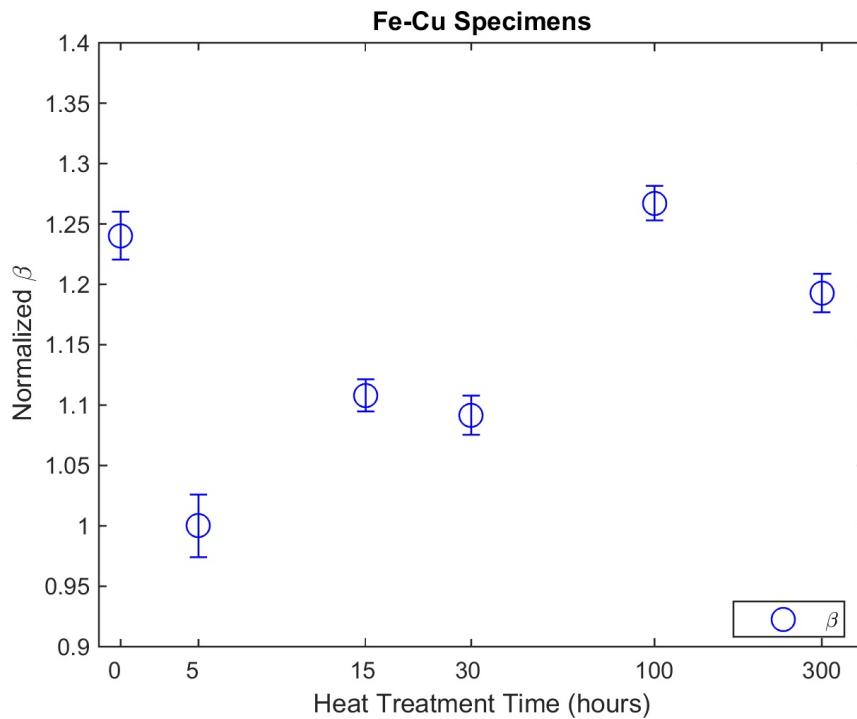


Figure 40. Measurements for β for Fe-Cu specimens comparing effect of heat treatment time [86] where error bars represent the standard error for experimental repeatability

6.4.4 SHG model for Fe-Cu alloy and discussion

As discussed earlier, Cantrell and Yost (later modified by Hurley to account for differences in elastic properties between the matrix and precipitate [16]) developed a theoretical model for precipitate pinned dislocations [15]. Knowing that the Cu-precipitates act as precipitate pinned dislocations, this theoretical model has been applied to this set of Fe-Cu specimens to see how the experimental values compare [6]. The change in the nonlinearity parameter β can be seen in Eq. 120 and is the exact same expression derived in section 2.3.1.2.

$$\Delta\beta = 495 \frac{\Omega\Lambda R^3 C_{11}^2 |\delta| r_{avg}^4}{G^2 b^2 f_n^{1/3}} \left[\frac{3B}{3B + 4G} \right] \quad (120)$$

In this model, Ω , Λ , R , C_{11} , δ , B , G , and b are all material constants and are defined in Table 6. f_n is the volume fraction of Cu-precipitates and can be calculated from the percent weight of Cu in the material which is known to be 1%. Zhu et al found that the volume fraction of Cu reaches equilibrium after approximately 0.5 hours of heat treatment so it can be said that the volume fraction will remain constant as well [71]. r_{avg} is the average radius of the Cu-precipitates which were found using SANS and presented in Table 1 and Figure 18.

Table 6. Constants for theoretical model

Burgers Vector, b	Dislocation Density, Λ	2 nd Elastic Constant, C_{11}	Shear Modulus, G	Schmid Factor, R	γ strain to ϵ strain, Ω	Lattice Misfit, δ	Bulk modulus, B
2.48 Å	$6 \times 10^{13} \text{ m}^{-2}$	286 GPa	83 GPa	0.3	0.3	1.4%	140 GPa
[93–95]	[95–97]	[96,98]	[93–95]	[15,16]	[15,16]	[99,100]	[16]

$\Delta\beta$ can then be calculated for each of the heat treatment times with Cu-precipitate radii information available. The total nonlinearity in the material can then be calculated by adding the change in nonlinearity with the nonlinearity from the lattice material, β_L . The nonlinearity for undamaged Fe polycrystal is well known can be found in the literature as 8.76 [101].

$$\beta = \Delta\beta + \beta_L \quad (121)$$

Once the total nonlinearity was calculated, it was normalized by the lattice nonlinearity so that normalized values may be compared. Figure 41 shows a comparison between the experimentally measured β and the theoretically model β .

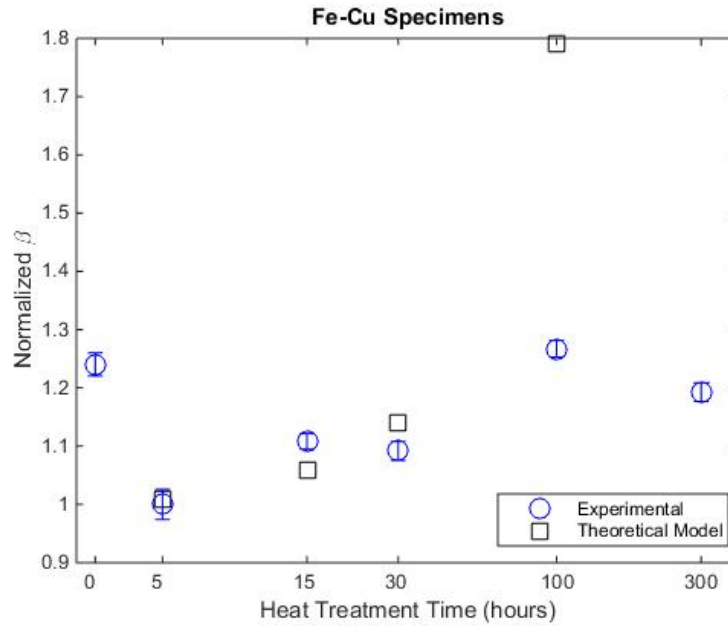


Figure 41. Comparison between experimental and theoretical model for β for Fe-1% Cu [6]

6.4.5 ANOVA results

ANOVA was used to determine the statistical significance of the experimental results. Using the procedure setup in section 2.6, the ANOVA results for α can be seen in Table 7, and the ANOVA results for β can be seen in Table 8. It can be seen that the F-value is much larger than the F-critical value and the P-value is much lower than 0.05. These results show that the null hypothesis is rejected, and the mean values of α and β are significantly different. This significant difference means that the changes in α and β are due to changes in the microstructure and not due to random error.

Table 7. ANOVA results for α for Fe-1.0% Cu

<i>Source of Variation</i>	<i>SS</i>	<i>df</i>	<i>MS</i>	<i>F</i>	<i>P-value</i>	<i>F crit</i>
Between Groups	29273.17	5	5854.64	20.71	3.09E-11	2.4
Within Groups	14416.72	51	282.68			
Total	43689.9	56				

Table 8. ANOVA result for β for Fe-1.0% Cu

<i>Source of Variation</i>	<i>SS</i>	<i>df</i>	<i>MS</i>	<i>F</i>	<i>P-value</i>	<i>F crit</i>
Between Groups	3.28E-07	5	6.56E-08	31.44	2.72E-08	2.77
Within Groups	3.75E-08	18	2.09E-09			
Total	3.65E-07	23				

CHAPTER 7. DISCUSSIONS

7.1 Overview

The previous chapter presented the experimental results found in this research and gave a brief discussion on each of the materials about the sensitivity of the nonlinear ultrasound techniques and the effects of the microstructural mechanisms on each of the techniques. This section will expand this discussion to get a better understand of each of the nonlinear ultrasound techniques and their relationship to the microstructural mechanisms. To provide a more robust discussion, the results from two other research studies (NRUS and SHG) will be provided [18,102]. These other studies looked at materials with microstructural mechanisms different than the ones presented here and will provide even more insight into the techniques.

7.2 Results from previous studies for comparison

7.2.1 17-4PH Stainless Steel

The first results presented are for the 17-4PH stainless steel which was studied by Matlack et al. [2] and Maier et al [18]. When 17-4PH stainless steel is thermally aged at and above 400°C, the material hardens through the formation of Cu-precipitates [103]. Since copper has a low solubility at 400°C and above, the copper atoms will diffuse and form small precipitates. When the Cu-precipitates first form in the material, they will be coherent and will restrict dislocation motion (precipitate pinned dislocations). In this research, the 17-4PH was solution annealed at 1040°C for 6 hours and air cooled to ensure that the initial samples had no Cu-precipitates [2,18]. The samples were then heat

treated at 400°C for 0.1, 1, and 6 hours. The researchers chose this heat treatment temperature to ensure that the dislocation density remained constant throughout thermal aging [2].

Matlack et al. made thermo-electric power (TEP), transmission electron microscopy (TEM), and 3D atom probe tomography (APT) measurements on these specimens [2]. The TEP results showed an increase as heat treatment time increased. This increase in TEP corresponds to a decrease of copper material in the matrix which indicates an increase in the volume fraction of Cu-precipitates. Matlack et al. indicate that this increase in volume fraction of Cu-precipitates likely indicates an increase in the number density of Cu-precipitates in the material. Similar results were seen by TEM and APT and can be seen in full detail in the text [2].

NRUS [18], SHG Rayleigh wave [2], hardness [2], and Young's modulus [18] measurements were all made on these specimens and can be seen in Figure 42. It can be seen that α increases with heat treatment time while β decreases with heat treatment. These changes in α and β are due to the increasing number of Cu-precipitates [2,18]. This is the first time that a difference in the behaviors of α and β has been seen and will provide for an interesting discussion which will be seen in Section 7.3.4. Despite the difference in trends, here again α is shown to be much more sensitive than β to changes in the microstructure.

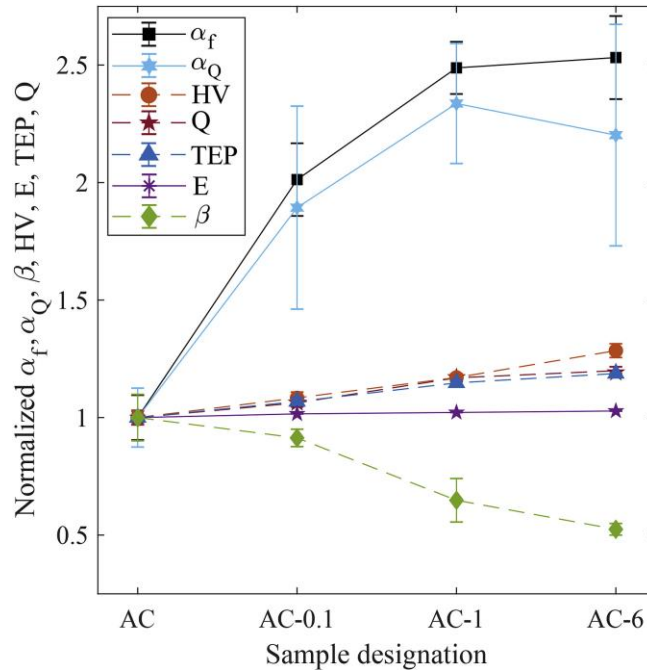


Figure 42. Results for 17-4PH stainless steel specimens [2,18]

7.2.2 Cr9Mo1

The second set of results presented are for a material where the microstructural changes are a little more complicated than the materials previously presented. This material will provide insight into both nonlinearity parameters when there is more than one microstructural mechanism present. For this material, the SHG Rayleigh wave measurements were made by Marino et al. [1], and the NRUS measurements and initial comparison were made by Fahse [102]. When Cr9Mo1 (a modified 9% Cr ferritic martensitic steel) is heat treated, there is a formation of precipitates as well as a change in the dislocation density. There are two types of precipitates that form when this material is thermally aged: $M_{23}C_6$, MX, and M_2X particles which form during tempering and Laves phase and Z-phase which form during further thermal aging. This evolution of Cr9Mo1 is highly cited in the literature [104–108].

Rockwell hardness (HRC) [1], β [1], α [102], and E [102] measurements were all made on this material and can be seen in Figure 43. It can be seen that Rockwell hardness initially decreases and then begins to level off as heat treatment time increases. E sees minimal changes as heat treatment time increases. β and α are seen to initially decrease up to 500 hours of heat treatment time and then increase up to 3000 hours of heat treatment time.

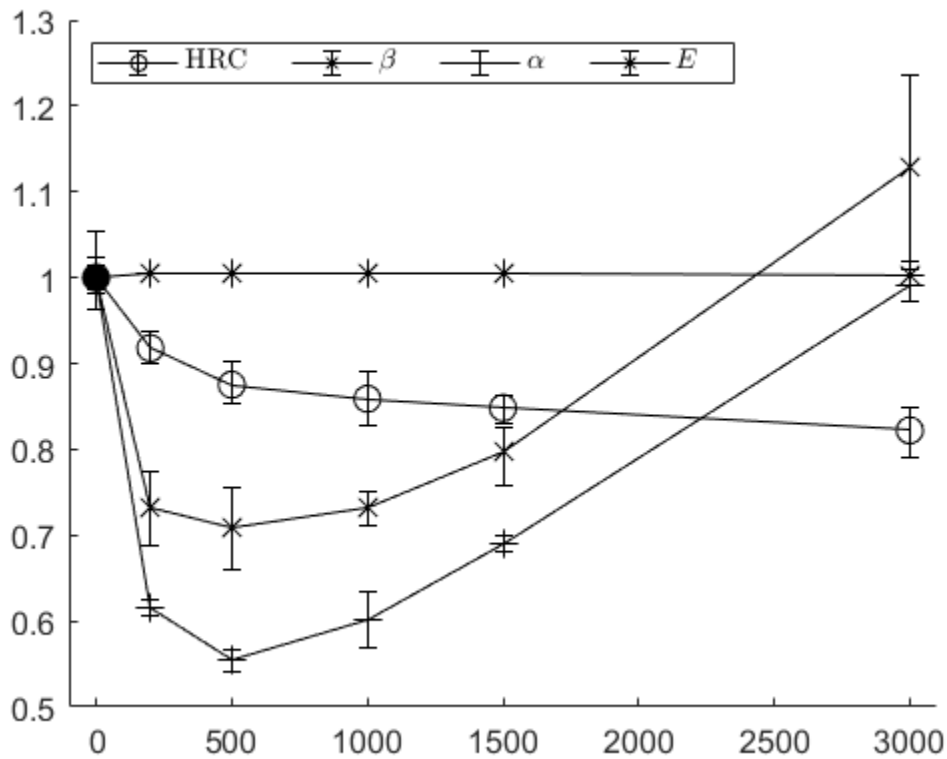


Figure 43. Results for Cr9Mo1 specimens [1,102]

Marino et al. provide a figure that overlays the changes in dislocation density and precipitate radii with heat treatment time which is shown in Figure 44. This shows how the microstructure changes as β changes. The sharp decrease in dislocation density

correlates to the decrease in β and the rapid increase in precipitate radius correlates with an increase in β .

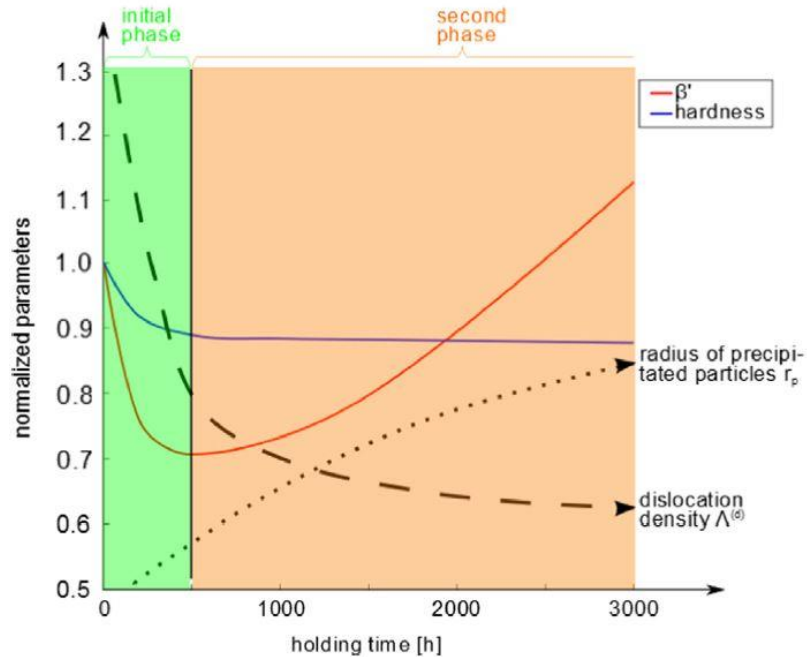


Figure 44. Overlay showing changes in dislocation density, precipitate radius, and β as a function of heat treatment time [1]

7.3 Mechanism Discussion

So far, the results for β and α have been presented for five different materials. While a brief discussion was provided as the results were presented, this section expands upon this discussion to give a better understanding of the techniques and their relationship to the mechanisms. Table 9 shows a summary of the materials that have been presented, their corresponding mechanisms, and the response of β and α . For the most part, β and α have responses similar to one another for each of the mechanisms. However, a couple of differences are seen in the Fe-1.0% Cu and 17-4PH materials and will be discussed.

Table 9. Summary of materials, mechanisms, and β/α response

Material	Microstructural Mechanism	β response	α response
304 - sensitization	Growth of precipitates along grain boundaries	↑	↑
316L - annealed	Removal dislocations from cold working	↓	↓
Fe-1.0% Cu	Nucleation of precipitates	↓	↓
	Precipitate pinned dislocations – growth of precipitate radius	↑ then ↓	↑
17-4PH	Precipitate pinned dislocations – growth in number density of precipitates	↓	↑
Cr9Mo1	Dislocation density decrease	↓	↓
	Growth of precipitate radius	↑	↑

7.3.1 304 – sensitization

As a refresher for discussion, the data for α and β are plotted on the same plot in Figure 45. The figure also shows Young’s modulus, E , which is determined using linear ultrasound (RUS, section 2.4.2). Each of the measurement values is normalized to the annealed sample so that the relative change between the annealed specimen and the sensitized specimen can be seen. As described earlier, when 304 stainless steel is heat treated, chromium carbide precipitates begin to form in and along the grain boundaries and create chromium depletion zones. This is known as sensitization. Figure 13, Figure 14, and Figure 36 demonstrate through both EPR and microscopy results that this sensitization is happening in the specimen being studied and is a completely separate measure from the ultrasound measurements. The EPR results give the DOS (degree of sensitization) and show that the annealed specimen is non-sensitized and the heat treated specimen is sensitized. The microscopy results confirm the EPR results and give a visual understanding of these chromium carbides.

Figure 45 shows that the nonlinear ultrasound measurements (α and β) are much more sensitive to changes in the microstructure than the linear ultrasound measurements (E). The changes in α and β are over 20% while the change in E is approximately 1%. This difference between the linear and nonlinear measurements demonstrates that the nonlinear ultrasound techniques are much more sensitive to these small length scale material changes than the linear ultrasound techniques.

Now when looking at just the nonlinear measurements, it can be seen that both α and β significantly increase between the annealed and sensitized state, 43% and 25%, respectively. These carbides act as an asperity in the grain boundary which generates the nonlinearity in the material meaning that increases in both β and α between the non-sensitized and sensitized states are due to this interaction between the carbide and the grain boundary.

As discussed earlier, it is known that hysteresis nonlinearity is affected by energy dissipation such as friction and contact. It is believed that contact and friction are generated between the carbide and the grain boundaries when the ultrasonic wave is propagated through the material leading to an increase in α .

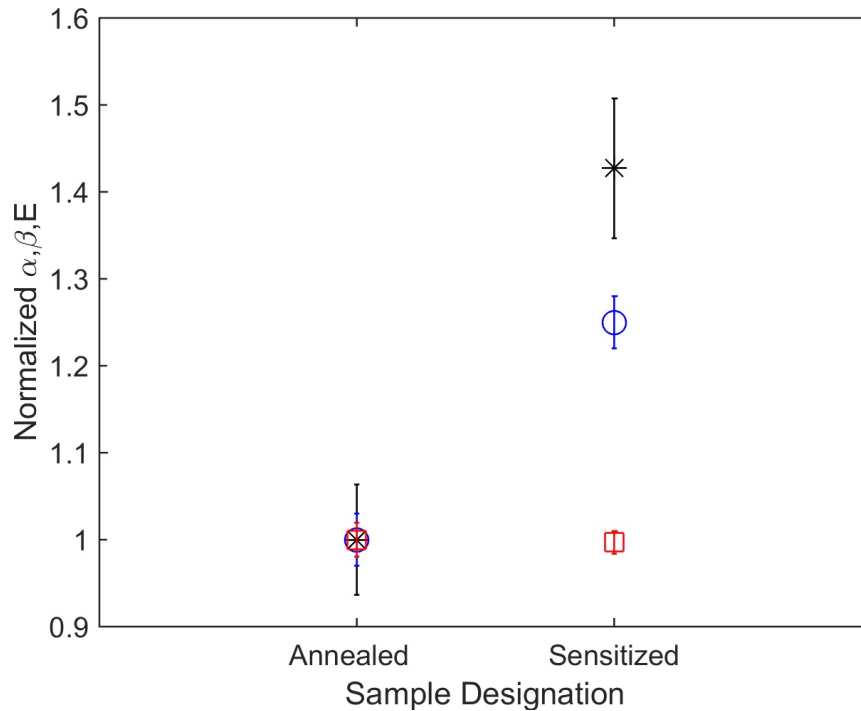


Figure 45. Comparison of α , β [29], and E for annealed and sensitized 304 where error bars represent the standard error for experimental repeatability

7.3.2 316L – annealed

Similar to the 304 specimens, the results for NRUS and SHG are plotted on the same figure for easy comparison. The results for E are added for a comparison to the linear measure. These three values can be seen in Figure 46. Again, by first doing a comparison between the nonlinear and linear ultrasound techniques, it can be seen that both α and β are much more sensitive to the small changes in the microstructure than E is, >20% vs. 1%.

Next, it can be seen that both α and β decrease between the as-received and heat treated states by 44% and 20%, respectively. This is because when the as-received sample is annealed some dislocations are removed (decrease in dislocation density) from the material relieving some of the residual stress in the material. As presented in section

3.3, previous work has shown that annealing metals will remove dislocations. Looking back at the model by Granato and Lücker on the damping and hysteresis loss from a vibrating pinned dislocation gives an explanation of why the reduction in dislocation density results in a decrease of α [43].

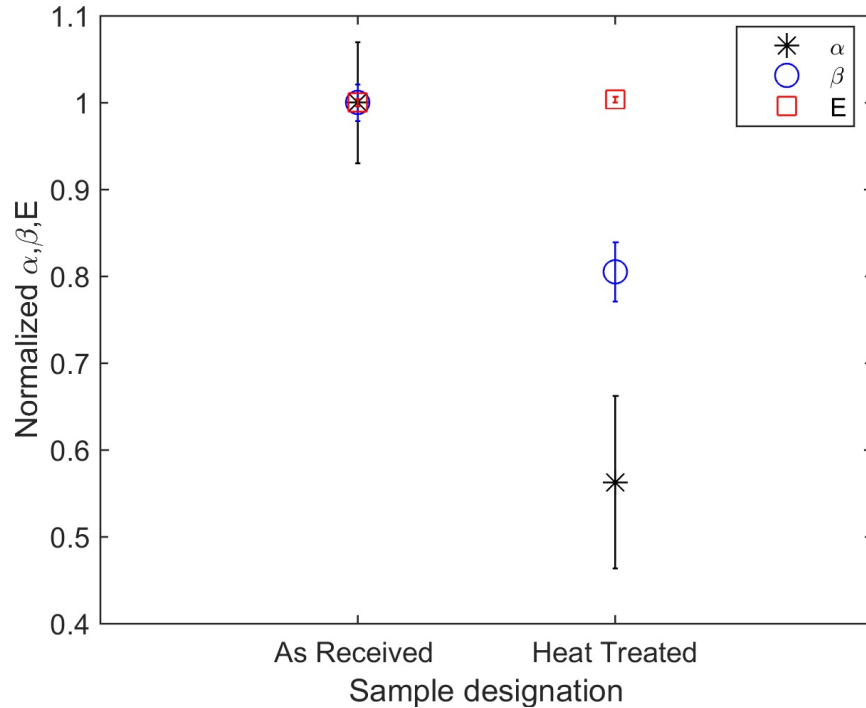


Figure 46. Comparison of α , β , and E for as received and heat treated 316L where error bars represent the standard error for experimental repeatability

7.3.3 Fe-1.0% Cu

The two nonlinear ultrasound results, as well as the linear ultrasound results, have been plotted on the same figure and can be seen in Figure 48. Similar to the other materials, the sensitivity of E due to changes in the microstructure is smaller than the changes in α and β , a maximum of 10% compared to 95% and 27%, respectively.

Now focusing on the nonlinear results, the figure shows that until the 100-hour heat treatment mark, both α and β have similar trends. From the untreated specimen to the 5-hour specimen, α and β decrease in value. This decrease in the nonlinearity is due to the nucleation of Cu-precipitates. A similar trend was seen by Cantrell and Yost in the nucleation of precipitates in a different material. Additionally, a molecular dynamics model was created to model the nonlinear ultrasound response to voids, Cu atoms, and Cu-precipitates in BCC Fe [109]. They looked at how the concentration of these mechanisms effected the relative change of the nonlinearity parameter. It was seen that as the concentration of Cu atoms and Cu-precipitates (radius remained constant) increased there was a decrease in the nonlinearity parameter as seen in Figure 47. From their model, they found that as concentration increases, Cu-precipitates decrease the classical nonlinearity at twice the rate that Cu-atoms do. These results can lead to the conclusion that the clustering of Cu-atoms into precipitates decreases the classical nonlinearity.

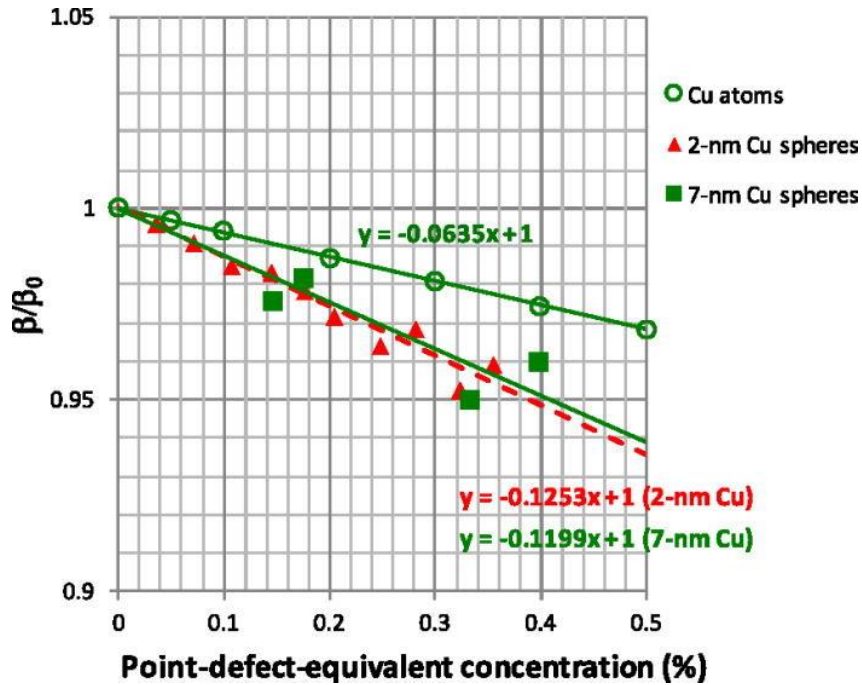


Figure 47. Comparison of classical nonlinearity from Cu atoms and Cu precipitates with increasing point-defect-equivalent concentration [109]

From the 5-hour specimen to the 300-hour specimen, there is a growth in the radii of the Cu-precipitates which is the cause of the nonlinearity in the material. This growth can clearly be seen from the SANS measurements in Figure 18. While these Cu-precipitates are the source of the nonlinearities in the material, the explanations for the behaviors of α and β will be discussed separately.

The discussion will begin by looking at the response of β . From the 5-hour specimen to the 30-hour specimen, there is an increase in β . This increase in nonlinearity is due to the interaction between the Cu-precipitates and the dislocations in the material creating precipitate pinned dislocations. Eq. 122 reminds the reader of the theoretical model for precipitate pinned dislocations proposed by Cantrell and Yost [15] that was seen in section 6.4.4. This model shows that the change in β is a function of material constants,

the volume fraction of precipitates, and the average radius of the precipitates. As discussed in section 6.4.4, the average radius of the precipitates is the only parameter in the model that changes with heat treatment time. This means that the change in β is a function of the Cu-precipitate radii to the fourth power.

$$\Delta\beta = 495 \frac{\Omega\Lambda R^3 C_{11}^2 |\delta| r_{avg}^4}{G^2 b^2 f_n^{1/3}} \left[\frac{3B}{3B + 4G} \right] \quad (122)$$

When looking at the Cu-precipitate radius for the 100-hour specimen, the radius of the precipitate is larger than the critical radius where the Cu-precipitate transitions from BCC with the Fe-matrix to 9R with the Fe-matrix. As discussed in section 3.4.3, when the Cu-precipitates transition from BCC to 9R, there is a loss of coherency between the Cu-precipitates and the Fe-matrix. This structure transition leads to a reduction in the eigenstrain [7]. It would be expected that this loss in coherency would decrease β , and Li et al demonstrates this by showing that a reduction in the eigenstrain leads to a decrease in β [7]. However, it can clearly be seen that there is an increase in β for the 100-hour specimen. This may be due to two reasons. One reason is that some of the Cu-precipitates will remain coherent with the Fe-matrix which would result in an increase in β . The second reason is as the Cu-precipitates transform from a BCC structure to a 9R structure, some of the pinned dislocations will become unpinned which will lead to an effectively longer loop length (producing an increase in β). These unpinned dislocations and the aforementioned loss of coherency would compete with each other, and eventually β will turn down. This decrease of β is seen in the 300-hour specimen.

When looking at the results for α , it can be seen that after nucleation starts α continues to increase as the radii of the Cu-precipitates grow. Since hysteresis nonlinearity is due to energy loss mechanisms such as friction and contact, this increase in α is believed to be due to both dislocation vibration as well as the contact between the Cu-precipitates and the Fe-matrix. The Granato and Lücke model of damping from pinned dislocations demonstrates the contribution of dislocation vibration to loss [43] and is a function of the dislocation density and the loop length. The hysteresis nonlinearity from the Cu-precipitates arises from the contact between the Cu-precipitates and the Fe-matrix and acts as a function of the surface area between the two. This means that as the size of the Cu-precipitates grows the surface area between the Cu-precipitates and the Fe-matrix will increase resulting in an increase in α . Additionally, when there is a loss of coherency between the Cu-precipitate and the Fe-matrix (at the 100-hour and 300-hour specimens), the contact between the Cu-precipitate and Fe-matrix may be considered even rougher leading to even more energy loss due to contact. This rougher contact would increase α even more.

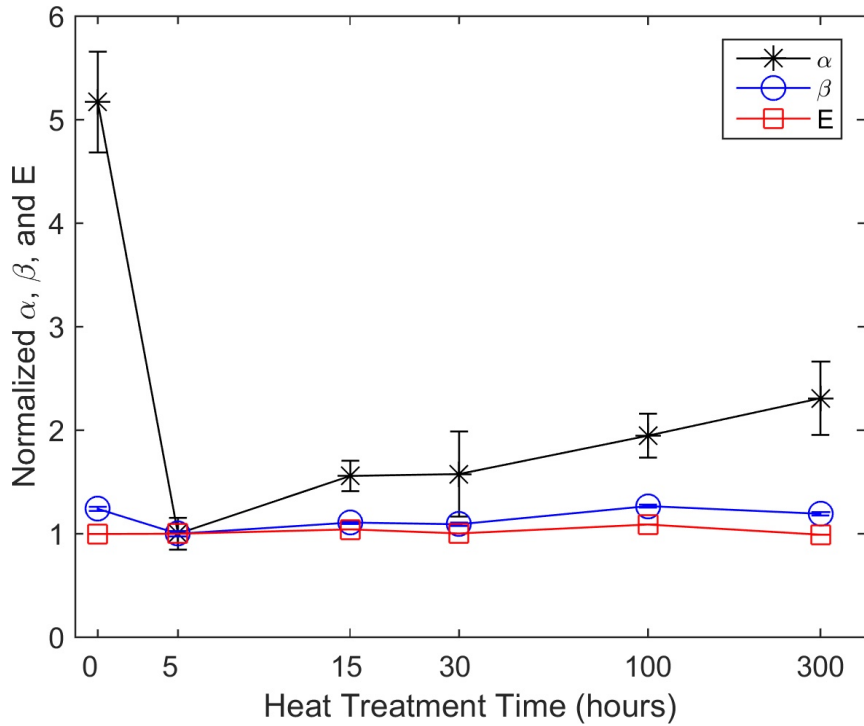


Figure 48. Comparison of α , β , and E results for Fe-1% Cu specimens (β from [86]) where error bars represent the standard error for experimental repeatability

7.3.3.1 Comparison of experimental β to models

Looking back in the results section, Figure 41 shows a comparison between the experimentally measured β and the theoretically modeled β . For 5-hours, 15-hours, and 30-hours, the theoretical model follows the values of the experimental trend for β fairly well. However, at 100-hours of heat treatment time, the model diverges from the experimental data. This is due to the loss in coherency between the Cu-precipitates and Fe-matrix. One of the assumptions of the theoretical model is the precipitates are coherent with the matrix. However as seen earlier, the Cu-precipitates become semi-coherent with the Fe-matrix at 100-hours of heat treatment time so the assumptions of the model are no longer valid.

After these results were published, Li et al developed an analytical model for ultrasonic propagation in Fe-Cu alloy [7]. In this model, the authors account for the loss of coherency between the Cu-precipitates and the Fe-matrix, and the model follows these experimental results very well as can be seen in Figure 49. This figure shows an overlay of the experimental measurements on the model that was developed by Li et al allowing for a comparison between the two.

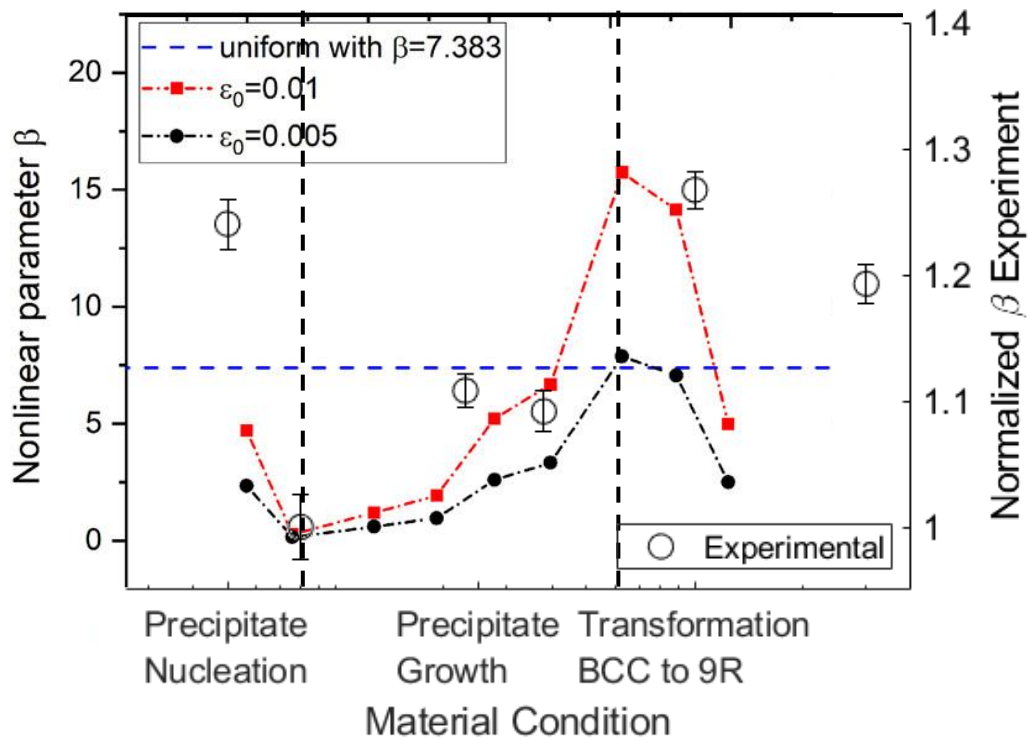


Figure 49. Analytical model by Li et al for Fe-Cu alloy [7] overlaid with experimental measurements

7.3.4 17-4PH

When looking at the results for the 17-4PH specimens from Maier et al and Matlack et al [2,18], the difference in the response of α and β can clearly be seen where α

increases as a function of heat treatment time and β decreases as a function of heat treatment time. In the 17-4PH specimens, the Cu-precipitates pin dislocations creating similar precipitate pinned dislocations as seen in Fe-Cu specimens. However, in these specimens, the radii of the Cu-precipitates remain constant while the number density of Cu-precipitates increases. Using the Cantrell and Yost theoretical model for change in β due to precipitate pinned dislocations [15], Matlack et al showed that the decrease in β was from the increase in the number density of precipitates. The base of the model can be seen in Eq. 123. This time the equation for the precipitate spacing, L , will be a function of the number density of precipitates instead of a function of the precipitate radii and volume fraction of precipitates as presented for the Fe-Cu specimens where $L = N^{-1/3}$.

$$\Delta\beta = 154 \frac{\Omega\Lambda R^3 C_{11}^2 |\delta| r_{crit}^3 L}{G^2 b^2} \quad (123)$$

Using this equation for the precipitate spacing, the equation for the change in β becomes

$$\Delta\beta = 154 \frac{\Omega\Lambda R^3 C_{11}^2 |\delta| r_{crit}^3}{G^2 b^2 N^{1/3}} \quad (124)$$

This equation shows that β is a function of the material constants, dislocation density, precipitate radii, and number density of precipitates. For the 17-4PH specimens, the dislocation density and precipitate radii remain constant throughout the heat treatment while the number density of precipitates increases with increasing heat treatment time. This shows that β should decrease as the number density of precipitates increases as was seen experimentally.

When looking at the results for α from Maier et al [18], it can be seen that response for α is in the opposite direction. The increase in α may be due to an additive effect. In section 7.3.3, the hysteresis nonlinearity was said to come from dislocations as well as the contact between the precipitates and the matrix. The amount of contact between the precipitates and the matrix can be calculated as the surface area of the precipitates. In this case, when the number density of precipitates increases, the amount of surface area between the precipitates and matrix will increase resulting in an increase in contact points. This increase in contact will result in an increase in α .

7.3.5 *Cr9Mo1*

Looking at the results for the Cr9Mo1 specimens from Marino et al and Fahse [1,102] the response of α and β can be seen. As discussed in section 7.2.2, the changes in the microstructure of Cr9Mo1 from heat treatment are more complicated than the other four materials presented here because there are multiple microstructural mechanisms. The mechanisms can be summarized as a decrease in dislocation density and a growth in precipitates. As can be seen in Figure 44, there is a rapid decrease in the dislocation density from 0 to 500 hours of heat treatment time and then it begins to level off for longer heat treatment times. During this time, the precipitates begin to nucleate and grow as heat treatment time increases. Marino et al and Fahse suggest that the change in nonlinearity in the material can be broken into two phases: the first phase where both nonlinearity parameters decrease is dominated by the decrease in dislocation density and precipitate nucleation and the second phase where both nonlinearity parameters increase dominated by the growth of the precipitates. These results show that while there are two competing mechanisms the nonlinearity parameters still show a significant response to

the changes. These results suggest that there may be a critical precipitate radius where the nonlinear contribution from precipitates dominates the nonlinear contribution from dislocations. While this material is very complicated and still not fully understood, these results show that it is possible to make measurements on a material with multiple mechanisms and get a better understanding of the material.

7.3.6 *Summary*

This section has shown the relationship between α and β and three prominent microstructural mechanisms: dislocations, precipitate pinned dislocations, and precipitate growth in and along the grain boundaries. Understanding how these mechanisms relate to α and β allows for better material damage characterization in the future. Additionally, understanding the response to individual mechanisms builds the foundation for the understanding of more complicated materials in the future.

These results have shown that depending on the mechanism α and β may respond similarly or differently to the microstructural mechanisms. This lends itself to the conclusion that the physics behind their response is different. α is sensitive to energy loss mechanisms such as friction and contact and seems to be an additive response while β is sensitive to specific interactions between microstructural components.

It is of interest to mention that in all the results the percent change in α is generally much higher than the change in β . This lends itself to the conjecture that α is more sensitive to the changes in the microstructure than β is. However, other possibilities such as ease of measurement technique may lend a hand in the exact sensitivities. Leading with the notion that α is more sensitive than β , the question remains: why not always

make NRUS measurements instead of SHG measurements? The answer to this is that while NRUS may provide important information about the material it is not a practical technique to use *in-situ* and on complicated geometries. In contrast, SHG, especially Rayleigh waves, has the potential for easy field measurements where it is not practical to assume a uniform geometry.

CHAPTER 8. CONCLUSIONS AND FUTURE WORK

8.1 Summary of Results

This research has shown the sensitivity and abilities of SHG and NRUS to detect microstructural damages in metals such as dislocations, precipitates in the grain boundaries, precipitate pinned dislocations, and a combination of mechanisms. This is the first time this field has seen the response of α to these changes in the microstructure of the metals. The analysis of the physics behind the responses of α and β to the presented microstructural mechanisms provides a novel look into these two nonlinear ultrasound techniques.

The removal dislocations from cold working was investigated by looking at an as-received and an annealed specimen. It is known that when a sample is annealed some of the pre-existing dislocations are removed and the residual stresses are relieved to some degree. The results for β and α show that both classical and hysteresis nonlinearities in a material decrease when dislocations are removed. This confirms the theoretical models that link dislocations and both types of nonlinearity. Hikata et al. showed that an increase in dislocation density will lead to an increase in β through their pinned dislocation model [31]. Additionally, Granato and Lücke modeled a pinned dislocation segment and showed that an increase in dislocation density increased the decrement in the material [43]. This research confirmed these theoretical conjectures.

The growth of precipitates in the grain boundaries was studied by comparing a sensitized and non-sensitized sample. It was found that there is an increase in both α and

β between the non-sensitized and sensitized samples. For α , this increase is attributed to the contact/friction between the chromium carbides and the grain boundary. For β , this increase is due to added stress caused by this abnormal growth in the grain boundaries.

There were two samples studied which looked at the effect of precipitate pinned dislocations on classical and hysteresis nonlinearity. The first set of samples (Fe-1.0% Cu) looked at the effects of nucleation and growth of Cu-precipitates on the nonlinearity parameters. For both α and β , there is a decrease in the nonlinearity parameters from the untreated specimen to the 5-hour specimen. This decrease is due to the nucleation of the Cu-precipitates. From the 5-hour specimen to the 30-hour specimen, there is a growth in the radii of the Cu-precipitates. The contact between the Cu-precipitates and the Fe-matrix results in an increase in α for these specimens. As the precipitate radii grow, there is an increase in surface area between the precipitates and the matrix. The increase in β is due to the precipitate dislocation interaction where as the radii of the Cu-precipitates increases the classical nonlinearity will also increase. At the 100-hour specimen, there is a loss of coherency between the Cu-precipitates and the Fe-matrix. This loss in coherency seems to add to the hysteresis nonlinearity with α continuing to increase all the way to the 300-hour specimen. It is believed that a combination of this rough contact caused by the coherency loss and the growing surface area between the precipitates and the matrix contributes to α . β sees an initial increase from the 30-hour specimen to the 100-hour specimen and then a decrease from the 100-hour specimen to the 300-hour specimen. This increase is due to some of the precipitates remaining coherent with the matrix as well as longer loop lengths. The decrease is due to the loss in coherency between the precipitates and the matrix.

The second set of samples (17-4PH) looks at the effect of the number of precipitates on the nonlinearity of the material. As this material is heat treated, the radii of the precipitates remain the same while the number density increases. In this material, a difference in the response of α and β was seen. α increased with an increase in number density of precipitates while β decreased. This difference in the nonlinearity parameters is due to relationship between the physics of the mechanisms and the type of elastic nonlinearity. For α , the increase is due to the increased surface area contact between the precipitates and the matrix as the number of precipitates increases. For β , the decrease is due to the pinning of dislocations as the number increases.

8.2 Recommendations for future work

This research has shown the capabilities of the experimental techniques and briefly introduced a few models. However, this area of research would greatly benefit from expanding theoretical and analytical models for the different microstructural mechanisms. While there are multiple models for SHG, there are only few models for NRUS and hysteretic nonlinearity. These models would allow for a better understanding between the mechanisms and the theory. So far, it has been seen that different mechanisms increase the hysteretic nonlinearity for geomaterials (previous research, [38,39]) and for metals (this research), and an overview of their physics is understood. Models would allow for a better understanding of the physics behind the mechanisms.

While this research studies a wide range of mechanisms, it would be of interest to study even more mechanisms to have a bank that encompasses a wide range of building blocks for more complicated materials. Examples of other mechanisms may include grain

size and aligned microcracks. It would be interesting to see how crack orientation affects the measure of hysteresis nonlinearity. It would be expected that if the cracks are aligned with the propagating wave then the friction from the movement of the cracks would be larger than the perpendicular propagation direction. It would also be interesting to see how a higher strain level effects α for a material with microcracks. As the strain level increases, the microcracks will open more and more and will eventually clap.

Additionally, more materials with multiple mechanisms should be considered to understand the effect that mechanisms may have on one another. This would allow for a better understanding of complicated materials.

8.3 Significance and Impact

This research has provided an understanding of the relationship between several microstructural mechanisms and classical and hysteretic nonlinearity. It has provided an understanding of how the mechanisms work and how the interaction between the microstructure and acoustic waves affects the nonlinearity parameters. An understanding of these building block mechanisms will allow for better material damage detection in the future. If the relationship between a single mechanism and the nonlinear ultrasound response is understood, then the response of a material with multiple mechanisms or damage can be predicted. When looking at real world problems and materials, this is very important because these materials typically have multiple damages in the material.

If these experimental NDE measurements can be made *in-situ*, then this model for the microstructural mechanisms will allow for an understanding of these structures and the current state of the microstructure. These nonlinear ultrasound parameters can then be

related to material properties through theoretical models. This relationship would then allow for quantitative modeling of the remaining life of structures. Remaining life predictions will permit these structures to be in service longer than was originally intended and provide for a safer community.

APPENDIX A. THEORY FOR SIGNAL PROCESSING METHODS

A.1 Discrete Fourier Transform

The discrete Fourier transform is similar to a continuous Fourier transform but deals with a discrete time signal. The discrete Fourier transform can be defined using Eq. 125 and a full derivation and explanation can be found in a book written by Marple [84].

$$X[k] = \sum_{n=0}^{N-1} x[n]e^{-j2\pi kn/N} \quad (125)$$

A.2 Prony Method

While a full derivation of Prony's method can be found here, a detailed description can also be found in a book written by Marple [84]. Prony's method is a signal modeling method where a linear combination of exponentials is fit to a set of data points [84]. For the NLU measurements described in this paper, the linear combination of exponentials represents the summation of sinusoidal signals (fundamental and higher harmonic frequencies) which make up the received signal. Fitting this linear combination to the received data allows for the computation of frequencies that make up the signal along with their corresponding amplitude, phase angle, and damping factor. This section gives a brief description of the steps found in Prony's method. Future sections will give a description on how to solve these steps using either the original Prony method or one of the modifications (least squares or known poles).

In general, Prony's method can be thought of comprising three steps. The first step consists of developing a model that fits p exponentials to the data (finite sample with N discrete data points) and determining the corresponding parameters. These parameters can then be used to develop a polynomial in the second step, and the roots of this polynomial are determined. These roots can then be used to determine the frequencies of the signal and the corresponding damping factors. The corresponding amplitudes and phase angles can then be determined in the third step from these values. An in-depth discussion of each of these steps is as follows.

Step 1

The Prony prediction model for the SHG measurements can be seen in Eq. 126 where A_k is the amplitude, α_k is the damping, f_k is the frequency, θ_k is the phase angle, and T is the sampling interval in seconds (1/sampling frequency):

$$\hat{x}[n] = \sum_{k=1}^p A_k e^{(\alpha_k + j2\pi f_k)(n-1)T + j\theta_k} = \sum_{k=1}^p h_k z_k^{n-1} \quad 1 \leq n \leq p \quad (126)$$

Note that Eq. 126 is simplified by the substitution of h_k in for $A_k e^{j\theta_k}$ and z_k in for $e^{(\alpha_k + j2\pi f_k)T}$. It is easier to visualize Eq. 126 when it is expanded into a matrix form as:

$$\begin{bmatrix} \hat{x}[1] \\ \hat{x}[2] \\ \vdots \\ \hat{x}[p] \end{bmatrix} = \begin{bmatrix} z_1^0 & z_2^0 & \cdots & z_p^0 \\ z_1^1 & z_2^1 & \cdots & z_p^1 \\ \vdots & \cdots & \ddots & \vdots \\ z_1^{p-1} & z_2^{p-1} & \cdots & z_p^{p-1} \end{bmatrix} \begin{bmatrix} h_1 \\ h_2 \\ \vdots \\ h_p \end{bmatrix} \quad (127)$$

The best way to solve this equation is to solve for z_k separately. This is done by creating a characteristic equation (p^{th} order polynomial $\emptyset(z)$ with z_k as its roots) which can be expanded into the following power series:

$$\emptyset(z) = \prod_{k=1}^p (z - z_k) = \sum_{m=0}^p a[m]z^{p-m} \quad (128)$$

The complex coefficient of $a[0]$ is equal to one. A comparison can be made between Eq. 126 and Eq. 128 when Eq. 126 is multiplied by $a[m]$, the indices are shifted from n to $n-m$, the entire equation is summed over the range of $m=0$ to p , and the relationship of $z_i^{n-m-1} = z_i^{n-p} z_i^{p-m-1}$ is substituted into the equation. These changes lead to the following, which is valid for the range $p + 1 \leq n \leq 2p$, or:

$$\sum_{m=0}^p a[m]\hat{x}[n-m] = \sum_{k=0}^p h_k z_k^{n-p} \sum_{m=0}^p a[m]z_k^{p-m-1} = 0 \quad (129)$$

Through close inspection of Eq. 129, it can be seen that the third summation is equal to $\emptyset(z_k)$. With the understanding that z_k is a root of $\emptyset(z)$, it is known that the third summation ($\sum_{m=0}^p a[m]z_k^{p-m-1}$) is equal to zero (resulting in Eq. 129 being equal to zero). Thus, it can be concluded that the first summation is equal to zero, or:

$$\sum_{m=0}^p a[m]\hat{x}[n-m] = 0 \quad (130)$$

Since $a[0]$ is equal to one, Eq. 130 can be rewritten in the following form:

$$\hat{x}[n] = - \sum_{m=0}^p a[m] \hat{x}[n - m] \quad (131)$$

The different versions of the Prony method use different methods to calculate the complex coefficients, $a[m]$. In the original Prony method, an exact fit is made between the model and the discrete signal ($\hat{x}[n] = x[n]$ and $p=N/2$) meaning the complex coefficients are solved for directly using Eq. 131.

Step 2

In step 2, the complex coefficients are used to determine the roots of the polynomial equation, z_k , as follows:

$$z^p + a_1 z^{p-1} + \dots + a_{p-1} z + a_p = (z - z_1)(z - z_2)(\dots)(z - z_p) \quad (132)$$

These roots can be used to calculate the frequencies of the signal as well as the corresponding damping factors in the following way:

$$f_k = \frac{\tan^{-1} \left(\frac{\text{Im}\{z_k\}}{\text{Re}\{z_k\}} \right)}{2\pi T} \quad [\text{Hertz}] \quad (133)$$

$$\alpha_k = \frac{\ln|z_k|}{T} \quad [\text{seconds}^{-1}] \quad (134)$$

Step 3

This step calculates h_k , as well as the amplitudes and phase angles. The method to calculate h_k is dependent on the version of the Prony method being used. In the original Prony method, h_k is solved for directly using Eq. 127. Once the values for h_k are determined, the amplitudes and phase angles which correspond to the frequencies calculated in step 2 can be determined using Eqs. 135 and 136, respectively:

$$A_k = |h_k| \quad (135)$$

$$\theta_k = \tan^{-1} \left(\frac{\text{Im}\{h_k\}}{\text{Re}\{h_k\}} \right) \quad [\text{radians}] \quad (136)$$

A.2.1 Least Squares Prony Method

Modifications have since been made to the original Prony method to adapt to varying conditions. The LS Prony method was developed to be used when the number of data points exceeds the number of data points needed to fit the model to the data (overdetermined) [84]. This method is not an exact fit to the data as was used in the original Prony method. Instead, it minimizes the squared error through the determination of the parameters z_k and h_k .

In the LS Prony method, the determination of z_k is calculated using a least squares covariance linear prediction algorithm. Eq. 130 is modified by the introduction of the linear prediction approximation error, $e[n]$, creating a forward linear prediction error equation:

$$\sum_{m=1}^p a[m]x[n-m] = e[n] \quad (137)$$

where $a[m]$ is the linear prediction parameter. $a[m]$ is determined through the minimization of the linear prediction squared error, ρ ,

$$\rho = \sum_{n=p+1}^N |e[n]|^2 = xvec^T xvec + 2xvec^T Xa[m] - a[m]^T X^H Xa[m] \quad (138)$$

by taking the derivative of ρ and setting it equal to zero [85], $a[m]$ is obtained as:

$$a[m] = (X^H X)^{-1} (X^H xvec) \quad (139)$$

where:

$$xvec = \begin{bmatrix} x[p+1] \\ x[p+2] \\ \vdots \\ x[N] \end{bmatrix} \quad (140)$$

and

$$X = \begin{bmatrix} x[p] & x[p-1] & \cdots & x[1] \\ x[p+1] & x[p] & \cdots & x[2] \\ \vdots & \vdots & \ddots & \vdots \\ x[N-1] & x[N-2] & \cdots & x[N-p] \end{bmatrix} \quad (141)$$

The values of z_k can then be calculated using Eq. 132. The values for h_k are solved through the minimization of the linear prediction squared error as was done for $a[m]$ and the final equation is:

$$h_k = (z^H z)^{-1} (z^H xvec) \quad (142)$$

A.2.2 Known Poles Prony Method

Often times some of the frequencies are known a priori, but their amplitudes may be unknown [79] as is the case for SHG. Consider q known frequencies/damping factors which can be used to calculate q z-exponentials.

A characteristic equation can be written using these z- exponentials as seen in Eq. 143 where $c[k]$ are the characteristic coefficients associated with the q frequencies and $c[q] = 1$.

$$\prod_{k=0}^q (z - z_k) = \sum_{k=0}^q c[k] z^k \quad (143)$$

Calculating the characteristic coefficients associated with the known poles will be the first step. For the purposes of this thesis, the example for SHG will be used to demonstrate the concepts. For SHG, the known frequencies are f_1 (fundamental frequency) and f_2 (second harmonic frequency), and the corresponding damping factors (α_1 and α_2) are zero. In this case, there are four known poles: one for each of the

harmonic frequencies and their corresponding negative frequencies, and can be calculated using the following equation

$$z_k = e^{(\alpha_k + j2\pi f_k)T} \quad (144)$$

The characteristic coefficients, $c[k]$, associated with these z -exponentials can be calculated using Eq. 142.

The characteristic polynomial for all p -components can be factored into two components: the known poles and the unknown poles

$$\sum_{m=0}^p a[m]z^m = \left(\sum_{k=0}^q c[k]z^k \right) \left(\sum_{i=0}^{p-q} \gamma[i]z^i \right) \quad (145)$$

By equating similar powers of z , one obtains the following expression for $a[m]$

$$a[m] = \sum_{k=0}^q c[k]\gamma[m-k] \quad (146)$$

This expression for $a[m]$ can be substituted into Eq. 130 to yield the following equation

$$\sum_{m=1}^p a[m]x[n-m] = \sum_{m=1}^p \left(\sum_{k=0}^q c[k]\gamma[m-k] \right) x[n-m] = 0 \quad (147)$$

$$p+1 \leq n \leq 2p$$

Eq. 147 can be rewritten in such a way that is solely a function of $\gamma[m]$ and $y[n-m]$ as seen in Eq. 148 where $y[n-m]$ is the original data filtered using the known poles (Eq. 149).

$$\sum_{m=0}^{p-q} \gamma[m]y[n-m] = 0 \quad (148)$$

$$p+1 \leq n \leq 2p$$

$$y[n] = \sum_{k=0}^q c[k]x[n-k] = 0 \quad (149)$$

$$p+1 \leq n \leq 2p$$

The second step for the KP Prony method is to filter the original data using the known characteristic coefficients $c[k]$ as is shown in Eq. 149. The filtered data, $y[n]$, can

then be processed using the least squares covariance linear prediction algorithm as was seen in the LS Prony method to solve for $\gamma[m]$ (unknown poles). These characteristic coefficients for the unknown poles, $\gamma[m]$, can be used to calculate the unknown z-exponentials by calculating the roots of the characteristic equation. These z-exponentials are then combined with the known z-exponentials as seen in Eq. 150. Now that all of the z-exponentials are known the frequencies and corresponding damping factors of the measured data can be calculated using the equations provided in the general Prony method section.

$$z_k = [z_{known} \quad z_{unknown}] \quad (150)$$

The final step is to use these z_k values to calculate the values of h_k using the procedure provided in the LS Prony method. Once the h_k values are known, the values for the corresponding amplitudes and phase angles can be calculated using the equations provided in the general Prony method section.

REFERENCES

- [1] Marino D, Kim J-Y, Ruiz A, Joo Y-S, Qu J, Jacobs LJ. Using nonlinear ultrasound to track microstructural changes due to thermal aging in modified 9%Cr ferritic martensitic steel. *NDT & E International* 2016;79:46–52. doi:10.1016/j.ndteint.2015.12.002.
- [2] Matlack KH, Bradley HA, Thiele S, Kim J-Y, Wall JJ, Jung HJ, et al. Nonlinear ultrasonic characterization of precipitation in 17-4PH stainless steel. *NDT & E International* 2015;71:8–15. doi:10.1016/j.ndteint.2014.11.001.
- [3] Matlack KH, Kim J-Y, Wall JJ, Qu J, Jacobs LJ, Sokolov MA. Sensitivity of ultrasonic nonlinearity to irradiated, annealed, and re-irradiated microstructure changes in RPV steels. *Journal of Nuclear Materials* 2014;448:26–32. doi:10.1016/j.jnucmat.2014.01.038.
- [4] Matlack KH, Wall JJ, Kim J-Y, Qu J, Jacobs LJ, Viehrig H-W. Evaluation of radiation damage using nonlinear ultrasound. *Journal of Applied Physics* 2012;111:054911. doi:10.1063/1.3692086.
- [5] Ruiz A, Ortiz N, Medina A, Kim J-Y, Jacobs LJ. Application of ultrasonic methods for early detection of thermal damage in 2205 duplex stainless steel. *NDT & E International* 2013;54:19–26. doi:10.1016/j.ndteint.2012.11.009.
- [6] Scott K, Kim J-Y, Wall JJ, Park D-G, Jacobs LJ. Investigation of Fe-1.0% Cu surrogate specimens with nonlinear ultrasound. *NDT & E International* 2017;89:40–3.
- [7] Li Y, Hu S, Henager CH. Microstructure-based model of nonlinear ultrasonic response in materials with distributed defects. *Journal of Applied Physics* 2019;125:145108. doi:10.1063/1.5083957.
- [8] Kim G, In C-W, Kim J-Y, Kurtis KE, Jacobs LJ. Air-coupled detection of nonlinear Rayleigh surface waves in concrete—Application to microcracking detection. *NDT & E International* 2014;67:64–70. doi:10.1016/j.ndteint.2014.07.004.
- [9] Hurley DC, Fortunko CM. Determination of the nonlinear ultrasonic parameter using a Michelson interferometer. *Meas Sci Technol* 1997;8:634–642. doi:10.1088/0957-0233/8/6/009.
- [10] Cantrell JH. Fundamentals and applications of nonlinear ultrasonic nondestructive evaluation. *Ultrasonic nondestructive evaluation*, CRC Press; 2003, p. 377–448.
- [11] Hikata A, Sewell FA, Elbaum C. Generation of Ultrasonic Second and Third Harmonics due to Dislocations. II. *Phys Rev* 1966;151:442–9. doi:10.1103/PhysRev.151.442.

- [12] Cantrell JH, Yost WT. Nonlinear ultrasonic characterization of fatigue microstructures. *International Journal of Fatigue* 2001;23:487–90. doi:10.1016/S0142-1123(01)00162-1.
- [13] Cantrell John H. Substructural organization, dislocation plasticity and harmonic generation in cyclically stressed wavy slip metals. *Proceedings of the Royal Society of London Series A: Mathematical, Physical and Engineering Sciences* 2004;460:757–80. doi:10.1098/rspa.2003.1181.
- [14] Cantrell JH, Zhang X-G. Nonlinear acoustic response from precipitate-matrix misfit in a dislocation network. *Journal of Applied Physics* 1998;84:5469–72. doi:10.1063/1.368309.
- [15] Cantrell JH, Yost WT. Determination of precipitate nucleation and growth rates from ultrasonic harmonic generation. *Appl Phys Lett* 2000;77:1952–4. doi:10.1063/1.1311951.
- [16] Hurley DC, Balzar D, Purtscher PT. Nonlinear ultrasonic assessment of precipitation hardening in ASTM A710 steel. *Journal of Materials Research* 2000;15:2036–42. doi:10.1557/JMR.2000.0292.
- [17] Hauptert S, Renaud G, Rivière J, Talmant M, Johnson PA, Laugier P. High-accuracy acoustic detection of nonclassical component of material nonlinearity. *The Journal of the Acoustical Society of America* 2011;130:2654–61. doi:10.1121/1.3641405.
- [18] Maier S, Kim J-Y, Forstehäusler M, Wall JJ, Jacobs LJ. Noncontact nonlinear resonance ultrasound spectroscopy (NRUS) for small metallic specimens. *NDT & E International* 2018;98:37–44. doi:10.1016/j.ndteint.2018.04.003.
- [19] Barsoum MW, Radovic M, Zhen T, Finkel P, Kalidindi SR. Dynamic Elastic Hysteretic Solids and Dislocations. *Phys Rev Lett* 2005;94:085501. doi:10.1103/PhysRevLett.94.085501.
- [20] Remillieux MC, Guyer RA, Payan C, Ulrich TJ. Decoupling Nonclassical Nonlinear Behavior of Elastic Wave Types. *Phys Rev Lett* 2016;116:115501. doi:10.1103/PhysRevLett.116.115501.
- [21] TenCate JA, Pasqualini D, Habib S, Heitmann K, Higdon D, Johnson PA. Nonlinear and Nonequilibrium Dynamics in Geomaterials. *Phys Rev Lett* 2004;93:065501. doi:10.1103/PhysRevLett.93.065501.
- [22] Bentahar M, El Aqra H, El Guerjouma R, Griffa M, Scalerandi M. Hysteretic elasticity in damaged concrete: Quantitative analysis of slow and fast dynamics. *Phys Rev B* 2006;73:014116. doi:10.1103/PhysRevB.73.014116.
- [23] Payan C, Ulrich TJ, Le Bas PY, Saleh T, Guimaraes M. Quantitative linear and nonlinear resonance inspection techniques and analysis for material characterization:

- Application to concrete thermal damage. *The Journal of the Acoustical Society of America* 2014;136:537–46. doi:10.1121/1.4887451.
- [24] Muller M, Sutin A, Guyer R, Talmant M, Laugier P, Johnson PA. Nonlinear resonant ultrasound spectroscopy (NRUS) applied to damage assessment in bone. *The Journal of the Acoustical Society of America* 2005;118:3946–52. doi:10.1121/1.2126917.
- [25] Espinoza C, Feliú D, Aguilar C, Espinoza-González R, Lund F, Salinas V, et al. Linear Versus Nonlinear Acoustic Probing of Plasticity in Metals: A Quantitative Assessment. *Materials* 2018;11:2217. doi:10.3390/ma11112217.
- [26] Ostrovsky LA, Johnson PA. Dynamic nonlinear elasticity in geomaterials. *RIVISTA DEL NUOVO CIMENTO* 2001;24:46.
- [27] Maier SG. Noncontact nonlinear resonance ultrasound spectroscopy for small metallic samples. Thesis. Georgia Institute of Technology, 2017.
- [28] Abeele KE-AVD, Johnson PA, Sutin A. Nonlinear Elastic Wave Spectroscopy (NEWS) Techniques to Discern Material Damage, Part I: Nonlinear Wave Modulation Spectroscopy (NWMS). *Research in Nondestructive Evaluation* 2000;12:17–30. doi:10.1080/09349840009409646.
- [29] Doerr C, Kim J-Y, Singh P, Wall JJ, Jacobs LJ. Evaluation of sensitization in stainless steel 304 and 304L using nonlinear Rayleigh waves. *NDT & E International* 2017;88:17–23. doi:10.1016/j.ndteint.2017.02.007.
- [30] Chen J, Yin T, Kim J-Y, Xu Z, Yao Y. Characterization of thermal damage in sandstone using the second harmonic generation of standing waves. *International Journal of Rock Mechanics and Mining Sciences* 2017;91:81–9. doi:10.1016/j.ijrmms.2016.11.014.
- [31] Hikata A, Chick BB, Elbaum C. Dislocation Contribution to the Second Harmonic Generation of Ultrasonic Waves. *Journal of Applied Physics* 1965;36:229–36. doi:10.1063/1.1713881.
- [32] Breazeale MA, Thompson DO. Finite-amplitude ultrasonic waves in aluminum. *Applied Physics Letters* 1963;3:77–8.
- [33] Herrmann J, Kim J-Y, Jacobs LJ, Qu J, Littles JW, Savage MF. Assessment of material damage in a nickel-base superalloy using nonlinear Rayleigh surface waves. *Journal of Applied Physics* 2006;99:124913. doi:10.1063/1.2204807.
- [34] Zabolotskaya EA. Nonlinear propagation of plane and circular Rayleigh waves in isotropic solids. *The Journal of the Acoustical Society of America* 1992;91:2569–75. doi:10.1121/1.402993.

- [35] Van Den Abeele K. Multi-mode nonlinear resonance ultrasound spectroscopy for defect imaging: An analytical approach for the one-dimensional case. *The Journal of the Acoustical Society of America* 2007;122:73–90. doi:10.1121/1.2735807.
- [36] Capogrosso-Sansone B, Guyer RA. Dynamic model of hysteretic elastic systems. *Phys Rev B* 2002;66:224101. doi:10.1103/PhysRevB.66.224101.
- [37] Gusev V. Propagation of acoustic pulses in material with hysteretic nonlinearity. *The Journal of the Acoustical Society of America* 2000;107:3047–58. doi:10.1121/1.429333.
- [38] Guyer RA, McCall KR, Abeele KVD. Slow elastic dynamics in a resonant bar of rock. *Geophysical Research Letters* 1998;25:1585–8. doi:10.1029/98GL51231.
- [39] Johnson PA, Zinszner B, Rasolofosaon PNJ. Resonance and elastic nonlinear phenomena in rock. *Journal of Geophysical Research: Solid Earth* 1996;101:11553–64. doi:10.1029/96JB00647.
- [40] Abeele KE-AVD, Carmeliet J, Cate JAT, Johnson PA. Nonlinear Elastic Wave Spectroscopy (NEWS) Techniques to Discern Material Damage, Part II: Single-Mode Nonlinear Resonance Acoustic Spectroscopy. *Research in Nondestructive Evaluation* 2000;12:31–42. doi:10.1080/09349840009409647.
- [41] Van Den Abeele K, Schubert F, Aleshin V, Windels F, Carmeliet J. Resonant bar simulations in media with localized damage. *Ultrasonics* 2004;42:1017–24. doi:10.1016/j.ultras.2003.12.021.
- [42] Scalerandi M, Agostini V, Delsanto PP, Van Den Abeele K, Johnson PA. Local interaction simulation approach to modelling nonclassical, nonlinear elastic behavior in solids. *The Journal of the Acoustical Society of America* 2003;113:3049–59. doi:10.1121/1.1570440.
- [43] Granato A, Lücker K. Theory of Mechanical Damping Due to Dislocations. *Journal of Applied Physics* 1956;27:583–93. doi:10.1063/1.1722436.
- [44] Kinsler LE, Frey AR, Coppens AB, Sanders JV. *FUNDAMENTALS OF ACOUSTICS*, 4TH ED. Wiley India Pvt. Limited; 2009.
- [45] Rutherford A. *Introducing Anova and Ancova: A GLM Approach*. London, UNITED KINGDOM: SAGE Publications; 2000.
- [46] Ford FP, Gordon BM, Horn RM. 16 - Intergranular stress corrosion cracking (IGSCC) in boiling water reactors (BWRs). In: Féron D, editor. *Nuclear Corrosion Science and Engineering*, Woodhead Publishing; 2012, p. 548–80. doi:10.1533/9780857095343.5.548.
- [47] Trillo EA, Beltran R, Maldonado JG, Romero RJ, Murr LE, Fisher WW, et al. Combined effects of deformation (strain and strain state), grain size, and carbon

- content on carbide precipitation and corrosion sensitization in 304 stainless steel. *Materials Characterization* 1995;35:99–112. doi:10.1016/1044-5803(95)00072-0.
- [48] Chung P, Szklarska-Smialowska S. The Effect of Heat Treatment on the Degree of Sensitization of Type 304 Stainless Steel. *CORROSION* 1981;37:39–50. doi:10.5006/1.3593836.
- [49] Pascali R, Benvenuti A, Wenger D. Carbon Content and Grain Size Effects on the Sensitization of AISI Type 304 Stainless Steels. *CORROSION* 1984;40:21–32. doi:10.5006/1.3579291.
- [50] Kokawa H, Shimada M, Sato YS. Grain-boundary structure and precipitation in sensitized austenitic stainless steel. *JOM* 2000;52:34–7. doi:10.1007/s11837-000-0159-0.
- [51] Trillo EA, Murr LE. Effects of carbon content, deformation, and interfacial energetics on carbide precipitation and corrosion sensitization in 304 stainless steel. *Acta Materialia* 1998;47:235–45. doi:10.1016/S1359-6454(98)00322-X.
- [52] Garcia C, Martin F, De Tiedra P, Heredero JA, Aparicio ML. Effect of Prior Cold Work on Intergranular and Transgranular Corrosion in Type 304 Stainless Steels: Quantitative Discrimination by Image Analysis. *CORROSION* 2000;56:243–55. doi:10.5006/1.3287650.
- [53] G01 Committee. Test Method for Electrochemical Reactivation (EPR) for Detecting Sensitization of AISI Type 304 and 304L Stainless Steels. *ASTM International*; n.d. doi:10.1520/G0108-94R15.
- [54] Doerr C. Evaluation of sensitization in stainless steel 304 and 304L using nonlinear Rayleigh waves. Thesis. Georgia Institute of Technology, 2016.
- [55] Smith TR, Sugar JD, Schoenung JM, San Marchi C. Anomalous Annealing Response of Directed Energy Deposited Type 304L Austenitic Stainless Steel. *JOM* 2018;70:358–63. doi:10.1007/s11837-017-2711-1.
- [56] Blazkiewicz M. The development of nondestructive evaluation (NDE) for monitoring the embrittlement in nuclear reactor pressure vessels. *Materials Science Forum*, vol. 210, Trans Tech Publ; 1996, p. 9–16.
- [57] Odette GR, Lucas GE. Embrittlement of nuclear reactor pressure vessels. *JOM* 2001;53:18–22. doi:10.1007/s11837-001-0081-0.
- [58] Pavinich W, Griesbach T, Server W. An Overview of Radiation Embrittlement Modeling for Reactor Vessel Steels. *An Overview of Radiation Embrittlement Modeling for Reactor Vessel Steels*, 1993.

- [59] Akamatsu M, Van Duysen JC, Pareige P, Auger P. Experimental evidence of several contributions to the radiation damage in ferritic alloys. *Journal of Nuclear Materials* 1995;225:192–5. doi:10.1016/0022-3115(95)00028-3.
- [60] Carter RG, Soneda N, Dohi K, Hyde JM, English CA, Server WL. Microstructural characterization of irradiation-induced Cu-enriched clusters in reactor pressure vessel steels. *Journal of Nuclear Materials* 2001;298:211–24. doi:10.1016/S0022-3115(01)00659-6.
- [61] Gurovich BA, Kuleshova EA, Nikolaev YuA, Shtrombakh YaI. Assessment of relative contributions from different mechanisms to radiation embrittlement of reactor pressure vessel steels. *Journal of Nuclear Materials* 1997;246:91–120. doi:10.1016/S0022-3115(97)00103-7.
- [62] Phythian WJ, English CA. Microstructural evolution in reactor pressure vessel steels. *Journal of Nuclear Materials* 1993;205:162–77. doi:10.1016/0022-3115(93)90079-E.
- [63] Odette GR. On the dominant mechanism of irradiation embrittlement of reactor pressure vessel steels. *Scripta Metallurgica* 1983;17:1183–8. doi:10.1016/0036-9748(83)90280-6.
- [64] Odette G, Lucas G. Irradiation Embrittlement of Reactor Pressure Vessel Steels: Mechanisms, Models, and Data Correlations. *Irradiation Embrittlement of Reactor Pressure Vessel Steels: Mechanisms, Models, and Data Correlations*, 1986.
- [65] Barbu A, Le TN, Lorenzelli N, Maury F, de Novion CH. Formation of copper-rich precipitates by electron irradiation or by thermal treatment in model iron-based alloys. *Annales de Chimie Science Des Materiaux (Paris)* 1991;16:325–31.
- [66] Blackstock JJ, Ackland GJ. Phase transitions of copper precipitates in Fe–Cu alloys. *Philosophical Magazine A* 2001;81:2127–48. doi:10.1080/01418610108217139.
- [67] Charleux M, Livet F, Bley F, Louchet F, Bréchet Y. Thermal ageing of an Fe [sbnd] Cu alloy: Microstructural evolution and precipitation hardening. *Philosophical Magazine A* 1996;73:883–97.
- [68] Hu SY, Li YL, Watanabe K. Calculation of internal stresses around Cu precipitates in the bcc Fe matrix by atomic simulation. *Modelling Simul Mater Sci Eng* 1999;7:641–655. doi:10.1088/0965-0393/7/4/312.
- [69] Othen PJ, Jenkins ML, Smith GDW. High-resolution electron microscopy studies of the structure of Cu precipitates in α -Fe. *Philosophical Magazine A* 1994;70:1–24.
- [70] Vandenbossche LP, Konstantinović MJ, Almazouzi A, Dupré LR. Magnetic evaluation of the hardening and softening of thermally aged iron–copper alloys. *Journal of Physics D: Applied Physics* 2007;40:4114.

- [71] Zhu J, Zhang T, Yang Y, Liu CT. Phase field study of the copper precipitation in Fe-Cu alloy. *Acta Materialia* 2019;166:560–71. doi:10.1016/j.actamat.2019.01.009.
- [72] Smallman RE, Ngan AHW. Chapter 10 - Surfaces, Grain Boundaries and Interfaces. In: Smallman RE, Ngan AHW, editors. *Modern Physical Metallurgy (Eighth Edition)*, Oxford: Butterworth-Heinemann; 2014, p. 415–42. doi:10.1016/B978-0-08-098204-5.00010-9.
- [73] Han Y-S, Park D-G, Kobayashi S. Small angle neutron scattering study of nano sized precipitates in ferrous alloys. *Journal of Nanoscience and Nanotechnology* 2015;15:8608–12.
- [74] Thiele S, Kim J-Y, Qu J, Jacobs LJ. Air-coupled detection of nonlinear Rayleigh surface waves to assess material nonlinearity. *Ultrasonics* 2014;54:1470–5. doi:10.1016/j.ultras.2014.04.020.
- [75] Thiele S. Air-coupled detection of Rayleigh surface waves to assess material nonlinearity due to precipitation in alloy steel. Thesis. Georgia Institute of Technology, 2013.
- [76] Kim Y-H. *Sound Propagation: An Impedance Based Approach*. John Wiley & Sons; 2010.
- [77] Bender FA, Kim J-Y, Jacobs LJ, Qu J. The generation of second harmonic waves in an isotropic solid with quadratic nonlinearity under the presence of a stress-free boundary. *Wave Motion* 2013;50:146–61. doi:10.1016/j.wavemoti.2012.08.009.
- [78] Matlack KH, Kim J-Y, Jacobs LJ, Qu J. Review of Second Harmonic Generation Measurement Techniques for Material State Determination in Metals. *J Nondestruct Eval* 2014;34:273. doi:10.1007/s10921-014-0273-5.
- [79] Trivett DH, Robinson AZ. Modified Prony method approach to echo-reduction measurements. *The Journal of the Acoustical Society of America* 1981;70:1166–75. doi:10.1121/1.386948.
- [80] Marple L, Brotherton T. Detection and classification of short duration underwater acoustic signals by Prony's method. [Proceedings] ICASSP 91: 1991 International Conference on Acoustics, Speech, and Signal Processing, 1991, p. 1309–12 vol.2. doi:10.1109/ICASSP.1991.150648.
- [81] Kley M, Valle C, Jacobs LJ, Qu J, Jarzynski J. Development of dispersion curves for two-layered cylinders using laser ultrasonics. *The Journal of the Acoustical Society of America* 1999;106:582–8. doi:10.1121/1.427135.
- [82] Ravanbod H, Karimi F, Amindavar H. Flaw characterization in ultrasonic non-destructive testing method using exponential modeling. 2013 IEEE International Instrumentation and Measurement Technology Conference (I2MTC), 2013, p. 1676–9. doi:10.1109/I2MTC.2013.6555699.

- [83] Saniie J, Jin XM. Spectral analysis for ultrasonic nondestructive evaluation applications using autoregressive, Prony, and multiple signal classification methods. *The Journal of the Acoustical Society of America* 1996;100:3165–71. doi:10.1121/1.417126.
- [84] Marple SL. *Digital spectral analysis: with applications*. vol. 5. Prentice-Hall Englewood Cliffs, NJ; 1987.
- [85] Vaseghi SV. *Advanced digital signal processing and noise reduction*. John Wiley & Sons; 2008.
- [86] Scott K, Kim J-Y, Jacobs LJ. Signal processing methods for second harmonic generation in thin specimens. *NDT & E International* 2018;95:57–64. doi:10.1016/j.ndteint.2018.02.001.
- [87] Blaricum MLV, Mittra R. Problems and Solutions Associated with Prony's Method for Processing Transient Data. *IEEE Transactions on Electromagnetic Compatibility* 1978;EMC-20:174–82. doi:10.1109/TEMC.1978.303708.
- [88] Fisher K. *Structural and Acoustic Response of Motion Sensors Mounted on a Compliant Coating*. Dissertation. Georgia Institute of Technology, 1998.
- [89] Glandier CY, Berthelot YH, Jarzynski J. Wave-vector analysis of the forced vibrations of cylindrical shells of finite length. *The Journal of the Acoustical Society of America* 1992;92:1985–93. doi:10.1121/1.405248.
- [90] Braun S, Ram YM. Determination of structural modes via the Prony model: System order and noise induced poles. *The Journal of the Acoustical Society of America* 1987;81:1447–59. doi:10.1121/1.394497.
- [91] Kumaresan R, Tufts DW, Scharf LL. A Prony method for noisy data: Choosing the signal components and selecting the order in exponential signal models. *Proceedings of the IEEE* 1984;72:230–3. doi:10.1109/PROC.1984.12849.
- [92] Scott K. *Characterization of nuclear reactor pressure vessel (RPV) surrogate specimens with ultrasound*. Thesis. Georgia Institute of Technology, 2016.
- [93] Russell KC, Brown LM. A dispersion strengthening model based on differing elastic moduli applied to the iron-copper system. *Acta Metallurgica* 1972;20:969–74.
- [94] Schmauder S, Binkele P. Atomistic computer simulation of the formation of Cu-precipitates in steels. *Computational Materials Science* 2002;24:42–53.
- [95] YANG J, ENOMOTO M. Numerical simulation of copper precipitation during aging in deformed Fe-Cu alloys. *ISIJ International* 2005;45:1335–44.

- [96] Zhang C, Enomoto M, Yamashita T, Sano N. Cu precipitation in a prestrained Fe-1.5 wt pct Cu alloy during isothermal aging. *Metallurgical and Materials Transactions A* 2004;35:1263–72.
- [97] Zhao JZ, Wang QL, Li HL, He J. Modeling of the Precipitation Kinetics During Aging a Predeformed Fe-Cu Alloy. *Metallurgical and Materials Transactions A* 2011;42:3200–7.
- [98] Ackland GJ, Bacon DJ, Calder AF, Harry T. Computer simulation of point defect properties in dilute Fe—Cu alloy using a many-body interatomic potential. *Philosophical Magazine A* 1997;75:713–32.
- [99] Maury F, Lorenzelli N, Mathon MH, De Novion CH, Lagarde P. Copper precipitation in FeCu, FeCuMn, and FeCuNi dilute alloys followed by X-ray absorption spectroscopy. *Journal of Physics: Condensed Matter* 1994;6:569.
- [100] Soisson F, Barbu A, Martin G. Monte Carlo simulations of copper precipitation in dilute iron-copper alloys during thermal ageing and under electron irradiation. *Acta Materialia* 1996;44:3789–800.
- [101] Kube CM, Turner JA. Acoustic nonlinearity parameters for transversely isotropic polycrystalline materials. *The Journal of the Acoustical Society of America* 2015;137:3272–80.
- [102] Fahse DN. Investigation of microstructural changes in CR9M01 due to thermal aging using SHG and NRUS methods. Georgia Institute of Technology, 2019.
- [103] Mirzadeh H, Najafizadeh A. Aging kinetics of 17-4 PH stainless steel. *Materials Chemistry and Physics* 2009;116:119–24. doi:10.1016/j.matchemphys.2009.02.049.
- [104] Park J, Kim M, Chi B, Jang C. Correlation of metallurgical analysis & higher harmonic ultrasound response for long term isothermally aged and crept FM steel for USC TPP turbine rotors. *NDT & E International* 2013;54:159–65. doi:10.1016/j.ndteint.2012.10.008.
- [105] Cipolla L, Di Gianfrancesco A, Venditti D, Cumino G, Caminada S. Microstructural Evolution During Long Term Creep Tests of 9%Cr Steel Grades, American Society of Mechanical Engineers Digital Collection; 2009, p. 445–59. doi:10.1115/CREEP2007-26030.
- [106] Hald J. Microstructure and long-term creep properties of 9–12% Cr steels. *International Journal of Pressure Vessels and Piping* 2008;85:30–7. doi:10.1016/j.ijpvp.2007.06.010.
- [107] Sawada K, Miyahara K, Kushima H, Kimura K, Matsuoka S. Contribution of Microstructural Factors to Hardness Change during Creep Exposure in Mod.9Cr-1Mo Steel. *ISIJ International* 2005;45:1934–9. doi:10.2355/isijinternational.45.1934.

- [108] Influence of Z-phase on long-term creep stability of martensitic 9-12% Cr steels (Conference) | ETDEWEB n.d. <https://www.osti.gov/etdeweb/biblio/21588182> (accessed October 4, 2019).
- [109] Setyawan W, Henager CH, Hu S. Nonlinear ultrasonic response of voids and Cu precipitates in body-centered cubic Fe. *Journal of Applied Physics* 2018;124:035104. doi:10.1063/1.5029368.